COMPUTATIONAL INVESTIGATION OF LYMPHATIC VALVES AND VESSELS

A Dissertation
Presented to
The Academic Faculty

by

Ki Tae Wolf

In Partial Fulfillment
of the Requirements for the Degree
Doctor of Philosophy in the
George W. Woodruff School of Mechanical Engineering

Georgia Institute of Technology
August 2021

COMPUTATIONAL INVSTIGATION OF LYMPHATIC VALVES AND VESSELS

Approved by:

Dr. Alexander Alexeev, Advisor
School of Mechanical Engineering
Georgia Institute of Technology

Dr. David Hu
School of Mechanical Engineering
Georgia Institute of Technology

Dr. J. Brandon Dixon
School of Mechanical Engineering
Georgia Institute of Technology

Dr. Damir Khismatullin
School of Science and Engineering
Tulane University

Dr. Rudolph Gleason
School of Mechanical Engineering
Georgia Institute of Technology

Date Approved: May 3, 2021

ACKNOWLEDGEMENTS

First, I would like to express my deepest gratitude to my family. Their encouragement for me to pursue my passion led me to pursue a PhD program in mechanical engineering. And without their moral support through difficult times, this thesis would not be possible. I would also like to thank my advisor Dr. Alexeev for welcoming me into his lab and for his willingness to take a chance on me. Joining his group with a background in physics, Dr. Alexeev's guidance and patience in my work led me to progress through not just the PhD program, but through a transition from physics to mechanical engineering. His encouragement towards attending conferences and exploring new topics led me to have a much broader PhD experience and helped me to gain new skills like public speaking, something I almost feared before. Not just an advisor, Dr. Alexeev has been a true mentor and a guide through my nearly five years during the PhD program.

I would also like to thank Dr. Dixon from our collaborating research group. Knowing little about the lymphatic system when first joining the PhD program, his patience, guidance, and insight led me to appreciate the lymphatic system. His introduction into the lymphatics research community also led me to appreciate the hard work that the lymphatic community does in advancing our understanding of the lymphatic system, even though I believe the attention that the lymphatic research community gets is still far smaller than its importance.

Last but not least, I like to thank the remaining members of my committee, Dr. Gleason, Dr. Hu, and Dr. Khismatullin. Their insights, guidance, and time spent for my dissertation have been crucial for my successful completion of the PhD program.

TABLE OF CONTENTS

LIST OF TABLES

LIST OF FIGURES

SUMMARY

The lymphatic system transports macromolecules and fluids throughout the body via contractions of lymphatic vessels. This flow from vessel contractions is regulated by unidirectional lymphatic valves, which allow lymphatic pumping against adverse pressure gradient. Despite the importance of the lymphatic system, understanding of lymphatic operation, especially the role of lymphatic valves, is still limited. By using a fully coupled three-dimensional fluid-structure interaction model created using lattice Boltzmann method and lattice spring model, we computationally investigate the role of lymphatic valve and vessel properties on lymphatic pumping. First, the effect of lymphatic valve properties such as valve aspect ratio and bending stiffness on pumping performance is investigated with a rigid lymphatic vessel. This study found that shorter and more flexible valves generally reduce flow resistance but valves that are too short cannot block backflow properly. Then, the effect of lymphatic valve and vessel properties on pumping performance under vessel contraction is studied. This study showed that lymphatic valve and vessel properties have complex relationship with lymphatic pumping, and all parameters investigated have optimal conditions with maximum pumping efficiencies. Finally, a model of lymphatic filarial worm is created and introduced to the model of lymphatic valve and vessel to investigate the worm's behavior when navigating through the

lymphatic system. Overall, this work highlights many important parameters of lymphatic valve and vessel that affect lymphatic operation and provides insights into conditions that may cause lymphatic disorders.

CHAPTER 1. INTRODUCTION

1.1 Motivation

The lymphatic system plays a critical role in maintaining homeostasis of the body by transporting interstitial fluid, fatty acid, and immune cells. These macromolecules and fluids are collected from initial lymphatics to eventually join the circulatory system and maintain fluid balance and waste disposal in tissues. Fatty acid absorbed from digestive tracts is also transported via the lymphatic system, while immune cells and antigens transported via the collecting lymphatics play an extremely valuable role in providing proper immune responses [1, 2]. Despite many functions of the lymphatic system, the entire system operates without any centralized pump under adverse pressure gradients produced by factors such as gravity. Rather, the lymphatic pumping is achieved by a combination of extrinsic pumping, defined as skeletal muscular movement of nearby tissues [3-7] and intrinsic pumping from a series of contracting lymphatic vessels and valves dispersed throughout the entire collecting lymphatic [8-10]. Specifically, intrinsic lymphatic pump is made of chains of lymphangions, which is a section of lymphatic vessel surrounded by two lymphatic valves. Within these lymphangions, lymphatic valves reduce backflow and promote unidirectional flow under a considerable adverse pressure gradient. Figure 1.1 shows a schematic of a lymphatic vessel composed of lymphangions and valves. Consequentially, dysfunctions of these valves can result in serious medical disorders like lymphedema, where excess interstitial fluid is pooled in parts of the body like the extremities [11].

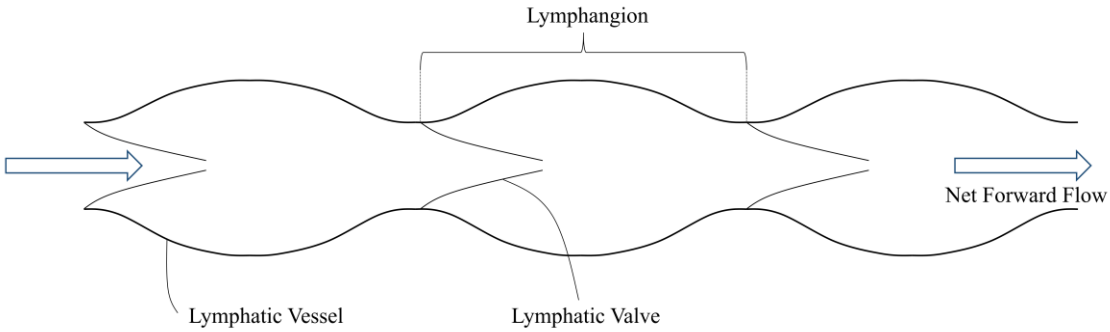

Figure 1.1 A diagram of a chain of lymphangions in a lymphatic vessel. Each lymphangion is a section of lymphatic vessel that contains a bi-leaflet lymphatic valve. Lymphatic vessels produce a net lymph flow (here shown left to right) through periodic contractions combined with unidirectional lymphatic valves that open and close due to fluctuating pressure throughout the contraction cycle.

Currently, ways to treat conditions like lymphedema are limited. Methods such as compression garments only address the symptoms without addressing the underlying causes. Although a general identification of causes of lymphedema is made between hereditary (known as primary lymphedema) and acquired (known as secondary lymphedema), the method and extent that various causes lead to manifestation of symptoms are largely unknown [12]. For example, genetic valve defects in primary lymphedema have been identified as a major source of the disorder [13-18], but the mechanism and importance of valve dysfunction to the actual disorder are still unknown. Different features of the valves like their heterogeneity in length are even less studied, leaving the effect of different lymphatic valve features to valve dysfunction and overall lymphatic pumping unknown.

Lymphatic pumping also presents a unique flow environment. Due to its typical geometric scales like its vessel diameters [19-21], the Reynolds number of lymphatic system falls solidly within a laminar regime with typical values around $Re = 1$ and is

reported to not exceed over $Re = 16$ [22, 23]. However, lymphatic flow is created through a combination of external contraction and internal contraction of lymphatic muscles. This contractile nature of flow creation leads to a flow environment where flow pulsation, vessel contraction-based flow, and lymphatic valves' flow disruption all affect lymphatic pumping. Although the pulsatile nature of lymphatic pumping is known to be quasi-static due to its Womersley number less than 1 [22], combination of peristaltic pumping from vessel contraction and flexible one-way lymphatic valve still brings in additional complexity to lymphatic pumping. Consequentially, effect of parameters that govern flow pulsation, peristaltic pumping, and valve mechanics such as Womersley number, lymphatic vessel contraction amplitude, and valve bending stiffness all play important roles in lymphatic pumping.

To address this limitation in understanding the lymphatic system, computational studies have been providing valuable insights into the workings of the lymphatic system. Lumped parameter models have captured lymphatic behavior in chains of lymphangions and expanded our understanding of the lymphatic system, but the model could not capture detailed response of lymphatic components like lymphatic valves under varied factors such as the valve length or valve mechanical properties [24-32]. Multi-dimensional models have been providing valuable information on lymphatic components' roles and effect on the overall pumping behavior, but these models did not simultaneously couple the fluid and the solid components of the collecting lymphatics [19, 21, 33, 34], unable to capture how different lymphatic components work dynamically. Thus, our work aims to create a fully coupled fluid-structure interaction model of the collecting lymphatic in a three-dimensional environment that more accurately captures dynamic response of lymphatic components,

enhancing our current understanding of the lymphatic system in addition to the aforementioned findings.

1.2 Survey of Prior Studies

1.2.1 Lumped parameter studies (zeroth-order models)

Lumped parameter model is a time-dependent model that describes the lymphatic system using ordinary differential equations. The model is spatially independent and incorporates multiple empirical fits based on experimental studies of lymphatic components. The biggest advantage of the lumped parameter model is its relatively low computational cost. Because lumped parameter model treats a relevant subdivision such as a section of lymphatic vessel across a single lymphangion or a lymphatic valve as one lumped node, relevant metrics like the average pressure across a lymphangion or average diameter of the vessel segment can be calculated with very low cost compared to multi-dimensional models. This is especially useful for structures like the lymphatic system where there are series or networks of alternatingly repeating lymphatic components of lymphatic vessels and valves.

However, these advantages of the lumped parameter model also present the model's limitation. Because each component is represented as a single node, the lumped parameter model does not account for variation of detailed features of individual node unless described by an empirical model. A good example of this limitation is the variation of geometric or mechanical properties of the lymphatic valve. Furthermore, because the model relies greatly on empirical fits, inaccuracies or limitation of experimental data directly relates to the accuracies of the model. Again, a good example is the flow resistance

model of the lymphatic valve [26, 30, 31] since the sigmoidal flow resistance model of the lymphatic valve does not account for variation of valve properties with arbitrary parameter selections.

Even so, lumped parameter models yielded many crucial findings about the lymphatic system. Considering the limited representation of lymphatic valves through lumped parameter models, many studies focus primarily on lymphatic vessel contraction parameters. For example, work by Baish, *et al* [24] showed how calcium ion transport and nitric oxide production create two oscillators that complement each other in lymphatic muscle contraction and eventual lymphatic vessel contraction. Work by Jamalian, *et al* [30] explored lymphatic chains when connected via branched networks and found optimal pumping conditions such as lymphangion lengths under different adverse pressure gradients. Finally, work by Razavi, *et al* [31] presented a combination of lumped parameter modeling and in vivo measurements to approximate lymphatic muscle contraction. The work gathered pumping pressure profile through in vivo measurements and incorporated it into lumped parameter model to understand mechanism behind measured pressure profile and determined relevant parameters affecting the observed in vivo data.

Despite the limited representation of the lymphatic valve, lumped parameter model also revealed many important features of lymphatic valves. This was explored in works by Bertram, *et al* [26-28] and Jamalian, *et al*[29], where features such as valves' bias to stay open and valves' hysteresis under changing flow condition were represented and incorporated into the lumped parameter model. The studies revealed valves can significantly affect flow under different vessel contraction conditions.

1.2.2 Multi-dimensional models

Because of the above-mentioned limitations that lumped parameter model possesses, there have been many multi-dimensional studies of the lymphatic system. These models typically reduced its domain size while incorporating a more detailed representation of the lymphatic system. The models range from one-dimensional to three dimensional models, while many models implement simultaneously coupled fluid-structure interaction except in a three-dimensional domain.

For one-dimensional model, MacDonald [19] created a model that closely resembles the lumped parameter model. Although the vessel section inside a lymphangion was divided into several computational cells along its length, lymphatic valves were still represented as a single computational cell. This model represents an intermediary between lumped parameter and multi-dimensional model where computational cost is reduced while having a greater resolution of the lymphangion behavior, especially of the vessel wall. By incorporating measured mechanical properties of various lymphangion components into the model, this model reproduced lymphatic pumping behavior with greater details. Furthermore, results from the model suggested that flow inside the experimentally measured bovine lymphatic can be computationally reproduced with a simple and fast traveling contraction pulses.

Two and three-dimensional models further reduced its scope while focusing more on additional details of the lymphatic system. For example, two-dimensional model by Kunert [33] incorporates not only fluid-structure interaction model, but also a chemical response of the lymphatic vessel based on production and concentration of Ca^{2+} and NO.

This work found a feedback loop between concentrations of Ca^{2+} and NO which creates a stable chemical mechanism of lymphatic vessel contraction under different flow environments. Although this model incorporates higher geometric resolution, simultaneous fluid-structure interaction, and reaction-diffusion-advection models for the two chemical species, the two-dimensional nature of the model could not capture the full geometric profile of the valves.

Three-dimensional models can address this geometric limitation by more accurately modeling the lymphatic valves and vessels. Wilson [21] utilized a very detailed model of the lymphatic valve and vessel via geometric acquisition through confocal imaging, which allowed an inclusion of features such as vessel expansion around the lymphatic valve (sinus) and crescent-shaped depression of the bicuspid valve leaflets. This study revealed a reduction in viscous loss by the sinus, reducing net pumping loss when compared to a straight tube representation of lymphatic vessel. However, this model assumed solid response based on steady flow assumption, which created a degree of decoupling between fluid and solid solvers. Other models like the work by Rahbar [34] ran a computational fluid dynamics model instead of fluid-structure interaction, where unsteady flow was simulated inside a valve-less section of a lymphatic vessel with prescribed wall motion. Even so, this work validated the quasi-static assumption of lymphatic flow observed [22] despite a range of different wall expansions and contractions the lymphatic vessels generate.

1.2.3 Lymphatic filariasis

Of many causes of lymphatic dysfunction, lymphatic filariasis is caused by parasitic filarial worms that specifically reside within human lymphatic system during a part of their larval stages and adult life [35]. The rest of worms' lifecycle takes place inside mosquitoes, where they act as hosts for worms' early larval stages and vectors for human transmission through mosquito bites [36]. The worms' residence within the lymphatic system until their deaths cause adult filarial worms and their dead bodies to become a source of obstruction for proper lymphatic pumping. Extensive and untreated damages done by the adult and dead worms can thus cause an onset of lymphedema and sometimes even more serious conditions such as hydrocele or limb elephantiasis [35].

Lymphatic filariasis is a serious health concern worldwide, especially in tropical regions [36, 37], but is considered a neglected tropical disease [37]. Even worse, studies on mechanism and process of initial lymphatic infection during its transmission from mosquito bites and consequential navigation to and around the lymphatic system are very limited [35, 38-42]. Due to this limited understanding of filarial worms' infection and navigation in their infective larval stages, filarial worm model for this work will be based on locomotion model of its well-studied nematode cousin *C. elegans* [43-46] with some available physiological and in-vitro behavioral data used for more accurate modeling and validation [39, 47, 48].

1.3 Thesis objectives

This work aims to investigate three aspects of the collecting lymphatics that could not be easily studied with existing experimental methods. First, a computational model for lymphatic valve will be developed, and valve mechanics will be studied. Experimental studies have suggested that lymphatic valves can display complex time-dependent response and exist under varied geometry and mechanical properties, but experimental data of valve properties have been little to nonexistent, while existing computational models could not fully replicate many valve behaviors such as time-dependent valve response [8, 49]. For this objective, we will simplify the actively contracting lymphatic vessel with a unidirectional valve by considering a rigid vessel with applied pressure gradient to simulate flow in order to focus our analysis to only lymphatic valve's effect on lymph flow. Valve effect to lymph flow under varied valve properties will be investigated along with valve's response under time-dependent flow condition. Then, lymphatic valve's performance under different valve properties will be optimized to show an existence of optimal valve parameters while experimental works will be compared with numerical results to gauge the confidence of the computational model. This understanding of lymphatic valve mechanics can be incorporated into existing models like the lumped parameter method where a table of simulated results can be created to represent the effect of lymphatic valve more accurately.

Because the first objective necessarily assumes a rigid lymphatic vessel wall, the next objective will develop a lymphatic model with contracting vessel and study the effect of lymphatic valve and contracting vessel. With a greater understanding of valve mechanics from the first objective, lymphatic valve's role in lymphatic pumping will be more clearly

distinguished. By assuming a simplified, sinusoidal vessel motion, the role of lymphatic valve can be more clearly analyzed through a comparison with its valve-less counterpart [50, 51]. Along with valve parameters, lymphatic vessel parameters will also be varied for this objective. The lymphatic pumping performance will be analyzed through flow efficiency and time-averaged flow rates under varied valve and vessel parameters. The objective will gauge the range that lymphatic valves are needed for better pumping while possibly expending additional energy, which will be represented via the pumping efficiency. Furthermore, this analysis will be compared with experimentally reported operating range of the collecting lymphatics, providing a greater insight into the reason behind certain lymphatic geometry and properties. Finally, because this objective will compare the pumping performance of the lymphatic vessel without a valve, we can see the extent of adverse pressure gradient and flow capacity that lymphatic system with valve dysfunction can handle, providing a greater understanding to the extent that valve dysfunction can contribute to the manifestation of lymphatic disorders like lymphedema.

The final objective will develop a model for a filarial worm, integrate the model to the existing lymphatic model, and examine the effects of a filarial worm on the lymphatic system. After a physiologically relevant filarial thrashing model is developed, different test cases will compare the worm's thrashing to experimental studies that analyzed the worm's behavior in-vitro and in microfluidic channels, thus validating the worm's simulated motion [39, 52]. Then, the filarial worm will be integrated into the lymphatic model with a rigid lymphatic wall with applied pressure gradient. Filarial worm parameters will be varied to observe the worm's behavior and speed in navigating past the valve. This

objective can provide a valuable insight into how filarial worm navigates the lymphatic system since in-vivo and computational study with filarial worm are very limited.

CHAPTER 2. METHODOLOGY

To address the limitations presented by the existing models, we utilized a fully coupled time-dependent model in a three-dimensional environment. To achieve this, lattice Boltzmann method (LBM) and lattice spring model (LSM) were used for fluid and solid components, respectively. Then, the fluid and solid components are coupled via an exchange of momentum from solid component to the fluid nodes using an interpolated bounce-back, while corresponding forces are applied to nearby solid nodes to conserve the momentum during the fluid-solid interaction [53, 54].

2.1 Lattice Boltzmann model

Lattice Boltzmann method (LBM) is a widely used, efficient solver for incompressible viscous flows [55, 56]. LBM is especially effective in simulating flows with complex geometries and can be easily integrated to parallel high-performance computing, making an essential fluid solver for fluid-structure interaction problems [57-60]. LBM represents Navier-Stokes equation at mesoscale level by solving discrete Boltzmann equation.

LBM solves a velocity distribution function of fluid "particles" $f_i(\boldsymbol{r}, t)$ in a fixed spatial lattice, where i is the velocity direction, $\boldsymbol{r}$ is the lattice node and t is time. For each time step, these fluid "particles" can move from one node to another at a discrete velocity $\boldsymbol{c}_i$. The velocity direction i and discrete velocity $\boldsymbol{c}_i$ depend on the dimension and lattice structure of the simulated model. For this work, we use D3Q19 method, which indicates

that the lattice structure is three-dimensional with 19 unique directions that fluid "particles" can move. The schematic of D3Q19 lattice with each $\boldsymbol{c}_i$ is shown in Figure 2.1.

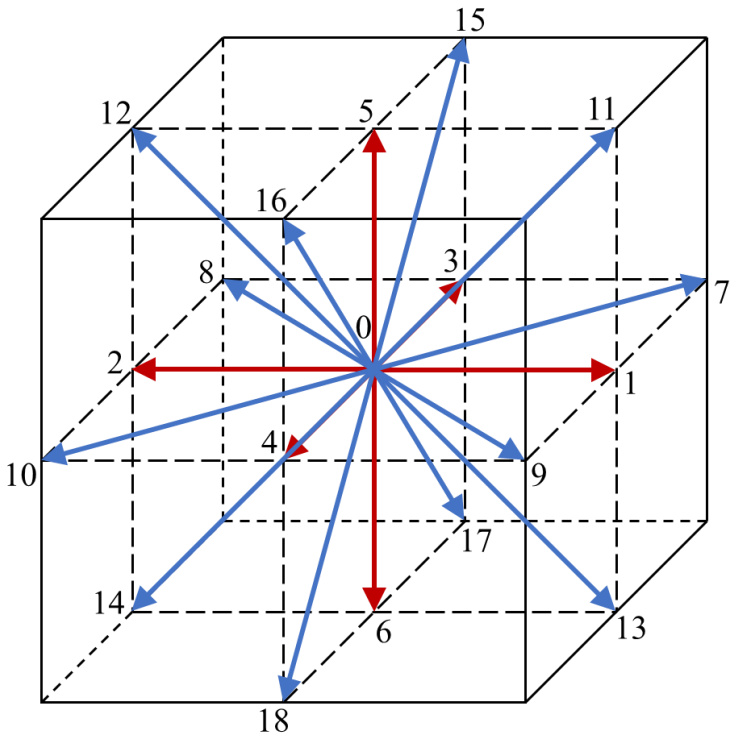

Figure 2.1 Schematic of LBM lattice in D3Q19 model. Arrows represent different discrete velocities $\boldsymbol{c}_i$.

Based on the labeling of velocity directions in Figure 2.1, each discrete velocity vector in D3Q19 can be written as:

$$\boldsymbol{c}_i = \begin{cases} (0,0,0), & i = 0 \\ (\pm 1,0,0), (0,\pm 1,0), (0,0,\pm 1), & i = 1,2,\ldots,5,6 \\ (\pm 1,\pm 1,0), (\pm 1,0,\pm 1), (0,\pm 1,\pm 1), & i = 7,8,\ldots,17,18 \end{cases} \quad (1)$$

LBM calculates hydrodynamics quantities like fluid density ρ, fluid momentum density $\boldsymbol{j}$, and momentum flux $\boldsymbol{\Pi}$ as moments of velocity distribution functions as follows:

$$\rho = \sum_i f_i \tag{2}$$

$$\boldsymbol{j} = \rho \boldsymbol{u} = \sum_i f_i \boldsymbol{c}_i \tag{3}$$

$$\boldsymbol{\Pi} = \rho \boldsymbol{I} + \rho \boldsymbol{u}\boldsymbol{u} = \sum_i f_i \boldsymbol{c}_i \boldsymbol{c}_i \tag{4}$$

Note that $\boldsymbol{u}$ represents macroscale velocity of fluid "particles". The distribution function is integrated over time through discrete time steps via streaming and collisions steps, governed by the discretized Boltzmann equation [56]. The streaming equation is given as

$$f_i(\boldsymbol{r} + \boldsymbol{c}_i \Delta t, t + \Delta t) = f_i(\boldsymbol{r}, t) + \Omega_i(\boldsymbol{r}, t) \tag{5}$$

Note that Δt is the LBM time step, and $\Omega_i(\boldsymbol{r}, t)$ is the collision operator. The summation of old fluid "particles" with a collision operator indicates the collision step of LBM where old fluid "particles" change due to collision at a given node.

This work uses a collision operator with two relaxation times based on work by Ladd and Verberg [55]. When compared against a collision operator with a single relaxation time, this collision operator brings greater numerical stability and flexibility of LBM operation at a larger range of Reynolds numbers. The post-collision distribution function can be written as

$$f_i(\boldsymbol{r}, t) + \Omega_i(\boldsymbol{r}, t) = a^{c_i}\left[\rho + \frac{\boldsymbol{j} \cdot \boldsymbol{c}_i}{c_s^2} + \frac{\left(\rho \boldsymbol{u}\boldsymbol{u} + \boldsymbol{\Pi}_{neq}^*\right) : \left(\boldsymbol{c}_i \boldsymbol{c}_i - c_s^2 \mathbf{I}\right)}{2c_s^4}\right] \tag{6}$$

Note that $c_s = \Delta x/\sqrt{3}\Delta t$ is the speed of sound where Δx is the lattice spacing between neighboring lattice nodes. The coefficient $a^{\boldsymbol{c}_i}$ is a weight term for a given velocity direction $\boldsymbol{c}_i$ and is defined as

$$a^{\boldsymbol{c}_i} = \begin{cases} 1/3, & |\boldsymbol{c}_i| = 0 \\ 1/18, & |\boldsymbol{c}_i| = 1 \\ 1/36, & |\boldsymbol{c}_i| = \sqrt{2} \end{cases} \tag{7}$$

The tensor $\boldsymbol{\Pi}^*_{neq}$ is the nonequilibrium momentum flux. In particular, $\boldsymbol{\Pi}^*_{neq}$ can be further defined as

$$\boldsymbol{\Pi}^*_{neq} = (1+\lambda)\bar{\boldsymbol{\Pi}}_{neq} + \frac{1}{3}(1+\lambda_v)\big(\boldsymbol{\Pi}_{neq}:\mathbf{I}\big)\mathbf{I} \tag{8}$$

Note that $\boldsymbol{\Pi}_{neq} = \boldsymbol{\Pi} - \boldsymbol{\Pi}_{eq}$ and $\bar{\boldsymbol{\Pi}}_{neq}$ is the traceless component of $\boldsymbol{\Pi}_{neq}$. The tensor $\boldsymbol{\Pi}_{eq}$ is the equilibrium momentum flux and is computed as

$$\boldsymbol{\Pi}_{eq} = \rho c_s^2 \mathbf{I} + \rho \boldsymbol{u}\boldsymbol{u} \tag{9}$$

Finally, λ and λ_v are two relaxation parameters for the collision operator and are related to shear and bulk viscosities μ and μ_v, respectively, as

$$\mu = -\rho c_s^2 \Delta t \left(\frac{1}{\lambda} + \frac{1}{2}\right) \tag{10}$$

$$\mu_v = -\rho c_s^2 \Delta t \left(\frac{2}{3\lambda_v} + \frac{1}{3}\right) \tag{11}$$

Although two distinct relaxation parameters are defined, λ_v is set at -1 usually. Furthermore, LBM is weakly compressible and the Mach number defined $Ma = u/c_s$ needs to be kept below 0.15 to maintain the incompressibility condition. Also, note that Δx and Δt are both typically set to 1 for this work.

Forcing term is added to the collision operator to allow force density $\boldsymbol{g}$ to be applied throughout the model [61]. This is an equivalent operation to applying a unidirectional and constant pressure gradient throughout the model. The forcing term $g_i(\boldsymbol{r}, t)$ is added as

$$f_i(\boldsymbol{r} + \boldsymbol{c}_i\Delta t, t + \Delta t) = f_i^*(\boldsymbol{r}, t) + g_i(\boldsymbol{r}, t) \tag{12}$$

$$g_i(\boldsymbol{r}, t) = \left(1 + \frac{\lambda}{2}\right) a^{\boldsymbol{c}_i} \left[\frac{\boldsymbol{g} \cdot \boldsymbol{c}_i}{c_s^2} + \frac{(\boldsymbol{g}\boldsymbol{u} + \boldsymbol{u}\boldsymbol{g}) : (\boldsymbol{c}_i\boldsymbol{c}_i - c_s^2\mathbf{I})}{2c_s^4}\right]\Delta t \tag{13}$$

Note that $f_i^*(\boldsymbol{r}, t)$ is the post-collision distribution function without forcing term applied. Furthermore, with forcing term applied, a more accurate momentum and fluid velocity $\boldsymbol{j}'$ and $\boldsymbol{u}'$, respectively, are calculated as

$$\boldsymbol{j}' = \rho\boldsymbol{u}' = \sum_i f_i\boldsymbol{c}_i + \frac{\boldsymbol{g}\Delta t}{2} \tag{14}$$

2.2 Lattice spring model

For solid mechanics of the model, the lattice spring model (LSM) is employed [62, 63]. This model discretizes elastic solid surfaces via a network of masses connected by stretching and bending springs. Although LSM is a simpler implementation of other solid

mechanics solver like the finite element methods (FEM), LSM is shown to be equivalent to FEM in certain cases [64].

The LSM lattice can be arranged in different ways. However, different lattices may yield different elastic properties, and equilateral triangular and square lattices were demonstrated to behave like an isotropic elastic solid [65]. For this work, the spring network is arranged in equilateral triangular lattices. A typical triangular lattice is shown below at Figure 2.2.

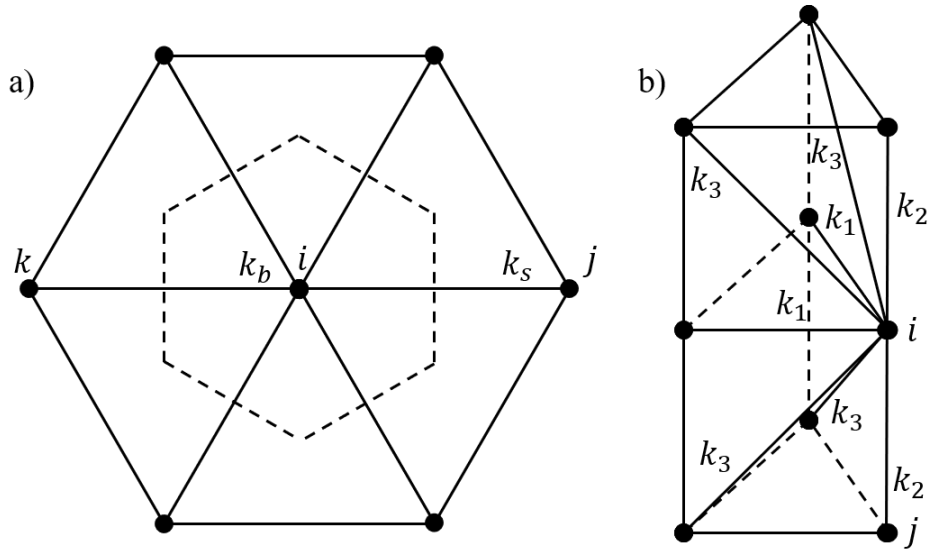

Figure 2.2 a) A single cell of a two-dimensional triangular LSM lattice. The dashed hexagon notes the boundary of a unit cell surrounding node i. Nodes with masses are represented in circles while solid lines indicate spring connections between neighboring nodes. For each pair of node-to-node connection like ij pair, a stretching spring of stiffness k_s is applied while a colinear triple like kij creates a set for bending spring with stiffness k_b. b) A segment of three-dimensional triangular prism lattice. A node i connects to 20 neighboring nodes but is shown to be connected to only a fragment of the entire connection due to only one-sixth of the entire network shown. Same rule for creating stretching pair and bending triple applies as in the two-dimensional cases. However, the stretching spring constants differ depending on whether the node pair connects two nodes on the same triangular layer (k_1), two nodes on different triangular layer but vertically above or below (k_2), or two nodes on different layers with diagonal connection (k_3).

For this study, a two-dimensional triangular lattice plates are used to represent thin elastic bodies like flexible lymphatic valves or boundaries of lymphatic vessels. Three-dimensional triangular lattice is only used for creation of filarial worm model. Three-dimensional triangular lattice is represented as stacks of two-dimensional lattice with each layer consisting of equilateral triangular lattice like in the two-dimensional case [66].

For stretching springs, the relationship between stretching force $\boldsymbol{F}_{s,ij}$, internode distance between node i and j, and stretching stiffness can be described as

$$\boldsymbol{F}_{s,ij} = -k_s\left(l_{ij} - l_0\right)\hat{\boldsymbol{r}}_{ij} \tag{15}$$

Note that l_{ij} denotes the distance between nodes i and j, l_0 denotes equilibrium length of the spring, and $\hat{\boldsymbol{r}}_{ij}$ is the unit vector in from i to j. For two-dimensional triangular lattice, the Young's modulus e is defined as $e = 2k_s/\sqrt{3}h$, where h is the thickness of the elastic sheet [63, 67] like the lymphatic valve. Poisson ratio for two-dimensional lattice is set at $\nu_p = 1/3$. Note that because typical biological tissues have Poisson ratio close to 0.5, this could create a possible limitation and inaccuracy of the model.

For the three-dimensional lattice, three distinct in-plane stiffness are defined based on the relative location of nodes to each other [66].

$$k_{s,3D} = \begin{cases} k_1 = 2k_c \\ k_2 = k_c \\ k_3 = 2k_c/3 \end{cases} \tag{16}$$

As see in Figure 2.2, stiffness of a pair of nodes on the same layer has the highest stiffness while a diagonally connected nodes between different layers have the lowest value. Note

that three distinct stiffness are related through a common stiffness factor k_c, which is related to the Young's modulus as $e_{3D} = 5k_c/\sqrt{3}a_{0,3D}$, where $a_{0,3D}$ is the lattice spacing. Finally, the Poisson ratio for three-dimensional lattice is set at $\nu_{p,3D} = 1/4$.

Bending springs are also added for the spring network since studies of heart valves suggested that bending stiffness could play a major role in valve susceptibility to deformation [68-70]. Like the in-plane spring, bending springs are modeled with a series of bending springs with each spring made up of three collinear LSM nodes in undeformed states. This method of defining bending triple applies the same in both two-dimensional and three-dimensional lattices. Bending spring stiffness k_b determines the degree of out-of-plane bending resistance for the triple nodes and is related to bending energy U_b as

$$U_b = k_b(cos\theta_{kij} - cos\theta_0) \tag{17}$$

Note that θ_{kij} represents an angle that kij triple from Figure 2.2a makes while θ_0 is the angle of the triple under undeformed state, typically set at $\theta_0 = \pi$. Bending forces $\boldsymbol{F}_b$ on each of the triple nodes are distributed as

$$\boldsymbol{F}_{b,k} = -\frac{k_b}{l_{ij}l_{ik}}\left(\boldsymbol{r}_{ij} - \frac{cos\theta_{kij}}{r_{ik}^2}\boldsymbol{r}_{ik}\right) \tag{18}$$

$$\boldsymbol{F}_{b,j} = -\frac{k_b}{l_{ij}l_{ik}}\left(\boldsymbol{r}_{ik} - \frac{cos\theta_{kij}}{r_{ij}^2}\boldsymbol{r}_{ij}\right) \tag{19}$$

$$\boldsymbol{F}_{b,i} = -(\boldsymbol{F}_{b,j} + \boldsymbol{F}_{b,k}) \tag{20}$$

Note that vector between two nodes is noted in $\boldsymbol{r}$. For example, $\boldsymbol{r}_{ij}$ notes a vector from node i to j. For a two-dimensional triangular lattice, plate bending rigidity d_b is related to bending stiffness as $d_b = 3\sqrt{3}k_b/4$, where $d_b = eh^3/12(1-v_p^2)$ [62, 66].

2.2.1 Solid body dynamics

The dynamics of solid domain is calculated through time-integration of Newton's equation of motion.

$$\boldsymbol{F}_i = M_i \frac{d^2\boldsymbol{r}_i}{dt^2} \tag{21}$$

Here, $\boldsymbol{F}_i$ is the total force applied a given node position i, M_i is the mass of node i, and $\boldsymbol{r}_i$ is the position vector of node i. Note that total force is calculated as a sum of spring forces, consisting of stretching (in-plane) and bending forces, interfacial forces between fluid and solid nodes, and any external forces prescribed. Overall, $\boldsymbol{F}_i$ can be described as

$$\boldsymbol{F}_i = \boldsymbol{F}_{s,i} + \boldsymbol{F}_{b,i} + \boldsymbol{F}_{int,i} + \boldsymbol{F}_{e,i} \tag{22}$$

Note that $\boldsymbol{F}_{int,i}$ is the interfacial force applied to node i while any prescribed force onto node i is written as $\boldsymbol{F}_{e,i}$.

Once the total force is found, the equation of motion is integrated through Verlet algorithm [71]. To integrate from t to $t + \Delta t$, solid node acceleration $\boldsymbol{a}_i(t)$ and velocity at half step $\boldsymbol{v}_i(t + \frac{\Delta t}{2})$ are first calculated as follows:

$$\boldsymbol{a}_i(t) = \boldsymbol{F}_i(\boldsymbol{r}_i(t), t)/M_i \tag{23}$$

$$\boldsymbol{v}_i\left(t + \frac{\Delta t}{2}\right) = \boldsymbol{v}_i(t) + \boldsymbol{a}_i(t)\frac{\Delta t}{2} \tag{24}$$

Then, a new position at $t + \Delta t$ is computed using the velocity at half step:

$$\boldsymbol{r}_i(t + \Delta t) = \boldsymbol{r}_i(t) + \boldsymbol{v}_i\left(t + \frac{\Delta t}{2}\right)\Delta t \tag{25}$$

Finally, acceleration and velocity at new time step are calculated:

$$\boldsymbol{a}_i(t + \Delta t) = \boldsymbol{F}_i(\boldsymbol{r}_i(t + \Delta t), t)/M_i \tag{26}$$

$$\boldsymbol{v}_i(t + \Delta t) = \boldsymbol{v}_i\left(t + \frac{\Delta t}{2}\right) + \boldsymbol{a}_i(t + \Delta t)\frac{\Delta t}{2} \tag{27}$$

2.3 Fluid-structure coupling

LBM and LSM models are coupled through the use of two-way coupling at the fluid-solid boundary. Momentum is imparted from solid surfaces onto the fluid through use of an interpolated bounce-back boundary method on a no-slip and no penetration surface, and momentum is conserved by the application of corresponding forces onto the solid nodes [53, 54]. This method of coupling has been successfully and extensively validated in several previous studies [72-77].

When imparting momentum from LSM surfaces to LBM nodes, interpolated bounce-back rule is necessary as solid surfaces will be unlikely to be positioned exactly halfway between two neighboring LBM nodes. The method first defines a wall distance

q_{int}, which is the distance between a given LBM node and an LSM surface in the direction of $\boldsymbol{c}_i$. Then, a bounce-back method depending on the value of q_{int} is implemented as shown below

$$f_{i'}(\boldsymbol{r}, t+\Delta t) = 2q_{int} f_i^*(\boldsymbol{r}, t) + (1-2q_{int}) f_i^*(\boldsymbol{r}-\boldsymbol{c}_i, t), \quad q_{int} < 1/2 \tag{28}$$

$$f_{i'}(\boldsymbol{r}, t+\Delta t) = \frac{1}{2q_{int}} f_i^*(\boldsymbol{r}, t) + \frac{2q_{int}-1}{2q_{int}} f_{i'}^*(\boldsymbol{r}, t), \quad q_{int} \geq 1/2 \tag{29}$$

Note that f_i^* denotes distribution function after collision while $f_{i'}$ indicates a distribution function in the opposite direction to the given velocity distribution direction of i. To account for a moving LSM surface of velocity $\boldsymbol{u}_b$, additional term of $-2a^{\boldsymbol{c}_i}\rho \boldsymbol{c}_i \cdot \boldsymbol{u}_b / c_s^2$ is added to $f_{i'}(\boldsymbol{r}, t+\Delta t)$.

Once the momentum exchange is complete on LBM side, the difference in momentum exchanged on the fluid domain is applied onto the solid domain as solid-fluid interfacial force $\boldsymbol{F}_{int}$. This force is defined as

$$\boldsymbol{F}_{int}(\boldsymbol{r}_b, t+\frac{1}{2}\Delta t) = \frac{\Delta x^3}{\Delta t}\left[f_i^*(\boldsymbol{r}, t) + f_{i'}^*(\boldsymbol{r}, t+\Delta t)\right]\boldsymbol{c}_i \tag{30}$$

Note that $\boldsymbol{r}_b$ is the intersection point on LSM surface where LBM propagation from a given LBM node in the direction of $\boldsymbol{c}_i$ intersects. Once the total interfacial force is calculated, it is distributed to nearby LSM nodes that make up the surface based on its distance from the point of intersection. Overall, this method of solid-fluid coupling conserves momentum of the entire model since the exact amount of momentum changed in fluid domain are applied as interfacial forces onto the solid domain.

CHAPTER 3. LYMPHATIC VALVE IN A RIGID VESSEL

3.1 Introduction

In this chapter, we model the lymphatic vessel wall as rigid and introduce a uniaxial pressure gradient that varies with a prescribed pressure waveform to mimic the flow generated by a contracting lymphatic vessel. These simplifying assumptions allow us to isolate the effects of valve morphology on its function. The effect of vessel contractility and more complicated dynamic pressure variations, both of which may also play important roles in valve efficacy, will be explored in later chapters.

FSI studies of cardiac valve behavior have been used to significantly increase understanding of cardiac valves [78-80] compared to more simplified approaches. Similar gains in knowledge of lymphatic valve behavior are anticipated when compared to simplified approaches. Ultimately, the findings are to complement results from lumped parameter lymphatic studies to increase our understanding of lymphatic system behavior, and to provide insights into how valve defects can lead to lymphatic dysfunctions.

3.1.1 Rigid wall model

In this chapter, we model the lymphatic vessel as a stationary fluid-filled cylinder and, based on Davis, Rahbar [8], assume the valve leaflets in their unstressed state as the section of a plane interior to the intersection of the plane with the cylindrical vessel (Figure 3.1a-b). The free leaflet tip is given a crescent shape through removal of a circular section of diameter d from the end of the valve, reflecting the geometry typical for lymphatic valve

leaflets found physiologically (Figure 3.1c). The valve leaflet is fixed at its perimeter to the vessel wall, whereas the interior and the tip are allowed to move freely.

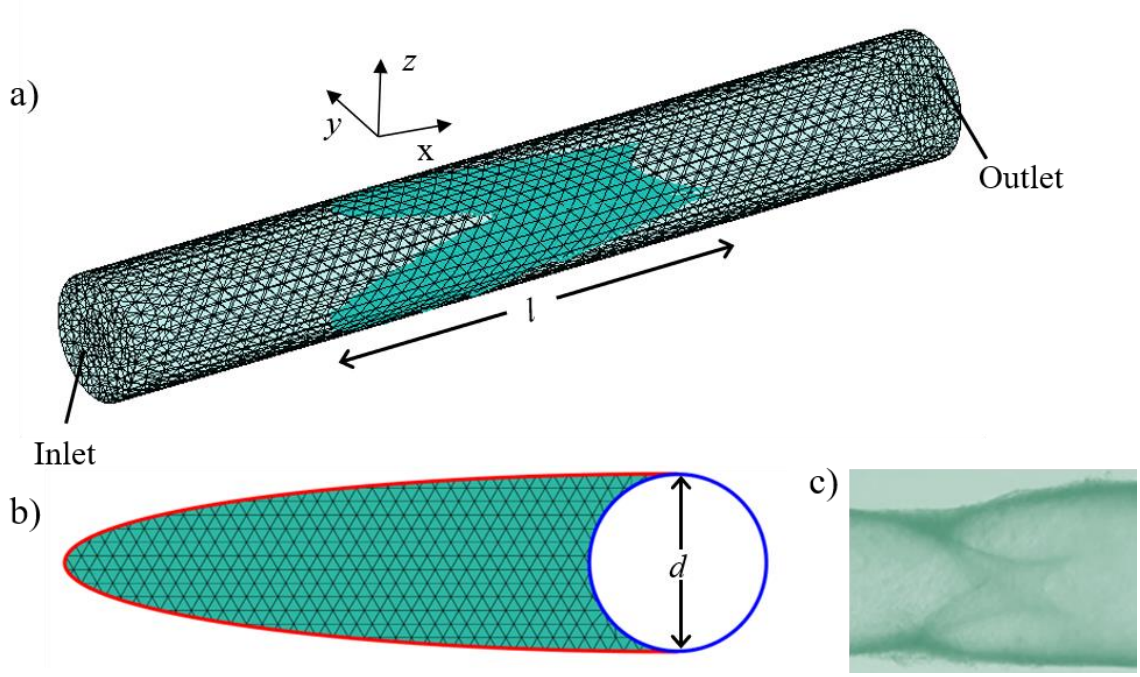

Figure 3.1 a) Simplified geometric model of a lymphangion consisting of a cylindrical vessel and valve. Note that the semicircular cutout can look elliptical when viewed from an angle. b) Shape and dimensions of the valve leaflet from Fig 3.1a. The red line marks the locations at which the valve leaflets are attached to the vessel walls, and the blue circle marks the region removed from the geometry to give it a crescent shape. c) Image of a lymphatic vessel segment containing a valve, given as a comparison to our simplified model.

The fluid domain is subjected to periodic boundary conditions in the axial flow direction, simulating an infinitely long repeating series of lymphangions. The periodic boundary conditions are implemented for the distribution functions exiting the domain by reintroducing these functions on the opposite side of the domain. A body force is used to impose a pressure gradient in the flow leading to a pressure drop $\Delta P_{app}(t)$ across the length of the channel.

Leaflet contact during valve closure was achieved by creating a no-penetration boundary at the center plane between the two leaflets, thus avoiding possible numerical instability caused by contacts between solid nodes while allowing satisfactory valve closure to prevent backflow.

3.1.2 Relevant operating conditions of lymphatic system

Understanding lymphatic biomechanics is a challenging task. Experimental studies on the lymphatics are scarce, in large part due to the difficulty of locating and handling lymphatic vessels. Lymphatic vessels are not as easily identifiable since they are clear (i.e. not filled with blood). Additionally, lymphatic vessels are quite fragile. For example, collecting lymphatics in the rat range in diameter from $80\sim800$ μm, with a wall thickness of $10\sim40$ μm. While measurements of lymphatic wall mechanics and muscle force generation have been occasionally reported in the literature [81-83], measurements of lymphatic valve opening and closing properties are very rare [8], and no measurements exist of lymphatic valve mechanical properties.

Despite the scarcity, some of the reported physiological values of relevant operating parameters are provided in Table 3.1 as a reference. Note that Cauchy number represents a ratio between dynamic pressure force from fluid and elastic force [84-88]. Unlike the typical Cauchy number which calculates contribution of stretching force, we define a modified Cauchy number that compares the pressure force against elastic force from bending. The modified Cauchy number is defined as $Ca = (\rho d^3 U_c^2)/d_b = (d\mu^2 Re_r^2)/(\rho d_b) = (12 d\mu^2(1-v_p^2)Re_r^2)/(\rho e h^3)$, where vessel diameter d is used as characteristic length, and characteristic velocity U_c is replaced with and adjusted with Reynolds number

in a rigid vessel Re_r. Finally, ρ and μ represent fluid density and dynamic viscosity, respectively.

Table 3.1 Table of referenced operating conditions

Operating Conditions	Typical Experimental Values	Reference
Valve length (μm)	$230\sim2800$ (est.)	[20, 21]
Vessel diameter (μm)	$100\sim2800$	[19-21]
Valve thickness (μm)	$0.5\sim6$	[89]
Pressure drop (Pa)	$0\sim200$	[8]
Young's modulus (kPa)	$1.25\sim7.5$	[19]
Reynolds number	< 16	[22, 23]
Womersley number	< 1.4	[22, 23]
Cauchy number	< 4800	[19, 84]
Note: Measured lymphatic valve diameter and length from Figure 3.2 were not specifically noted since the values are within the ranges for respective parameters. [8] and [21] used rat mesenteric lymphatic vessels. [20] used lymphatic vessels from human legs. [19] used bovine mesentery lymphatic vessels. [89] used adult rabbit lung's lymphatic vessels. Cauchy number is calculated from average d from Figure 3.2 and average Young's modulus and valve thickness from Table 3.1. v_p is set at 0.5 for biological materials.		

3.1.3 Nondimensional number and simulation parameters

Note that in lattice-Boltzmann simulations, physical parameter values are derived from relationships between lattice-Boltzmann simulation parameters and are not explicitly specified in the model. Thus, to compare our simulation results with relevant experimental systems, we match dimensionless parameters characterizing the system including the aspect ratio, Reynolds number, Womersley number, $K_{b,r}$, and $K_{s,r}$. Dimensionless

parameters corresponding to the physiological ranges of physical parameters as listed in Table 3.1 were used in our simulations.

We first consider the aspect ratio $AR = l/d$ of the lymphatic valves, where l is the length of the valve, and d is the vessel diameter at the base of the valve, or the valve width, as shown in Figure 3.1b. We also consider a dimensionless bending stiffness parameter $K_{b,r} = 160k_b/\sqrt{3}\pi d^3\Delta P_{app}$, which represents the balance between elastic forces and pressure forces on the valve. The normalized in-plane stiffness is given by $K_{s,r} = k_s/\Delta P_{app} d = \sqrt{3}eh/2\Delta P_{app} d$, where e is Young's modulus, and h is valve thickness. Unless specified otherwise, we set $K_{s,r} = 0.1$ for the simulations. The value of $K_{s,r}$ is chosen by using the averages of physiological parameter values from Table 3.1.

The lymphatic system operates at a low Reynolds number, $Re_r = \rho U d/\mu$, where the flow is dominated by the fluid viscosity. Here, μ and ρ are the dynamic viscosity and density of the fluid, respectively. In our simulation, the largest values of the Reynolds number calculated based on the fastest flow velocity U_{max} does not exceed $max\ (Re_r) \approx 0.7$. While low values of Re_r are typical for the lymphatic experimental studies [22], wide variation of lymphatic valve and vessel properties such as the vessel diameter [19-21] make it possible for lymphatic flows to have a Reynolds number greater than unity [23]. In such a case, inertial effect could play a more significant role than in our simulations. In our dynamic simulations, we use the Womersley number $Wo = d/2\sqrt{\omega\rho/\mu} = 0.11$, where ω is the angular frequency of the applied dynamic pressure difference. The relatively low Wo corresponds to flow conditions characteristic to the lymphatic system [22, 23]. Note that our computational model explicitly accounts for inertial effects on both fluid and solid

mechanics. Finally, Cauchy number for the model is calculated based on $Ca = (d\mu^2 Re_r^2)/(\rho d_b)$. For Re_r, the average flow velocity for a valve-less, rigid vessel under ΔP_{app} is used, which gives $Re_r = 0.2$ and $Ca < 0.2$. The large variation of Ca from Table 3.1 can be explained from the difference in Re_r, which has a quadratic relationship with Ca. In fact, once the numerical operating range of $Re_r = 0.2$ is applied to recalculate Ca in Table 3.1, the recalculated Ca is around 0.8, which is within an order of magnitude from the numerical counterpart.

To characterize the resistance of lymphatic valves to forward fluid flow, we introduce the flow resistance R_r using an analogy to Ohm's law, $\Delta P_{app} = Q_{steady} R_r$. Here, ΔP_{app} is the imposed pressure drop across the vessel length and Q_{steady} is the calculated resulting steady-state volumetric flow rate. We calculated the valve flow resistance $R_{valve} = R_{total} - R_{vessel}$, where R_{total} is the total resistance of the vessel and valve to flow, as calculated from simulation data, and R_{vessel} is the flow resistance of a valve-less vessel section based on Poiseuille approximation and validated through simulation of a valve-less vessel segment. The ratio R_{valve}/R_{vessel} gives the relative resistive effects of the valve and vessel on flow. When $R_{valve}/R_{vessel} < 1$, the valve causes less flow resistance than does the vessel, while the opposite is true for $R_{valve}/R_{vessel} > 1$. A Poiseuille approximation of the valve-less vessel flow is appropriate given the low Womersley number flow under the conditions in this study, and further has been shown to be an appropriate approach for the low Reynolds number associated with lymphatic flow in regions away from valve segments [22, 34]. Under backflow conditions, valve closing should prevent fluid leakage. To characterize the ability of valves to resist leakage during the backflow, we introduce the fluid conductance $C = 1/R_r$. The valve

conductance $C_{valve} = 1/R_{valve}$ is normalized by the conductance in an equivalent valve-less vessel, $C_{vessel} = 1/R_{vessel}$, to give the relative effects of the valve and vessel on conductance of flow.

For model dimensions, note that all dimensional values are given in lattice Boltzmann units, if not indicated otherwise. In our model, the vessel has constant length $L_{vessel} = 150$ and diameter $d = 20$ and is contained within a rectangular computational domain. The vessel is filled with fluid of density $\rho = 1$ and kinematic viscosity $\nu = 1/6$. The valve leaflets are constructed of springs arranged on an equilateral triangular lattice with equilibrium length $L_{eq} = 1.78$. The mass of each solid node is calculated to correspond to the approximate valve mass, based on the average lymphatic valve thickness reported by Lauweryns and Boussauw [89]. Under steady-state simulators, we consider a constant pressure drop $\Delta P_{app} = 1/300$, whereas $\Delta P_{app}(t)$ changes following a trapezoidal waveform in dynamic simulations. The wave form is characterized by the maximum pressure drop $\Delta P_{app,max}$.

3.1.4 Convergence analysis

Even though LBM, LSM, and coupling method have been successfully and extensively validated in several previous studies [72-77], additional numerical validation is required to determine the accuracy of model resolution. Thus, a convergence analysis of both the LBM and LSM components of the simulated model was conducted. Deviation of average velocity and leaflet opening at the center were used to analyze the convergence for LBM and LSM, respectively, and approximately 2% deviation in both average velocity

and leaflet opening were found when the resolution was doubled, supporting that the current grid is sufficiently accurate for the study conditions.

To our knowledge, analysis of this chapter was the first time that the three-dimensional dynamics of collecting lymphatic valves has been successfully modeled using two-way coupling of fluid mechanics and solid mechanics models. Thus, this simplified model of collecting lymphatic valves represents a significant step above the previous research and provides a means to study the effects of basic system parameters on dynamic valve behavior and on fluid resistance.

3.2 Effect of valve aspect ratio

When first studying the effect of valve aspect ratio and mechanical properties, we performed numerical simulations in which a steady pressure gradient was applied in either the favorable or adverse axial direction down a vessel containing a lymphatic valve. While a steady pressure gradient is not physiological, its application in this context allows for one to easily appreciate the influence of relevant valve parameters on its resistance. A favorable pressure gradient drives flow in the forward direction from left to right and causes the valve to open. Conversely, an adverse pressure gradient drives flow in the backward direction from right to left and causes the valve to close. We simulated flow through vessels of constant geometry containing valves of different length, so as to represent geometries with varied valve aspect ratio.

3.2.1 Survey of experimental data on valve geometry

As indicated by previous studies, lymphatic valves come in varied geometries. For example, the valve aspect ratio varies widely across species and vessel location. In a brief survey of valves from vessel segments that we excised from rats and sheep, we observed this aspect ratio to vary over the range of approximately $1.15 < AR < 3$, shown in order of increasing aspect ratio in Figure 3.2. While these data do not conclude that valves always fall into this range of aspect ratio, they provide a guideline for an aspect ratio range over which we focus our simulations. The experimental method of obtaining the valves' geometric profiles is detailed in [49].

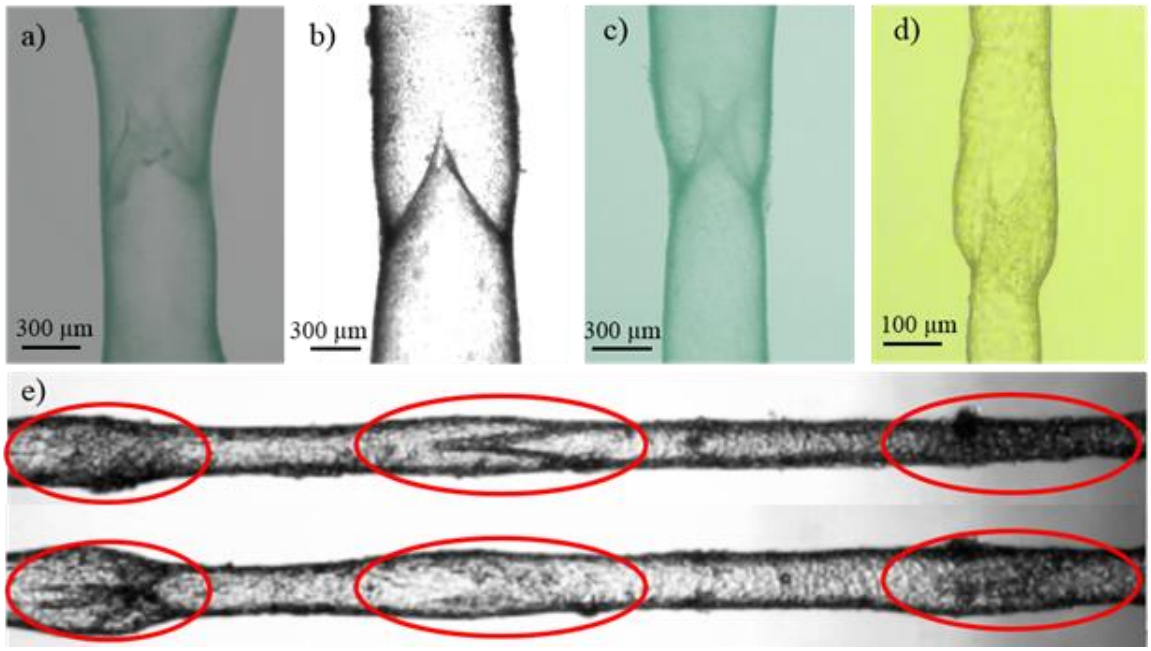

Figure 3.2 Images of lymphatic vessels with valves, excised from various vessel locations and species, given in order of increasing aspect ratio. a) rat thoracic duct: $d \approx 550\mu m$, $L \approx 640\mu m$ and $AR \approx 1.15$, b) sheep popliteal lymphatic vessel: $d \approx 650\mu m$, $L \approx 810\mu m$ and $AR \approx 1.25$, c) rat cervical lymphatic vessel: $d \approx 440\mu m$, $L \approx 660\mu m$ and $AR \approx 1.5$, and d) rat mesenteric lymphatic vessel: $d \approx 110\mu m$, $L \approx 295\mu m$ and $AR \approx 2.7$. e) Two rat tail lymphangions (valves noted in red) in series with $d \approx 220\mu m$, $L \approx 660\mu m$, and $AR \approx 3$. The upper image shows the closure of the central valve with other valves open, while the lower image shows the same lymphangions but with the central valve now open and the other two valves closed. This shows how lymphangions in a chain work together to create a unidirectional flow.

3.2.2 Flow resistance variation, forward flow

Figure 3.3a presents the normalized valve flow resistance over a range of AR with two different values of $K_{b,r}$ under a favorable pressure gradient. We find that the normalized resistance of an open valve to forward flow increases monotonically with aspect ratio. This is because long valves (i.e., valves with a large aspect ratio) have longer constricted regions than short ones, thus leading to increased flow resistance. Consequently, from the perspective of purely minimizing resistance to forward flow, low aspect ratio valves would be the optimal configuration. We found that lymphatic valves in fact do tend toward the limit of a low aspect ratio, as the majority of the physiological valves that we considered have aspect ratios close to unity, as seen by labels a-c in Figure 3.3a.

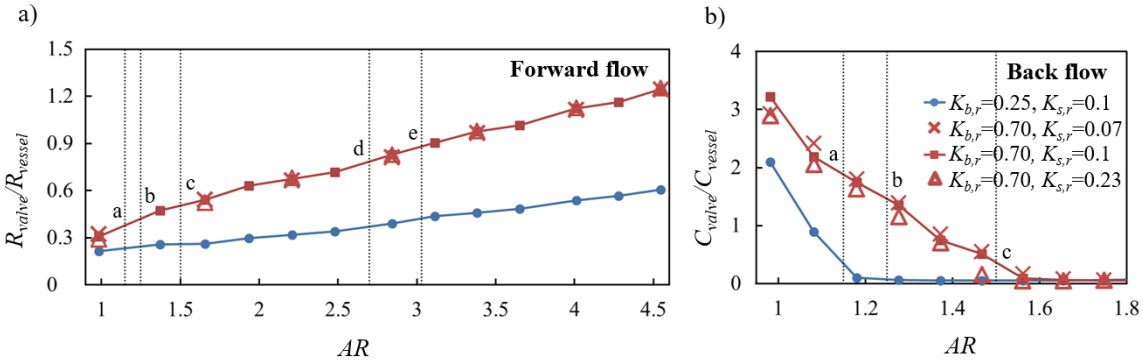

Figure 3.3 Plot of normalized valve resistance and conductance of lymphatic valves to forward and backward flow, respectively, for various aspect ratios AR for a fixed vessel size and normalized stiffness values of $K_{b,r} = 0.25$ and $K_{b,r} = 0.7$. a) Normalized resistance to forward flow. The markings a-e and dotted vertical lines correspond to the aspect ratios of the valves shown in Figure 3.2a-e, respectively. Also note that $K_{s,r}$ is varied between $K_{s,r} = 0.07$ and 0.23 for selected values of AR at $K_{b,r} = 0.7$. b) Normalized conductance to back flow. Labels for d and e are not shown as the solution converges to zero for $AR > 1.5$. The same $K_{s,r}$ variation is studied for selected values of AR at $K_{b,r} = 0.7$ as was used in a).

3.2.3 Flow resistance variation, backward flow

To provide a net pumping effect, lymphatic valves must not only allow forward flow, but they must also effectively resist backward flow. Thus, we examined the ability of lymphatic valves of varied aspect ratio to prevent backflow. In Figure 3.3b, we report the calculated normalized fluid conductance, which gives a measure of the ability of fluid to flow through the valve. The conductance is calculated over a range of AR for two values of $K_{b,r}$. We found that in the limit of small aspect ratios the valve leaflets are too short to be able to fully occlude the vessel upon valve closure, allowing significant backflow as indicated by nonzero conductance in Figure 3.3b. However, as the valve aspect ratio is increased, the valve is able to close more fully to effectively block backflow, as is seen by the near-zero conductance above a critical aspect ratio AR_{cr}, whose value is dependent on the valve stiffness. Thus, lymphatic valves should be of an aspect ratio greater than AR_{cr} to effectively block backflow. Interestingly, some of the lymphatic valves shown in Figure 3.2 fall near the critical aspect ratio range we found in the simulations, as indicated by the letters a-c on Figure 3.3b.

Thus, functional lymphatic valves must balance having a low enough aspect ratio to reduce resistance to forward flow, while still maintaining a high enough aspect ratio to fully close and prevent backflow. This explains why the majority of the physiological valves which we have observed in our limited sample size (Figure 3.2) fall into a limited aspect ratio range, as seen in Figure 3.3. Furthermore, if we assume that lymphatic valve geometry is optimized to both facilitate forward flow and limit backward flow, our results suggest that the stiffness of physiological valves is likely such that it will result in

dimensionless values close to the range of those considered in our study.

We note that actual geometrical configurations observed physiologically may differ from the critical aspect ratio for proper valve closing and backflow prevention as predicted in this study. This is expected since valve aspect ratios are approximated with some uncertainly, due to dynamic changes in the vessel diameter resulting from the significant contraction and expansion inherent to lymphatic vessels. This could in fact change the effective aspect ratio for a given valve. For example, Figure 3.3 does not indicate proper valve closure under back flow with $AR < 1.2$. However, in actual valves, the lymphatic vessel contracts during the phase in which the valve must prevent backflow. This means that the effective aspect ratio in fact will be much larger than 1.2 under backflow even for valves with an aspect ratio close to 1 under passive conditions. This indicates that valves with $AR < 1.2$ in an inflated state can still close properly due to vessel contraction. Furthermore, reported regional heterogeneity within the lymphatic system has been suggested to occur as a result of adaptations of the vessel to the natural loading conditions that it experiences in vivo [82, 90, 91]. Thus, valves that do not routinely encounter large unfavorable pressure gradients may have developed valve geometries that are less adept at preventing backflow.

3.3 Effect of valve mechanical properties

The dependence of AR_{cr} on valve bending stiffness, as seen in the difference between the two curves on Figure 3.3b, also suggests that AR is not the only factor vital to valve closing function. Furthermore, analysis of flow resistance for different AR under different in-plane stiffness demonstrated that valve's bending stiffness will be a key factor

in variation of valve's flow resistance. Thus, we performed simulations of both high and low aspect ratio valves ($AR = 3.4$ and $AR = 1.7$, respectively) over a range of normalized bending stiffness, $K_{b,r}$.

3.3.1 Flow resistance variation, forward flow

As seen in Figure 3.4, the resistance of the valve to forward flow increases monotonically with $K_{b,r}$. This is due to the fact that flexible valves deflect more readily than stiff valves, allowing them to open more fully, thus reducing fluid resistance to forward flow.

In the limit of infinitely stiff valves, fluid flow is not able to deform valve leaflets and the flow resistance is defined by the valve geometry in the unstressed condition. To evaluate the limiting values corresponding to the valves with extremely high stiffness, we simulated flow through rigid valves of each aspect ratio. Thus, the normalized resistance of valves converges with increasing elasticity to the values $R_{valve}/R_{vessel} = 1.2$ and $R_{valve}/R_{vessel} = 6$, for $AR = 1.7$ and $AR = 3.4$, respectively. As seen from previous analysis of valve resistance in different valve aspect ratios, low aspect ratio valves have lower limiting resistance values than higher aspect ratio valves, due to the fact that lower aspect ratio valves provide a shorter constriction than do higher aspect ratio valves.

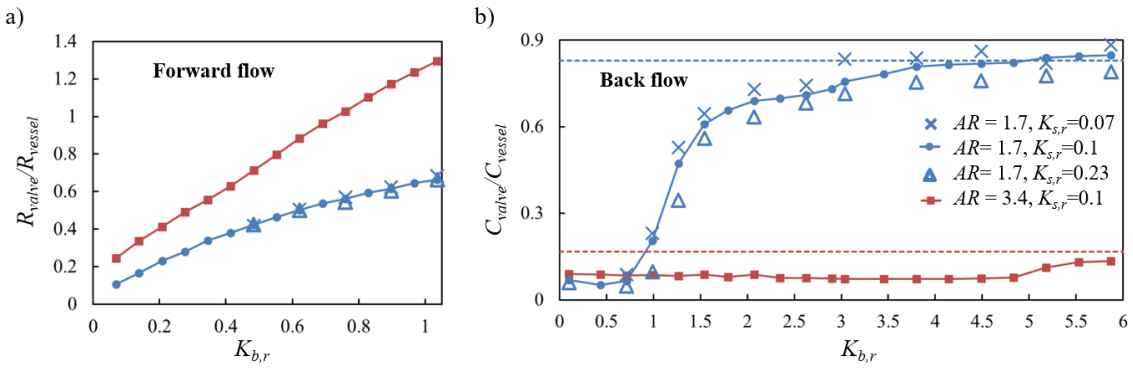

Figure 3.4 a) Normalized valve resistance to forward flow for $AR = 1.7$ and $AR = 3.4$, plotted against normalized bending stiffness. As in Figure 3.3, a segment of various $K_{b,r}$ at $AR = 1.7$ was varied in $K_{s,r}$. b) Normalized valve conductance to backflow against normalized bending stiffness for the same aspect ratios as in a). The asymptotic dashed lines indicate the limit of normalized conductance in the limit of a completely rigid valve. Note the normalized conductance's convergence to its limiting value at high stiffness.

3.3.2 Flow resistance variation, backward flow

As seen in Figure 3.4b, more flexible valves result in low backflow conductance for valves of both $AR = 1.7$ and $AR = 3.4$. As valves become stiffer, they are less easily closed by pressure drops across the valve, and thus are less effective in preventing back flow. For example, valves with $AR = 1.7$ and normalized stiffness above about $K_{b,r} = 1$ yielded a dramatically increasing conductance of backflow with increasing $K_{b,r}$, as seen in Figure 3.4b. Valves of higher aspect ratio are able to function with higher stiffness than those of lower aspect ratio, as seen by the conductance curve for $AR = 3.4$ in Figure 3.4b. However, increasing stiffness will eventually introduce backflow in all valve sizes, as extremely stiff valves will remain in their initially flat position.

Thus, fluid conductance under backflow conditions would be expected to converge to a limit corresponding to a rigid valve, as shown by the dashed lines in Figure 3.4b for the two valve geometries. Low aspect ratio valves reach the threshold of increased

conductance at a lower stiffness value than higher aspect ratio valves because they must deflect further than higher aspect ratio valves in order to fully close.

Overall, we find that more flexible valves are best both for allowing forward flow and for preventing backflow, although the effect of stiffness is dependent on valve geometry. While the extent to which changes in valve stiffness are an important determinant in the pathogenesis of lymphedema remains completely unexplored, these results suggest that valve stiffening could have a profound effect on overall lymphatic pumping performance.

3.3.3 Role of in-plane stiffness on flow resistance

It is also useful to consider the role of in-plane stiffness in valve behavior under varied valve geometry. Within the range of in-plane stiffness varied, Figure 3.3 shows a minor effect of in-plane stiffness on valve resistance and conductance in forward and backward flows, respectively. The variation of forward flow resistance under varied in-plane stiffness was almost nonexistent, while the conductance in backflow varied slightly, most notably at the transition between zero and nonzero conductance, between $AR = 1.4$ and $AR = 1.6$. Likewise, in-plane stiffness only has a minor effect on valve behavior in Figure 3.4, indicating that bending stiffness is the determining factor in valve deformation. Although this conclusion is solely based on the data of Figure 3.3 and Figure 3.4, this insensitivity to in-plane stiffness is similar to what was suggested by the heart valve study [68, 69, 92].

We also analyzed how the average leaflet area changes from the initial state. This change was calculated to be around 6% and 4% for forward and backward flows for Figure

3.3, respectively. For Figure 3.4, valve area change from the initial state was calculated for both aspect ratios, with average values of 6.2% and 0.7% for forward and backward flow, respectively. This indicates that under the parameters used in this study, there is a limited in-plane stretching of the valve leaflets. For these reasons we focus the main attention in our numerical study on exploring the effect of $K_{b,r}$ rather than $K_{s,r}$. Furthermore, we can extend the assumption of limited effect of in-plane stiffness to the dynamic simulations discussed below where we set $K_{s,r} = 0.1$. This is justifiable since the variation of pressure over time is relatively slow, such that inertial effects in the simulation are negligible, as indicated by a relatively small magnitude of the Womersley number.

3.4 Valve under time-dependent pressure gradient

3.4.1 Introduction

In-vivo lymphatic pressure waveforms are highly dynamic, due to the intrinsic contractility of each individual lymphangion, adjacent lymphangions, and extrinsic tissue motion (e.g., through skeletal muscle contraction). In order to understand the dynamic behavior of lymphatic valves and its effect on fluid flow, we simulated flow driven by a time-dependent pressure drop $\Delta P_{app}(t)$ in a trapezoidal waveform for four cycles, thus obtaining time-periodic valve behavior after an initial transient period. Results of our simulations are shown in Figure 3.5.

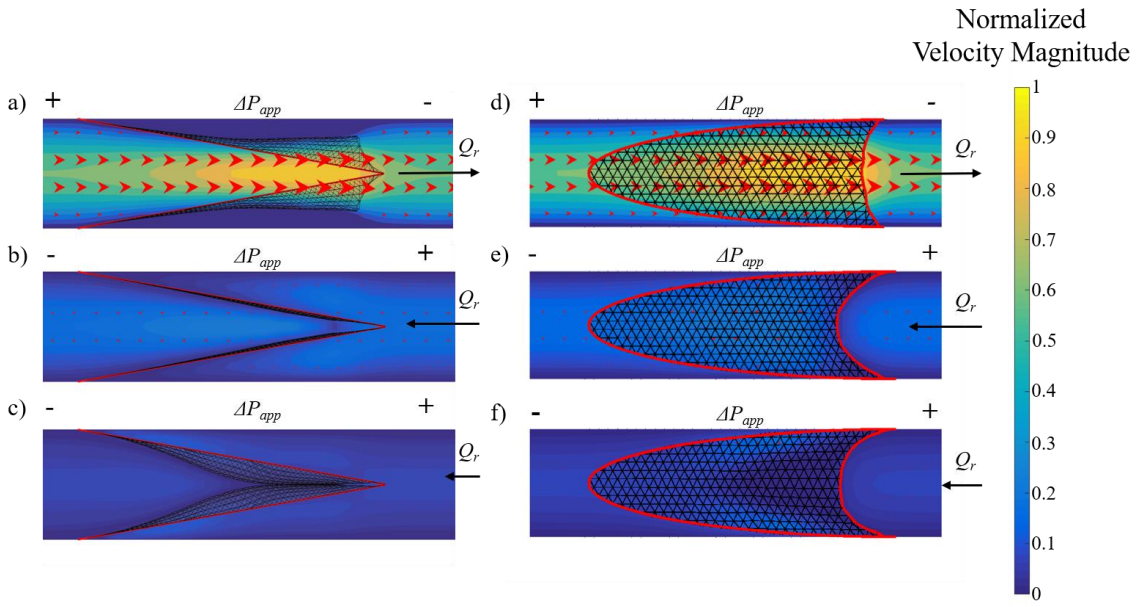

Figure 3.5 a-c) Valve positions, normalized velocity magnitude contour plot and vector field on the x-z plane at the center y-coordinate of the model, as shown in Figure 3.1. The plots show various stages of the lymphatic valve opening and closing cycle induced by a dynamically changing pressure gradient that follows a trapezoidal waveform. Note that the red line outlines where the leaflets are attached to the vessel wall. a) The pressure gradient forces fluid flow in the forward direction, opening the valve. b) The pressure gradient has recently been reversed and the valve is just beginning to close, but backflow is still allowed. c) The pressure gradient has been reversed for sufficiently long that the valve has closed to stop backflow. d-f) Corresponds to a)-c), respectively, but looking at the x-y plane at the center z-coordinate of the model. Note that leaflet edges are outline with the red line.

When $\Delta P_{app}(t)$ propels flow through the vessel from left to right (Figure 3.5a and Figure 3.5d), the valve leaflets deform to open, enabling relatively unobstructed flow. As the pressure gradient is reduced gradually and eventually reversed, the flow starts to slow down, stop, and move from right to left (Figure 3.5b and Figure 3.5e). After a short transient during which the valve remains open allowing backflow (Figure 3.5b and Figure 3.5e), the pressure drop across the valve surface forces it to close (Figure 3.5c and Figure 3.5f), increasing the backflow resistance, or reducing the backflow conductance.

To further analyze the flow behavior, average flow velocity U_{avg} normalized by its

maximum velocity is shown in Figure 3.6. The asymmetric time evolution of U_{avg} indicates that the valve in our model provides a net forward pumping effect. The peak in negative flow velocity reflects a lag in the dynamic closing response of the valve with respect to $\Delta P_{app}(t)$, which is the flow driving force. A qualitatively similar amount of reverse lymphatic flow has been observed experimentally in rat mesenteric lymphatics [22].

The lymphatic flow profile is axially dominated except when the lymphatic valve is fully closed against backflow. Under a forward pressure gradient, the fluid flows through the valve opening and near the central axis of the vessel, with a distinct region of stagnation at the gap between the leaflet and the lymphatic vessel wall. When the flow direction just starts to reverse, similar axially dominated flow develops, but now in the reverse direction. The magnitude of the reverse flow decreases as the leaflets close. In the case of an active lymphatic vessel where vessel contraction and expansion provide for the pressure gradients that drive the flow, the local fluid flow profile would be expected to be more complex than those observed in our simulations. Additionally, it is likely that the valve behavior itself would change due to contraction of the vessel wall near the anchoring points, although it is worth noting that usually the contraction amplitude is lowest near the valve region.

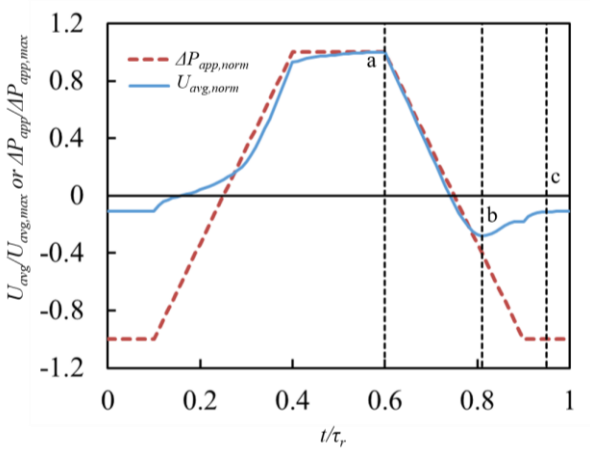

Figure 3.6 Waveform of the normalized average axial velocity (the solid blue line) and the normalized pressure drop, and correspondingly gradient, (the dashed red line) over a cycle of oscillating pressure drop, with the valve ($AR = 2.8$, $K_{b,r} = 0.25$, $K_{s,r} = 0.1$) positions from Figure 3.5a-c denoted with the corresponding letter and with vertical dashed lines. Positive pressure drop indicates pressure driving fluid from left to right, and vice-versa. Time is normalized by the cycle period τ_r.

3.4.2 Valve hysteresis

In order to better understand the dynamic behavior of the valves and how it results in a momentary peak in backflow and affects overall cycle pumping, we further investigated the valve dynamics under a trapezoidal pressure gradient waveform. To do this, time variation of the distance between the center points of the tips of the top and bottom leaflets, referred to hereafter as the gap distance δ_{gap}, is measured.

In Figure 3.7, the time evolution of the normalized gap distance throughout a trapezoidal pressure drop cycle was plotted against the normalized pressure drop for $AR = 2.8$, $K_{s,r} = 0.1$, and valve stiffness values of $K_{b,r} = 0.25$ and $K_{b,r} = 0.7$. In both cases, substantial hysteresis of the gap distance is observed between an increasing and decreasing pressure drop (i.e., back flow to forward flow and forward flow to back flow, respectively),

providing clarity into the delayed valve response to changing flow conditions.

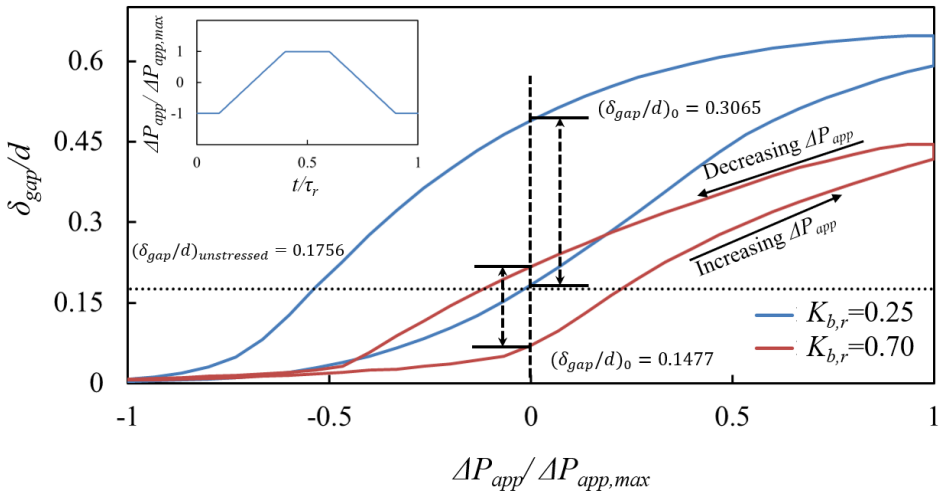

Figure 3.7 Valve gap distance plotted against the normalized pressure drop for a single trapezoidal pressure drop cycle, where the waveform profile is given in a subplot on the top left corner. Gap distance response was plotted for $K_{b,r} = 0.25$ and $K_{b,r} = 0.7$ with $AR = 2.8$, $K_{s,r} = 0.1$. The normalized gap distance difference at zero normalized pressure drop between increasing and decreasing pressure drop segment of the trapezoidal waveform is noted as $(\delta_{gap}/d)_0$. As a reference, normalized gap distance at the unstressed state $(\delta_{gap}/d)_{unstressed}$ is shown by the horizontal dotted line.

Under an increasing pressure gradient that eventually opens an initially closed valve, valve opening lags the increasing pressure gradient. For $K_{b,r} = 0.7$, this lag can be seen near zero pressure drop, which is indicated by the vertical dashed line in Figure 3.7. The gap distance at zero pressure is lower than the gap distance at the unstressed state, which is marked with a horizontal dotted line. This result indicates that the valve is not yet at its unstressed state when the pressure drop increases to a value of zero and flow transitions from the reverse direction to the forward direction. On the other hand, the softer valve ($K_{b,r} = 0.25$) shows minimal delay after changing pressure to this level.

For both values of $K_{b,r}$, the vertical lines at maximum positive pressure drop in

Figure 3.7 show that valves are not fully opened to maximum gap distances when maximum positive pressure is initially reached and require additional time to reach the fully opened state. As seen in Figure 3.7, under a decreasing pressure gradient that eventually closes an initially opened valve, valve closing trails the applied pressure gradient and thus results in a larger gap distance for a given instantaneous pressure gradient than when the valve was opening from a closed state. This supports the observed peak in reverse flow when the pressure gradient was decreasing (Figure 3.6), as a larger gap distance initially allows more backflow until the valve is fully sealed. This non-linear behavior due to the delayed valve response has been observed experimentally [8], further emphasizing the importance of studying the valve's dynamic behavior.

Comparison of the dynamic response of valves of two different normalized stiffness values reveals a significant effect of valve stiffness on the hysteresis area and the gap size throughout the pumping cycle. Figure 3.7 shows a larger gap opening for flexible valves throughout the entire pumping cycle, except at the point when the valve is fully closed at maximum negative pressure ($\Delta P_{app}/\Delta P_{app,max} = -1$). When fully opened (i.e., $\Delta P_{app}/\Delta P_{app,max} = 1$), the flexible valve is able to open to a greater gap than the stiff valve. This is due to the decreased elastic forces balancing the pressure forces from the pressure gradient and results in lower resistance to forward flow than in stiff valves, as shown in Figure 3.4a.

On the other hand, the gap distance approaches zero when the valve is in the closed position (i.e., $\Delta P_{app}/\Delta P_{app,max} = -1$) for valves of both stiffness values, as seen in Figure 3.7. This is due to the fact that the limiting valve position when subjected to an adverse

pressure gradient is the fully-closed position with a zero gap distance. This is in agreement with the results in Figure 3.4b, which indicates that valve fluid conductance to back flow experiences little variation with stiffness, so long as the valve stiffness is not taken to values prohibiting proper closing.

Figure 3.7 also shows that while valves of both stiffness values experience a significant response delay resulting in a gap hysteresis between an increasing and decreasing pressure gradient, this hysteresis is more pronounced for a flexible valve than for its stiffer counterpart. This effect can be quantified through comparison of the opening-closing gap difference at zero pressure gradient. A flexible valve has a greater difference in gap distance at zero pressure gradient, as indicated in Figure 3.7. This is due in large part to the ability of flexible valves to open further than stiffer valves, resulting in a greater distance for them to travel during opening and closing. This larger distance to travel leads to greater valve velocities, hydrodynamic forces, and ultimately, to variation in hysteresis.

3.4.3 Optimization of pumping

An important quantitative measure of overall valve performance is the volume of fluid pumped through the valve. Figure 3.8 shows the volume, $Vol = \overline{Q_r(t)}\tau_r$, pumped through a valve orifice in one cycle of a trapezoidal pressure waveform. Note that $\overline{Q_r(t)}$ is the mean flow rate of the pumped fluid per cycle τ_r. This is normalized by the volume passed through the vessel without a valve under a constant forward pressure gradient (the maximum forward pressure gradient in the trapezoidal waveform) throughout a single cycle period, calculated based on the Poiseuille approximation and denoted Vol_{Pois}. Note that the ratio Vol/Vol_{Pois} is also equal to the normalized average flow rate pumped

through the valve per cycle since $Vol/Vol_{Pois} = \overline{Q_r(t)}\tau_r/Q_{r,pois}\tau_r = \overline{Q_r(t)}/Q_{r,pois}$. The normalized volume pumped is plotted against valve aspect ratios for $K_{b,r} = 0.25$ and $K_{b,r} = 0.7$.

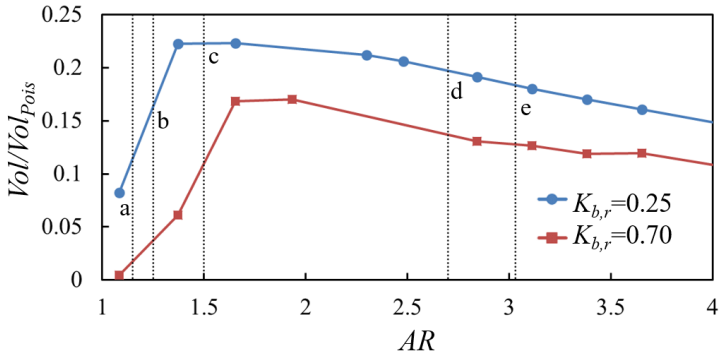

Figure 3.8 Normalized volume pumped during a single pumping cycle induced by a pressure gradient varied in a trapezoidal waveform through valves of varied aspect ratio with $K_{b,r} = 0.25$ and $K_{b,r} = 0.7$ with $K_{s,r} = 0.1$ for all cases. The markings a-e and dotted vertical lines correspond to the aspect ratios of the valves shown in Figure 3.2a-e, respectively.

For both stiffness values, the volume pumped rapidly increases with increasing aspect ratio from the limit of low AR until it reaches AR_{cr} in the range of approximately $1.3 \leq AR \leq 1.7$. Above AR_{cr}, a gradual decrease in pumping occurs with increasing aspect ratio. As shown in Figure 3.3, low aspect ratio valves have low resistance to forward flow, but also allow back flow, suggesting that little if any flow will be pumped in the forward direction. However, as backflow is reduced with increasing aspect ratio, an optimal aspect ratio can be reached where the most pumping is done per cycle for a given stiffness. Valves with aspect ratios which are higher than this optimal configuration will yield increased resistance to forward flow, leading to an overall decrease in pumping effectiveness with increased aspect ratios. Comparison of this result with aspect ratios of

physiological valves from Figure 3.2 again suggests that lymphatic valves are potentially optimized for maximum pumping capability.

3.5 Combining with lumped parameter models

Results from above sections reveal that valve morphology has a significant impact on valve's contribution to lymph flow. In comparison, many lumped parameter models widely utilizes a sigmoidal functional relationship of valve resistance with multiple adjustable model parameters [26, 30, 31]. However, there is no clear relationship between the model parameters and properties of the valve like its morphology and mechanical properties.

To compare the sigmoidal model with our flow resistance model, our own valve flow resistance model was created by running several steady-state simulations of varying applied pressure gradients, shown in Figure 3.9. Figure 3.9a shows that although sigmoidal model approximates valve flow resistance, the model fails to capture detailed features like a more gradual decrease in flow resistance under forward flow near the region of sudden resistance change (transition zone). Furthermore, a noticeable shift in resistance transition location occurs between different bending stiffness. Although similar sigmoidal fits are created under both bending stiffness in Figure 3.9a, parameters for each sigmoidal function have to be arbitrarily fitted for best shape as there is no clear relationship between different valve properties to the sigmoidal function parameters.

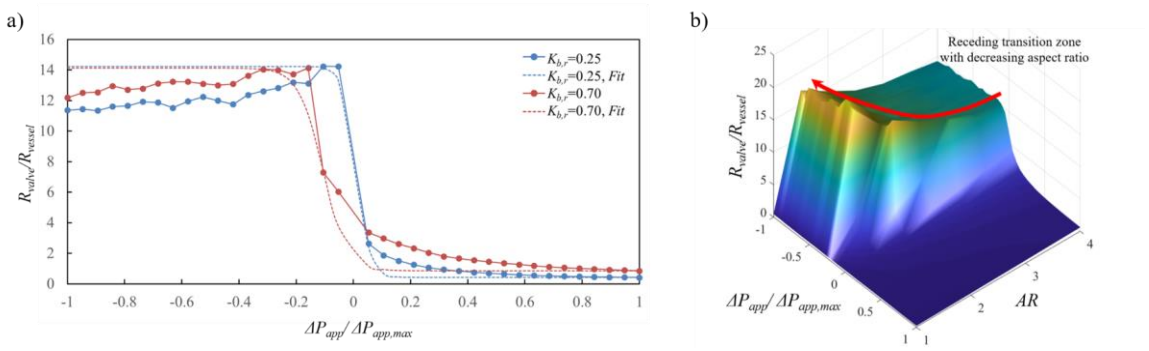

Figure 3.9 Flow resistance model of the lymphatic valve constructed from series of steady state-cases of varying parameters. Note that all axes are normalized based on the criteria mentioned in above sections. a) Comparison between flow resistance model our model with the sigmoidal model, noted in dashed lines, under two different bending stiffness. Other parameters for both $K_{b,r}$ are set as $AR = 2.7$ and $K_{s,r} = 0.28$. The sigmoidal model parameters were adjusted to resemble the simulated data as close as possible. b) 3D surface plot of valve flow resistance as a function of aspect ratio and applied pressure difference, represented as AR and $\Delta P_{app}/\Delta P_{app,max}$, respectively.

Figure 3.9b then combines simulated results of Figure 3.9a under different valve aspect ratios, creating a surface plot of valve aspect ratio, applied pressure gradient, and valve resistance. The plot indicates that shorter valves begin to fail in preventing backflow effectively, as seen in the receding transition zone with lower aspect ratio, where valves start to not occlude properly until a larger backward pressure gradient is applied. The finding again supports that shorter valves can only be effective in pumping when they can prevent backflow properly and demonstrates that a flow resistance can be defined as a function of different valve properties. The findings also show that tabulation of valve resistance under different valve properties can supply lower-dimensional models such as lumped parameter models with more physiologically relevant values, which can vary with coherent trend. For example, valve resistance can be an oscillating function of time since valve aspect ratio would change under different phases of vessel contraction, as the change in vessel diameter would change the valve aspect ratio.

CHAPTER 4. LYMPHATIC VALVE IN A CONTRACTING VESSEL

4.1 Introduction

Although the previous chapter explores various aspects of the lymphatic valve, the model in the previous chapter was necessarily restricted to a study of lymphatic valve in a rigid vessel where flow was motivated by applied pressure gradient. By expanding our finding to a case with vessel contraction, this chapter investigates the second objective of the research goal, where lymphatic vessel contraction was applied to motivate the flow against an adverse pressure gradient.

Specifically, we focus on understanding the pumping behavior of a peristaltically contracting vessel fitted with compliant valves similar to those found in lymphatic systems [93, 94]. We consider a periodic vessel that undergoes periodic radial contractions leading to a sinusoidal traveling wave [50, 51]. We use this model to investigate the effects of elastic valves on pumping performance of peristaltically contracting vessels. Specifically, valve and vessel properties such as vessel contraction wave speed, vessel contraction amplitude, and valve elasticity are systematically probed for the peristaltic pumping under a range of applied adverse pressure gradients.

Additional complexity in lymphatic systems emerges due the coupling between the contraction amplitude of lymphatic vessel and the applied adverse pressure gradient [14]. Experiments show that an increasing adverse pressure gradient results in a decreased contraction amplitude diminishing the pumping performance of lymphatic vessel. Such

behavior is typically associated with the finite force generation by the lymphatic muscle cells driving contractions. Other physiological features affecting lymphatic pumping include nonuniformity of vessel contraction near the valve [14, 95] and lymph flow-sensitive wall contraction via wall shear stress [96, 97]. Here, we examine how the coupling between the adverse pressure gradient and the vessel contraction amplitude affects the pumping performance of peristaltic vessels with elastic valves.

4.1.1 Peristaltic pumping

Without valves, peristaltic pumping generates fluid packets with alternating axial velocity that are steady in the moving frame of reference under constant contraction wave speed c (Figure 4.1a). These velocity packets lead to a net transport of the fluid in the direction of wave propagation that we refer as the positive flow direction. The presence of an adverse pressure gradient can reduce the net fluid pumping by peristaltic oscillations and ultimately can result in a negative flow (Figure 4.1b). When the adverse pressure gradient is large enough, sections with positive flow velocity diminish or entirely disappear, even though the general pattern with repeating velocity packets is still maintained (Figure 4.1c). The peristaltic pumping in a vessel without valves provides a baseline that allows us to evaluate the function of valves and to identify their effects on the fluid flow and pumping.

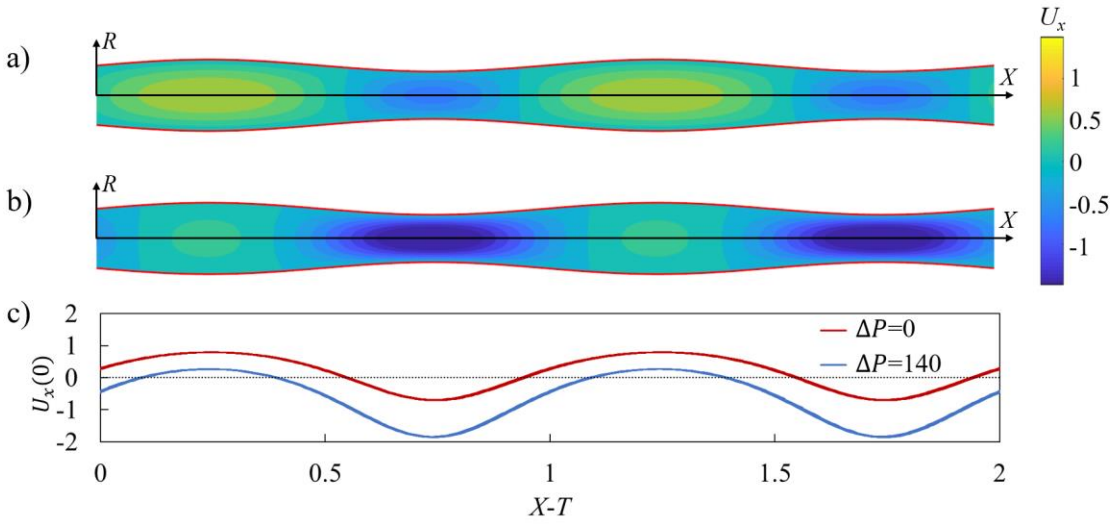

Figure 4.1 a) Axial component of flow velocity U_x in a valve-less peristaltic vessel without an imposed pressure gradient yielding a flow rate $Q = 0.15$. b) Axial velocity U_x in a vessel with an adverse pressure gradient $\Delta P = 140$ yielding a flow rate $Q = -0.22$. c) Centerline axial velocity $U_x(0)$ in the moving reference frame $X - T$. In these simulations, the contraction ratio is $\phi = 0.2$, and the peristaltic Reynolds number is $Re = 0.2$. Note that $X = x/\lambda, T = t/\tau, \Delta P = \Delta p_\lambda \, {r_0}^2 \rho/\mu^2 \; Q = q/\pi r_0^2 c, \phi = a/r_0$, and $Re = \rho c {r_0}^2/\mu\lambda$, where Δp_λ is the pressure difference across a contraction wavelength, q is the vessel flow rate, r_0 is the mean radius of the vessel, x is the axial coordinate, ρ and μ are the fluid density and dynamic viscosity, and t is time. Furthermore, λ, τ, c, and a are the wavelength, period, speed, and amplitude of vessel contraction.

4.1.2 Model geometry

Initial geometry of the model is composed of a periodic fluid-filled axisymmetric vessel and two sets of valves with each valve made up of two compliant leaflets (Figure 4.2), simulating an infinitely long repeating chain of valves. Each leaflet is created from an intersecting plane between an axisymmetric vessel and a plane that cuts through the vessel at an angle [49]. Thus, the elastic leaflets are initially flat. The leaflet edge that overlaps with the vessel wall is firmly attached to the wall and follows the wall motion. The free edge of the leaflet has a semicircular cutout mimicking the typical geometry observed for lymphatic valves [98]. The valve geometry combined with the axisymmetric vessel deem

it necessary to use of a three-dimensional computational model since lower dimensional or axisymmetric models are unable to capture the leaflet motion. The leaflet geometry is characterized by the aspect ratio that is defined as the ratio between axial length of the leaflet and mean diameter of the vessel. In this chapter, we keep the leaflet aspect ratio equal to 1.75 that is in the typical range of experimental values [49]. The simulation domain has 301 by 44 by 44 LBM nodes in *x*, *y*, and *z*-directions, respectively, while the vessel and valves are composed of 8272 LSM nodes. The initial distance between two neighboring LSM nodes is about twice the distance between neighboring LBM nodes.

The vessel undergoes a prescribed radial motion that leads to a sinusoidal traveling wave propagating along the vessel in the axial x direction. The periodic motion of the vessel wall is given by

$$r_{vess}(x,t) = r_0\left[1 + \phi\, sin\left(\frac{2\pi}{\lambda}(x - ct)\right)\right] \tag{31}$$

where r_0 is the mean radius of the vessel, ϕ is the normalized contraction amplitude, λ is the wavelength, and $c = \lambda/\tau$ is the wave speed with τ being the oscillation period. Note that $\phi = a/r_0$ where a is the vessel contraction amplitude. We set the wavelength equal to the distance between centroids of two consecutive valves. The wavelength is kept at a constant value equal to the distance between valves to induce synchronous valve deformation, providing a clearer understanding behind fundamental operation of valves in contracting vessel.

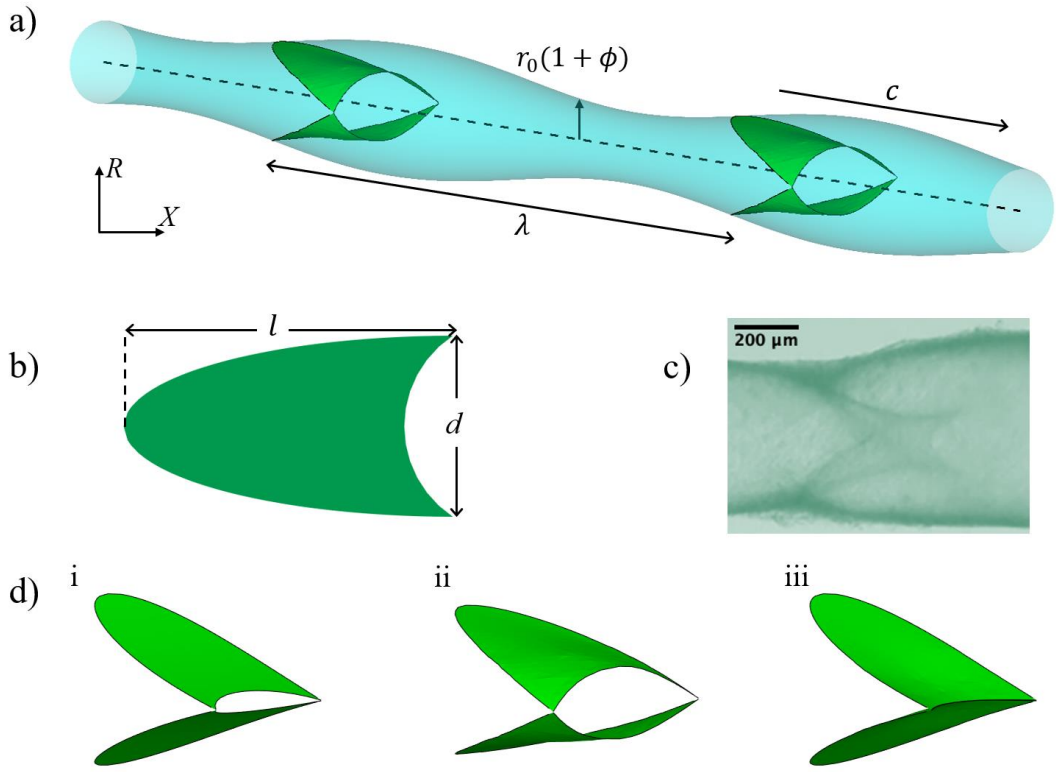

Figure 4.2 a) Model of a periodic contracting vessel fitted with two valves. b) Shape and dimensions of the valve leaflet. The edge on the right side of the leaflet is free, whereas the remaining part of the edge is attached to the vessel wall. The aspect ratio of the valve is defined as $l/d = 1.75$. c) Image of a lymphatic vessel segment with a valve. d) Typical valve profiles during different stages of valve operation. i: initial valve configuration, ii: valve opening, and iii: valve closure.

4.1.3 Survey of relevant experimental data

Experiments report a wide range of the contraction wavelength λ. Indeed, the wave speed c ranges from zero to 10mm/s with the frequency between 7 and 21 contractions per minute yielding the wavelength between 0 and 81mm [19, 95]. Since the vessel diameters typically range from $80\mu\text{m}$ to 2.8mm and considering that the larger vessels exhibit a longer wavelength, we estimate that the ratio of the wavelength to the vessel radius λ/r_0 is in a wide range between 0 and 60. In our simulations, we set $\lambda/r_0 = 15$,

which falls well in the experimental range. Furthermore, considering that inter-valve distance is the same as λ, this puts the valve placement within the experimental range where the values of this ratio are up to 20 [20, 99, 100].

We vary the following system parameters to investigate the vessel pumping performance: the traveling speed of vessel contraction wave c that is varied by varying the contraction period τ, the normalized contraction ratio ϕ, the adverse pressure difference over a contraction wavelength Δp_λ, and the in-plane stiffness and the bending stiffness of the valve. The ranges of these system parameters are selected based on the available experimental data summarized in Table 4.1.

Table 4.1 Lymphatic system parameters for simulating lymphatic valves with a contracting vessel

Parameters	**Experiments**	**Reference**
Valve length, l (μm)	80∼2800 (*est.*)	Pan, le Roux [20], Wilson, van Loon [21], Rahbar and Moore [34], Akl, Coté [95]
Average vessel diameter, d (μm)	80∼2800	MacDonald, Arkill [19], Pan, le Roux [20], Wilson, van Loon [21], Rahbar and Moore [34], Akl, Coté [95]
Valve thickness (μm)	0.5∼6	Lauweryns and Boussauw [89]
Applied adverse pressure difference, Δp_λ (Pa)	0∼2000	Davis, Rahbar [8], Davis, Scallan [14], Scallan, Wolpers [101]
Contraction wave speed, c (mm/s)	0∼10	Akl, Coté [95]
Contraction frequency, $1/\tau$ (contraction/min)	7∼21	Akl, Coté [95]
Dimensionless contraction amplitude, (ϕ)	0∼0.45	Davis, Scallan [14]
Viscosity, μ (mPa · s)	0.89∼1.36	MacDonald, Arkill [19], Moore and Bertram [23], Kassis, Yarlagadda [102]

Fluid density, ρ (kg/m^3)	998~1016	MacDonald, Arkill [19], Moore and Bertram [23], Burton-Opitz and Nemser [103]

Note that in lymphatic systems, the contraction amplitude depends on the adverse pressure difference Δp_λ [14]. Here, we first examine the flow where the two parameters are independent to isolate the effect of each parameter on the flow. Then, the two parameters are coupled via the experimentally reported relationship and investigated to reveal any difference arising from the coupling.

4.1.4 Nondimensional number and simulation parameters

The above mentioned physical parameters can be expressed in terms of the following dimensionless parameters relevant to peristaltic pumping [50, 51], which are indicated using the uppercase. We use the dimensionless axial coordinate $X = x/\lambda$, radial coordinate $R = r/r_0$, axial component of flow velocity $U_x = u_x/c$, and time $T = t/\tau$. The adverse pressure difference is nondimensionalized as $\Delta P = \Delta p_\lambda \, {r_0}^2 \rho/\mu^2$, which represents the ratio between pressure and viscous forces during peristaltic pumping [50, 104-108]. The Reynolds number for peristaltic pumping is defined as $Re = \rho c {r_0}^2/\mu\lambda$, where ρ is the fluid density, and μ is the dynamic viscosity [50, 51, 109-111]. Because parameters that describe Re are kept constant throughout the work except for c, a change in peristaltic Reynolds number means a corresponding change in contraction wave speed defined by τ. We vary Re in the range between 0.1 and 1.4. The dimensionless valve leaflet in-plane and bending stiffnesses are $K_s = k_s \rho r_0/\mu^2$ and $K_b = k_b \rho/\mu^2 r_0$, respectively. These parameters represent the ratios between, respectively, stretching and bending forces experienced by the valve and the viscous forces applied on the vessel wall.

The pumping performance is quantified in terms of the flow rate q averaged over a wave period τ, the average work done by the vessel wall w_{avg}, pumping efficiency η and pumping economy ε that are both evaluated over a wavelength λ and averaged over a wave period τ. To calculate w_{avg} the work done by vessel walls is calculated by integrating the hydrodynamic force on the wall over the wall displacement and averaging the work over the wavelength λ and period τ of the vessel. The pumping efficiency is defined as $\eta = q\Delta p_{\lambda}\tau/w_{avg}$ while the pumping economy is defined as $\varepsilon = q(\Delta p_{\lambda} + \Delta p_{visc})\tau/w_{avg}$, where Δp_{visc} is pressure loss due to viscous friction for laminar flow arising at flow rate q in a straight pipe with radius r_0 and length λ. This is expressed as $\Delta p_{visc} = q/(\pi {r_0}^4/8\mu\lambda)$. Thus, the pumping efficiency represents the relative amount of work done by the vessel that goes into the transporting the fluid against the adverse pressure gradient, whereas the flow economy indicates the proportion of the work that is consumed by the fluid transport and viscous losses. The flow rate is normalized as $Q = q/q_0$, where $q_0 = \pi r_0^2 c$ is the flow rate in a rigid pipe with radius r_0 and average flow velocity c. Note that this normalization that has been previously used for peristaltic pumping [50, 51]. Work done by the vessel wall per wave period is normalized by the corresponding friction loss generated in a rigid pipe with an average flow velocity c using Hagen-Poiseuille law [112] and is given by $W = w_{avg}/(8\mu\lambda\pi c^2\tau)$.

To characterize valve opening, we evaluate the cross-sectional area defined by the free edges of the leaflets a_{valve} that is normalized as $A = a_{valve}/\pi {r_0}^2$. The maximum valve opening A_{max} is defined as the maximum value of A over a vessel cycle. Furthermore, we examine the time that the valve is closed per vessel cycle $T_c = \tau_c/\tau$. Here,

τ_c is the time that valve remains closed during one vessel period. The valve is considered closed when $A < 0.05$. The dimensionless parameters are summarized in Table 4.2.

Finally, the Cauchy number from Table 3.1 is recalculated based on simulation parameters under contracting vessel, using $Ca_c = (\rho d^3 c^2)/d_b$. For the contracting vessel, the mean diameter of the vessel is used for d while the characteristic velocity U_c is set at c. Based on typical operating conditions, the recalculated Cauchy number gives $Ca_c = 2.8$, which is about an order of magnitude higher than its counterpart under a rigid vessel.

Table 4.2 Definitions of the dimensionless parameters for simulating lymphatic valves with a contracting vessel

Dimensionless parameter	**Expression**
Input parameters	
Peristaltic Reynolds number	$Re = \rho c {r_0}^2/\mu\lambda$
Contraction amplitude	$\phi = a/r_0$
Pressure difference	$\Delta P = \Delta p_\lambda \, {r_0}^2 \rho/\mu^2$
Bending stiffness	$K_b = k_b \rho/\mu^2 r_0$
In-plane stiffness	$K_s = k_s \rho r_0/\mu^2$
Output parameters	
Flow rate	$Q = q/q_0 = q/(\pi r_0^2 c)$
Work done by the vessel	$W = w_{avg}/(8\mu\lambda\pi c^2 \tau)$
Pumping efficiency	$\eta = q\Delta p_\lambda \tau / w_{avg}$
Pumping economy	$\varepsilon = q(\Delta p_\lambda + \Delta p_{visc})\tau / w_{avg}$
Valve opening cross section	$A = a_{valve}/\pi {r_0}^2$
Valve closure time	$T_c = \tau_c/\tau$
Descriptive parameters	
Axial coordinate	$X = x/\lambda$
Radial coordinate	$R = r/r_0$

Axial flow velocity	$U_x = u_x/c$
Time	$T = t/\tau$

4.1.5 Numerical validation

The simulations start with a stagnant fluid and continue for at least 5 contraction periods to eliminate the influence of the initial transient. This ensures that the difference in the results between consecutive periods does not exceed 1%.

We have previously extensively validated our FSI model with application to different flows including lymphatic pumping [49, 72, 75, 77, 113]. Here, we perform two additional tests to examine the accuracy of the model for simulating flow generated due to moving vessel walls. The first test (Figure 4.3) compares the axial velocity profiles in vessels with radially moving walls with the analytical solutions for semi-infinite circular pipe flow with the same wall motion [114]. The normalized radial velocity is defined as $\alpha = \rho v_r(t) r(t)/\mu$, where $v_r(t)$ is the radial speed and $r(t)$ is the radial position. Three different normalized radial speeds were tested for expanding and contracting vessels. Normalized axial velocity profiles in Figure 4.3 indicate that the numerically calculated flow velocities are in close agreement with the analytical results for both expanding and contracting vessels.

The second test compared Q and W obtained using an analytical solution for peristaltic oscillation [50, 51] with simulated results, as shown in Figure 4.4. The comparison is made for $\phi = 0.2$ and 0.25, $\Delta P = 0$ and 140, and for a range of Re. It was found that the simulations are close to the analytical solution under different system

parameters relevant to our study. Divergence from the analytical solution growths as Re increases. This can be expected since the analytical solution assumes $Re \ll 1$.

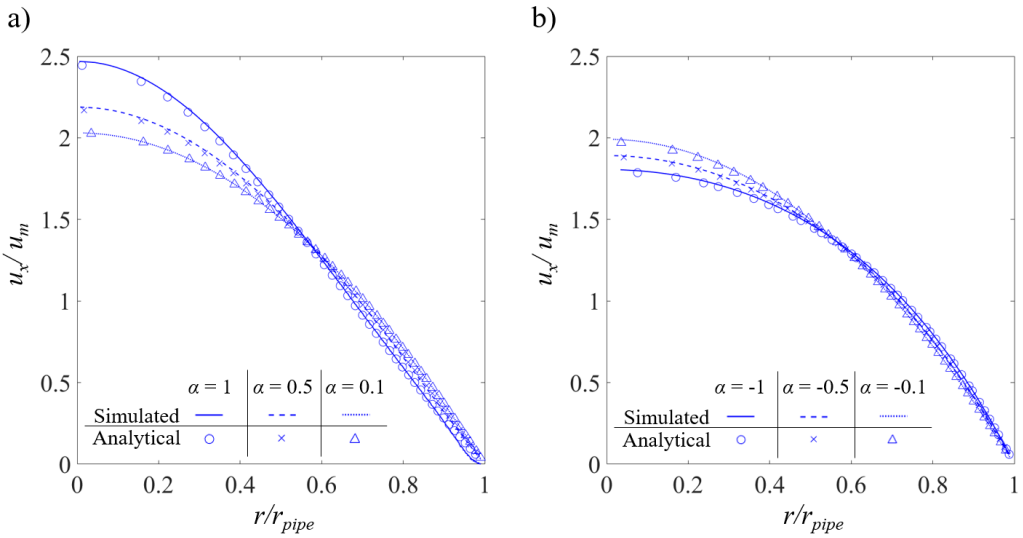

Figure 4.3 Axial flow velocity u_x in a) expanding and b) contracting vessels for different values of radial wall velocity α. Axial velocity is normalized by the mean axial velocity of the vessel u_m, whereas the radial coordinate r is normalized by the vessel radius r_{pipe}. The lines represent the simulated results, whereas the symbols represent the analytical solution [114].

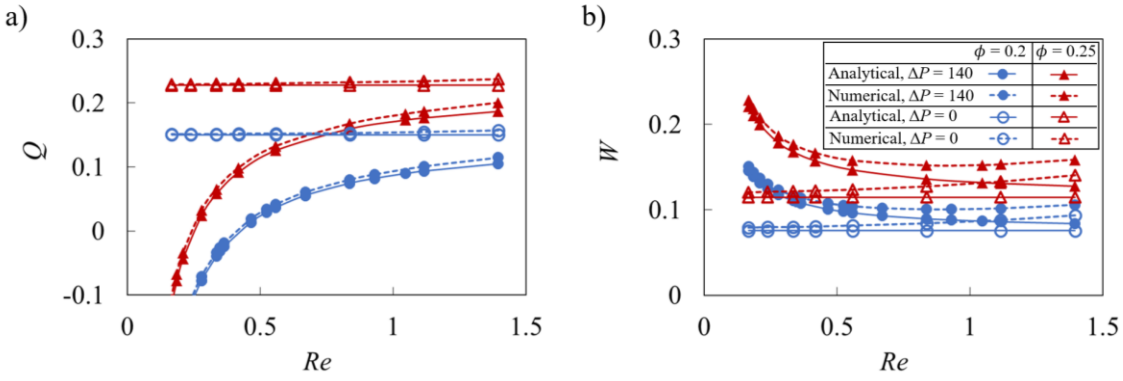

Figure 4.4 a) Flow rate Q and b) vessel work W as a function of peristaltic Reynolds number Re for different contraction amplitude ϕ without valves. The solid and dotted lines show the analytical and numerical solutions, respectively. The empty and filled symbols represent data for $\Delta P = 0$ and $\Delta P = 140$, respectively.

4.2 General flow pattern and valve deformation

Figure 4.5a and Figure 4.5b present snapshots showing axial velocity magnitude and valve deformation for different stages of the vessel contraction cycle, respectively, without and with adverse pressure gradient. Note that figures show one valve since the flow profile and valve deformation repeat due to their synchronous motion. Similar to peristaltic pumping without valves (Figure 4.1), the flow is divided into alternating packets of positive and negative axial velocities. Regions of the positive axial velocity travel in the expanded region of the vessel, while packets of negative axial velocity propagate within the contracted region of the vessel. This indicates that velocity packets propagate with the same speed as the contraction wave [50, 51].

Unlike vessels without valves, velocity packets are disrupted when they pass through the elastic valves. Compared to an axisymmetric flow profile in the cases without valves, flow disruption by the valves results in a flow that is no longer axisymmetric even though the pattern of alternating positive and negative velocity packets still persists. The valves open when they encounter packets of positive axial velocity and close to occlude the flow when packets of negative axial velocity pass. Thus, the valves affect the forward and backward flow in different ways. While the forward flow is allowed with some viscous loss due to the reduced orifice size, the backflow can be significantly suppressed and ultimately stopped by fully closed valves.

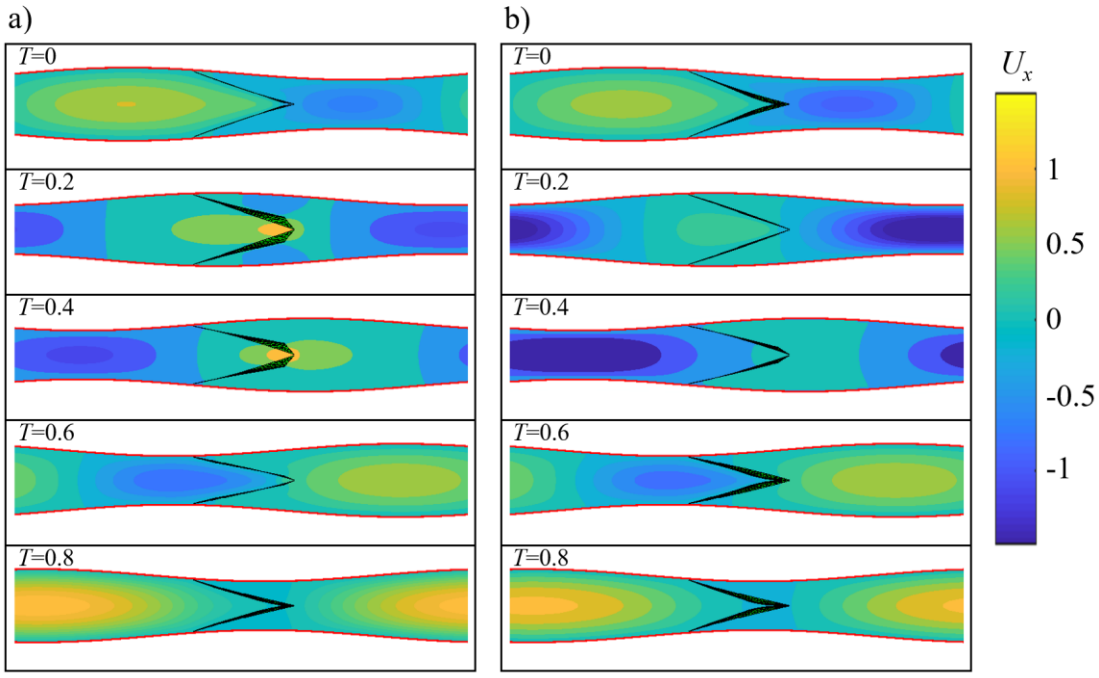

Figure 4.5 a) Axial flow velocity U_x at different instances of the contraction cycle in a valved vessel with no adverse pressure gradient. b) Axial flow velocity U_x in a valved vessel with $\Delta P = 140$. Note that due to the valves, flow profile is not axisymmetric. Flow profiles are shown at the symmetry plane perpendicular to the valve opening. The simulation parameters are $\phi = 0.2$, $Re = 0.2$, $K_b = 88$, and $K_s = 115$.

The valves deform differently when encountering fluid packets with positive and negative velocities, as shown in Figure 4.2d. When encountering packets of positive axial velocity, the leaflets stretch and deform outwards by a combined action of the flow and the vessel expansion. This process increases the opening area of the valve defined by the leaflet free edges, thereby enabling fluid flow. When the valve encounters negative velocity packets, the vessel contracts. The middle of the leaflets deforms inwards, allowing the free edges to rapidly collapse and block the flow. The valve closure process culminates by creating a coaptation zone expanding from the leaflet free edges.

The effect of valves on backflow reduction is more evident when the flow is subjected to an adverse pressure gradient. In this scenario, a peristaltic vessel without a valve has a limited capacity to transport fluid in the direction of wave propagation (Figure 4.1b), whereas addition of unidirectional valves yields a positive net flow in the vessel (Figure 4.5b). Note that without adverse pressure gradient, both vessels with and without valves can successfully pump fluid in the positive direction (Figure 4.1a and Figure 4.5a). This further points to the important role that valves play in enabling pumping against adverse pressure gradients.

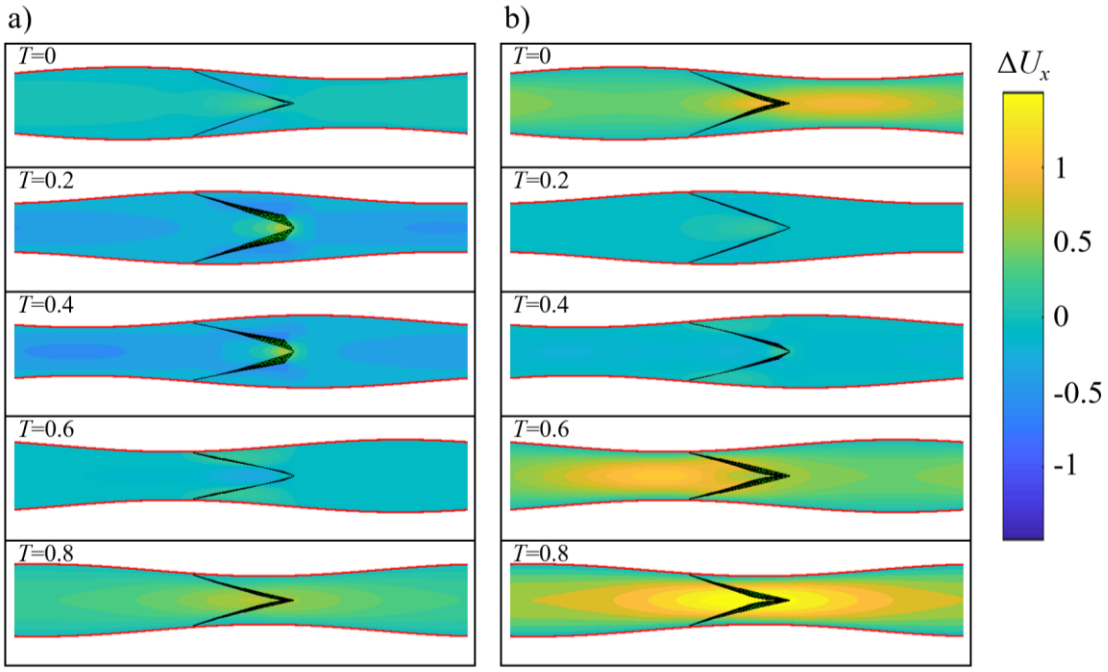

Figure 4.6 a) Axial flow velocity difference ΔU_x at different instances of the contraction cycle in a valved vessel with no adverse pressure gradient. b) Axial flow velocity difference ΔU_x in a valved vessel with $\Delta P = 140$. Flow profiles are shown at the symmetry plane perpendicular to the valve opening. The simulation parameters are $\phi = 0.2$, $Re = 0.2$, $K_b = 88$, and $K_s = 115$. The flow velocity difference ΔU_x is calculated as the difference between flow velocities in vessels with and without valves.

The effect of valves on pumping is further revealed when considering the difference in axial velocity between vessels with and without valves denoted as ΔU_x and shown in Figure 4.6. When packets of positive velocity pass through an open valve (see Figure 4.6 for $T = 0.2$ and 0.4), the overall flow velocity pattern is similar to the flow in the valve-less vessel with minor flow disturbances around the valves, where the flow accelerates due to the reduced opening between the leaflets. In this case, ΔU_x is nearly zero everywhere in the vessel except for a small region in the vicinity of the valve. The velocity difference ΔU_x is more significant when vessel contraction passes the valve. In this case, negative flow velocity causes the valve to close and block the flow. This, in turn, results in a positive ΔU_x in most of the vessel, as shown in Figure 4.6 for $T = 0$, 0.6, and 0.8. A significant positive difference in velocity between the cases with and without valves when the valves are closed indicates that the valves increase pumping by reducing backflow. Furthermore, when comparing Figure 4.6a and Figure 4.6b, we find that the backflow reduction is more prominent when the pumping is against an adverse pressure gradient. Indeed, the adverse pressure gradient causes a significant negative flow when the valve-less vessel contracts (Figure 4.1b). The backflow is stopped by the closed valves in the case of the vessel fitted with valves (Figure 4.5b).

4.3 Contraction wave speed on pumping

4.3.1 General centerline axial velocity profile

We first examine the effect of contraction wave speed on pumping by varying the peristaltic Reynolds number that, in turn, is realized by varying the contraction period τ. In Figure 4.7, we show how the centerline flow velocity $U_x(0)$ changes along the vessel

without an adverse pressure gradient at $Re = 0.2$ and $Re = 0.6$. The velocity is shown as a function of the distance along the vessel X and in the moving reference frame $X - T$. In Figure 4.7a and Figure 4.7c, which show the velocity $U_x(0)$ as a function of the distance along the vessel X, the two vertical dotted lines indicate the location of the valve with the leaflet free edge being on the right side. Furthermore, the horizontal lines in these figures show the maximum and minimum magnitude of the centerline velocity in a vessel without a valve. Figure 4.7b and Figure 4.7d show the velocity $U_x(0)$ in the moving reference frame $X - T$ in which case the velocity in a valve-less vessel is represented by a single line. Note that the velocities in Figure 4.7a and Figure 4.7b correspond to the snapshots shown in Figure 4.5.

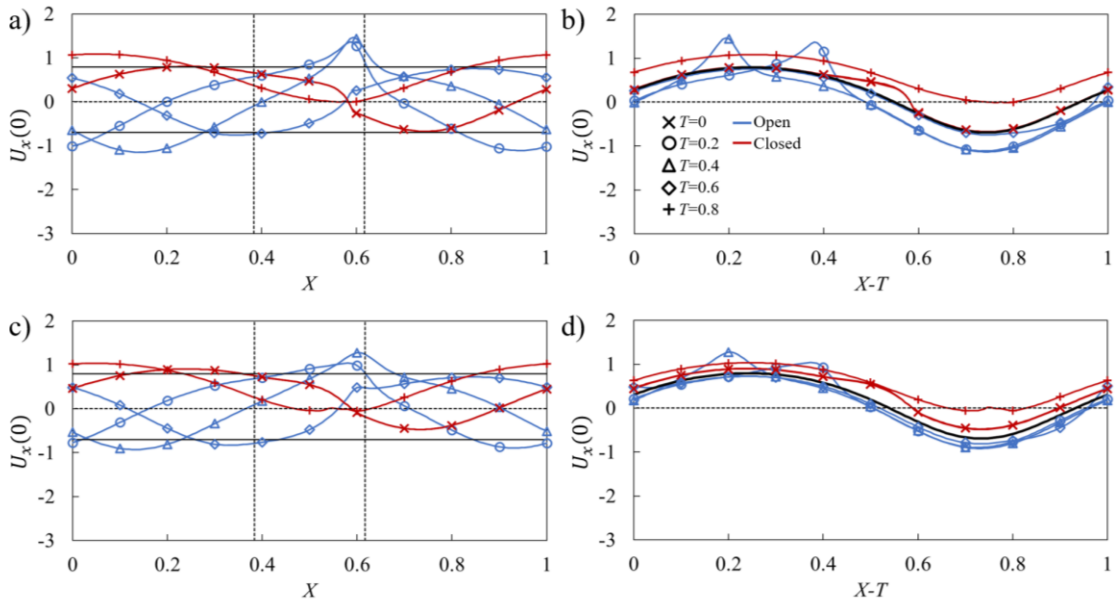

Figure 4.7 a) Centerline axial flow velocity $U_x(0)$ in the stationary reference frame in a vessel with no adverse pressure gradient with $Re = 0.2$. The maximum valve opening is $A_{max} = 0.44$. b) Same as a) but in the moving reference frame, the solid black line indicates the average centerline velocity for the valve-less vessel. c) Centerline axial flow velocity $U_x(0)$ in a stationary reference frame in a vessel with $Re = 0.6$. The maximum opening is $A_{max} = 0.68$. d) Same as c) but in the moving reference frame, the solid black line indicates the average centerline velocity for the valve-less vessel. The horizontal solid

lines indicate the maximum and minimum centerline velocities in a vessel without valves. The dashed vertical lines indicate the boundaries of valve position. The blue and red lines show the velocities when the valves are, respectively, open ($A \geq 0.05$) and closed ($A < 0.05$). The simulation parameters are $\Delta P = 0$, $\phi = 0.2$, $K_b = 88$, and $K_s = 115$.

Outside from the regions around the valve, the centerline velocity follows a sinusoidal wave (Figure 4.7a), which is characteristic for the centerline velocity in peristaltic vessels without valves (Figure 4.1c). The valves introduce a velocity disturbance that is manifested by a velocity maximum at the valve orifice located at $X = 0.6$ and is formed by the partially open leaflets at $T = 0.2$ and 0.4 (Figure 4.7a). Furthermore, when the valve is closed at $T = 0$, 0.6, and 0.8, the centerline velocity between coapted leaflets is nearly zero. Thus, the valve prevents a negative flow at the valve orifice.

To identify the velocity changes induced by the valves with respect to the centerline velocity in the valve-less vessel, we use a moving reference frame that is translated with the speed of the traveling wave (Figure 4.7b). We find that the valve can both decrease and increase the centerline velocity with respect to the valve-less vessel. The velocity corresponding to the open valve condition is somewhat lower than the valve-less velocity. Thus, the flow resistance in the valves on average reduces the flow in the entire vessel. On the other hand, when the valve is closed, the centerline velocity in the vessel exceeds the valve-less velocity. For a fully closed valve, the velocity within the vessel is defined by the fluid redistribution induced by the peristaltic wave propagating along the vessel.

The overall pumping in the vessel with valves is greater than in a valve-less vessel when the backflow reduction due to valve closure outweighs the velocity decrease due to the hydrodynamic resistance in the open valve. Thus, the pumping performance is

determined by the valve properties and is maximized when the valve is able to fully block the backflow with minimal resistance for the forward flow.

4.3.2 Centerline velocity profile under different contraction wave speed

Increasing the Reynolds number from $Re = 0.2$ to $Re = 0.6$ does not change the general shape of the centerline velocity profile, although the maxima at the valve orifice are less pronounced (Figure 4.7c). During the backflow phase the valve is able to fully close as indicated by the near zero velocity at $T = 0$ and 0.8 at the leaflet edge. Compared to the case of $Re = 0.2$, the increase in wave speed decreases the deviation of centerline velocity from that of a valve-less vessel. We also find that the velocity during the open valve phase matches closer to the valve-less velocity with increased Reynolds number, which can be attributed to a reduced hydrodynamic resistance of the valve from a greater opening due to the faster fluid flow. Indeed, at $Re = 0.2$ the maximum opening of the valve is about 44% of the cross-sectional area under the average vessel diameter, whereas the maximum opening increases to 68% when $Re = 0.6$.

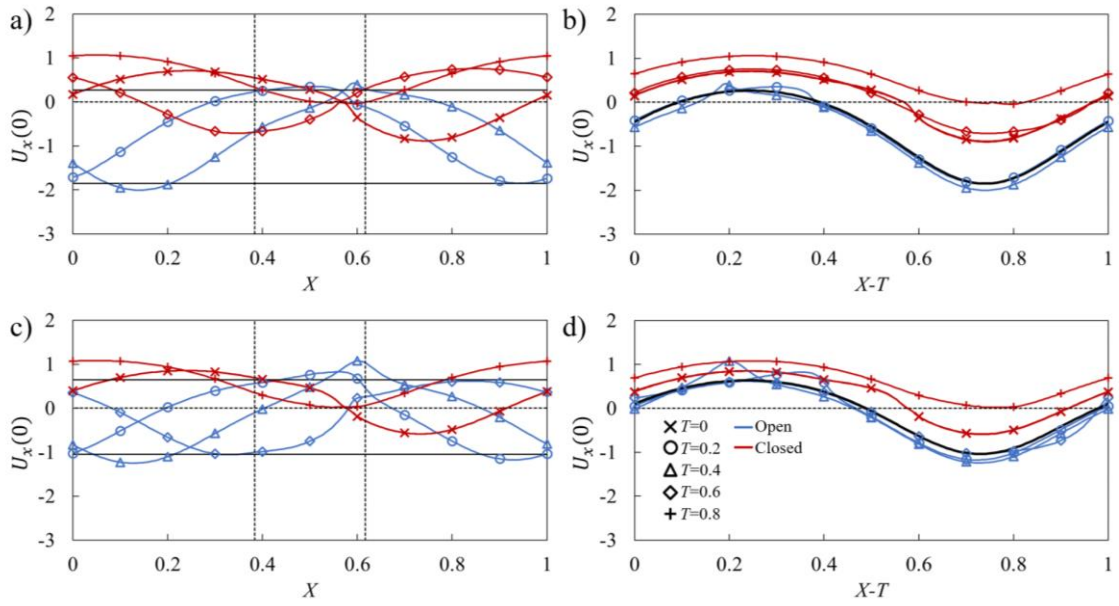

Figure 4.8 a) Centerline axial flow velocity $U_x(0)$ in the stationary reference frame in a vessel with $Re = 0.2$ with an adverse pressure gradient. The maximum valve opening is $A_{max} = 0.3$. b) Same as a) but in the moving reference frame, the solid black line indicates the average centerline velocity for the valve-less vessel. c) Centerline axial flow velocity $U_x(0)$ in a stationary reference frame in a vessel with $Re = 0.6$. The maximum opening is $A_{max} = 0.61$. d) Same as c) but in the moving reference frame, the solid black line indicates the average centerline velocity for the valve-less vessel. The horizontal solid lines indicate the maximum and minimum centerline velocities in vessels without valves. The dashed vertical lines indicate the boundaries of valve position. The blue and red lines show the velocities when the valves are, respectively, open ($A \geq 0.05$) and closed ($A < 0.05$). The simulation parameters are $\Delta P = 140$, $\phi = 0.2$, $K_b = 88$, and $K_s = 115$.

Figure 4.8 shows centerline velocities for the flow in vessels with $Re = 0.2$ and $Re = 0.6$ that experience an adverse pressure difference $\Delta P = 140$. The velocities in Figure 4.8a and Figure 4.8b correspond to the snapshots in Figure 4.5b. An adverse pressure gradient has a minor effect on the shape of the velocity profiles compared to the case of the flow with $\Delta P = 0$ (Figure 4.7) although the velocities are shifted towards the negative values. For $Re = 0.2$, the valve-less vessel is unable to produce a net positive flow resulting in $Q = -0.22$. For the same Re, the vessel with the valves yields a small positive $Q = 0.01$, indicating that a sufficiently high ΔP can stop pumping by such vessels.

Note that further increase of ΔP leads to the valve remaining fully closed throughout the entire contraction cycle. When compared to the velocity in the valve-less vessel, the velocities at the open valve condition are nearly identical to the valve-less velocity (Figure 4.8b). This can be attributed to a reduced flow through the valve at this ΔP as shown in Figure 4.8a.

At a larger $Re = 0.6$ (Figure 4.8c) both vessels with and without valves are able to generate a net positive fluid flow in spite of an adverse pressure gradient. However, valves enable significantly greater pumping of $Q = 0.11$ compared to $Q = 0.04$ without valves. This is again due to the ability of valves to stop backflow. The velocity during the open valve phase is slightly lower than the valve-less velocity (Figure 4.8d) and comparable to the velocity in the flow without adverse pressure gradient (Figure 4.8d). Indeed, in both cases normalized maximum valve openings are comparable with 61% and 68%, for $\Delta P = 140$ and $\Delta P = 0$, respectively. Thus, this adverse pressure gradient has a rather insignificant effect on the maximum valve opening.

Note that increasing Re has opposing effects on the peristaltic pumping with valves. On one hand, increasing Re facilitates valve opening and decreases the associated viscous loss; on the other hand, the time during which the valve is closed decreases impairing the valve's ability to fully arrest the backflow. Indeed, at $Re = 0.2$ the valve is closed about 62% of the contraction cycle, whereas at $Re = 0.6$ the valve is closed about 42% of the contraction cycle.

4.3.3 Pumping parameter variation

The dependencies of the pumping parameters on Re are summarized in Figure 4.9. The data is shown for $\Delta P = 0$ using the empty symbols, and for $\Delta P = 140$ using the filled symbols. Figure 4.9a shows that normalized flow rate Q mostly increases as Re increases. Without an adverse pressure gradient, Q remains nearly flat in valve-less vessels and slightly increases when vessels are fitted with valves. Thus, the flow rate has nearly a linear relationship with the wave speed. When the pumping occurs against an adverse pressure gradient, Q rapidly decreases with decreasing Re. Without valves, low Re results in a negative Q, meaning that peristaltic pumping cannot overcome the adverse pressure gradient at these wave speeds. With valves, however, low Re leads to slightly positive values of Q, indicating that whereas peristatic motion cannot pump the fluid, the valves are able to eliminate the backflow.

Figure 4.9b shows the normalized work W done over a wave period by the peristaltic vessel. In valve-less cases and in valved cases with $\Delta P = 0$, W is nearly constant indicating that work done by the vessel increases nearly quadratically with Re since the normalization factor is proportional to Re^2. Otherwise, the work W decreases with increasing Re, as increased flow rate leads to a larger valve opening and decreased loss from valve interference with the flow.

Pumping efficiency $\eta = q\Delta p_\lambda / w_{avg}$ is shown in Figure 4.9c as a function of Re. The efficiency is defined as the ratio between the work due to the fluid transport against the adverse pressure gradient and the work done by the vessel. Note that when $\Delta P = 0$ the efficiency is zero. We therefore present data only for $\Delta P = 140$. We find that the efficiency

curves for vessels with and without valves exhibit maxima indicating the existence of optimum Re maximizing the pumping per unit work against an adverse pressure gradient. This result is consistent with the analytical solution for peristaltic pumping [50, 51]. The maxima of efficiency are a result of two opposing trends. At small Re, peristaltic pumping cannot overcome the adverse pressure gradient diminishing the flow rate and therefore the pumping efficiency. For higher Re, the flow rate increases as Re, whereas the work increases as Re^2, leading to overall efficiency decrease with Re. Interestingly, valves increase the maximum efficiency and shift it to the lower values of Re. This can be related to a more rapid decrease of the flow rate with decreasing Re in valve-less vessels due to the adverse pressure gradient compared to vessels fitted with valves. Furthermore, the efficiency is greater for larger ϕ as a result of a faster flow (Figure 4.9a). For larger Re, the efficiency of valve-less and valved vessels nearly overlaps, indicating a weak effect of valves on pumping in this flow regime.

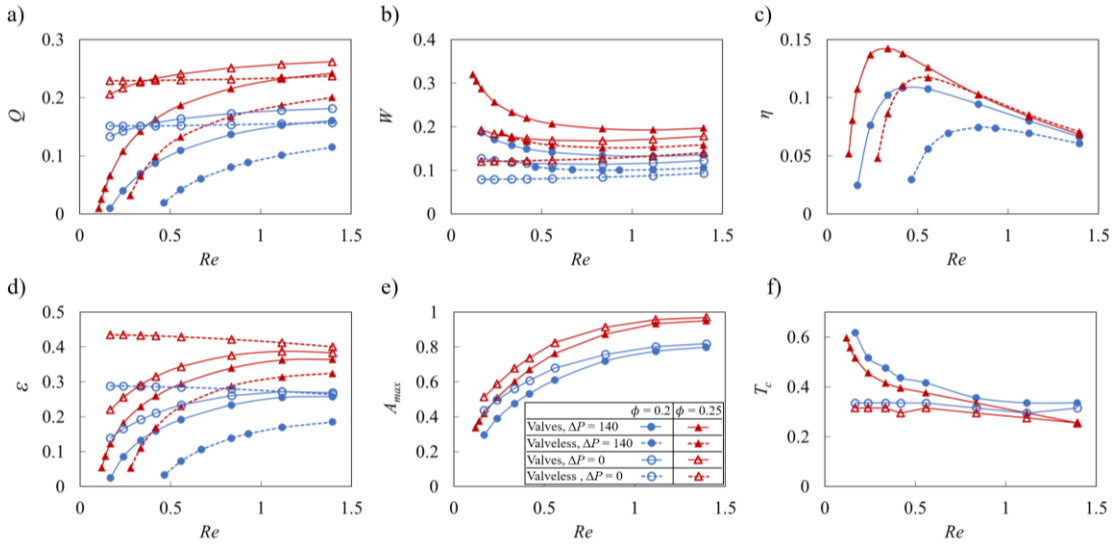

Figure 4.9 a) Flow rate, b) vessel work, c) pumping efficiency, d) pumping economy, e) maximum valve opening area A_{max}, and f) valve closure time T_c as a function of peristaltic Reynolds number for vessels with $K_b = 88$, and $K_s = 115$. The empty and filled symbols

represent data $\Delta P = 0$ and $\Delta P = 140$, respectively. The dashed lines represent results from valve-less vessels. The valve is considered closed when $A < 0.05$.

Another metric to characterize the performance of the peristaltic pumping is flow economy ε shown in Figure 4.9d as a function of Re. In addition to accounting for the work against the adverse pressure gradient, as it is in the case for η, ε also accounts for the viscous losses in the vessel. We find that ε is significantly greater than η and closely resembles the trend of the normalized flow rate shown in Figure 4.9a, indicating that greater amount of work by the vessel goes to viscous loss than to pumping the fluid. Without an adverse pressure gradient, ε for the valve-less vessel exceeds the value for vessels with valves, due to the additional loss associated with valves restricting the flow. The difference decreases with increasing Re due to the larger valve opening (Figure 4.9e). However, when $\Delta P = 140$, ε for vessels with valves exceeds valve-less ε. Thus, adding valves improve the economy when the flow is confronted by an adverse pressure gradient, whereas without an adverse pressure, pumping of the valve-less vessel is more economical.

We further characterize valve behavior during peristaltic pumping by quantifying the maximum valve opening area A_{max} and the occlusion time T_c, which are shown as a function of Re in respective Figure 4.9e and Figure 4.9f. The maximum opening area steadily increases with Re and plateaus for $Re > 1$. For lower Re, an adverse pressure gradient somewhat decreases A_{max} as a result of a lower positive flow velocity in the vessel (Figure 4.8). The occlusion time T_c is relatively constant with Re when the flow is not affected by ΔP. This is consistent with the velocity profiles shown in Figure 4.7 that exhibit minor variations for different Re. On the other hand, an adverse pressure gradient

causes T_c to increase with decreasing Re, as longer occlusion period occurs due to the increased backflow.

4.4 Adverse pressure gradient on pumping

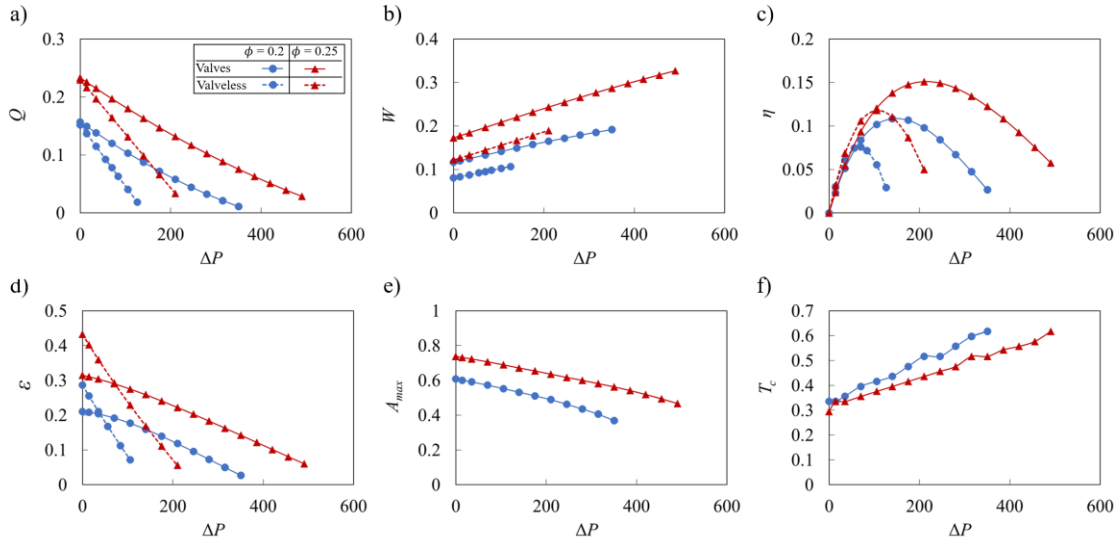

Figure 4.10 a) Flow rate, b) vessel work, c) pumping efficiency, d) pumping economy, e) maximum valve opening area A_{max}, and f) valve closure time T_c as a function of adverse pressure difference ΔP for vessels with $Re = 0.4$, $K_b = 88$, and $K_s = 115$. The dashed lines represent results from valve-less cases. The valve is considered closed when $A < 0.05$.

Figure 4.10 presents the dependence of peristaltic pumping parameters for vessels with and without valves on the magnitude of the adverse pressure difference ΔP. Here, we keep the wave speed constant leading to $Re = 0.4$. We find that the normalized flow rate Q decreases linearly with increasing ΔP (Figure 4.10a). Furthermore, Q increases with wave amplitude ϕ. For vessels without valves the decrease of Q is more rapid than for vessels with valves. As a result, valved vessels are able to pump fluid against significantly greater ΔP. However, this enhanced pumping in valved vessels comes at the cost of increased work W performed by the vessel (Figure 4.10b). The work by vessels with valves

exceeds the work by valve-less vessels likely due to the increased viscous losses associated with the flow through the occluding valves. Increased wave amplitude ϕ results in greater W.

Pumping efficiency is presented in Figure 4.10c. In spite the greater work done by vessels with valves, their efficiency is either comparable (at lower ΔP) or exceeds (at higher ΔP) that of valve-less vessels. Thus, in terms of pumping efficiency, the greater pumping capacity overcomes the increased viscous loss created by the valves. Furthermore, pumping efficiency curves exhibit maxima indicating the existence of optimum values of the adverse pressure gradient leading to the most efficient peristaltic pumping. For a vessel with valves, the optimum ΔP significantly exceeds that for a valve-less vessel. Furthermore, increasing ϕ increases the efficiency and the optimum ΔP. Thus, by changing vessel parameters the pumping can be optimized to a specific value of ΔP.

Flow economy shows nearly linear decrease with ΔP (Figure 4.10d). At lower ΔP, the work of vessel contraction mostly goes to overcome viscous friction loss rather than useful pumping. At these conditions, ε for valve-less vessels exceeds ε for vessels with valves. At higher ΔP, vessels with valves exhibit better economy than valve-less vessels. Note that the economy is greater when the wave amplitude is increased.

The maximum valve opening area and valve occlusion time are shown in Figure 4.10e and Figure 4.10f, respectively. Increasing adverse pressure gradient gradually decreases the valve maximum opening and increases the time that valve stays closed per contraction cycle. That is consistent with the reduction of the pumping flow rate with increasing ΔP (Figure 4.10a). Indeed, the slower flow velocity and lower favorable

pressure gradient in the vessel decrease the forces acting to open the elastic valve resulting in lower A_{max} and longer T_c.

4.5 Valve elastic properties on pumping

4.5.1 Valve deformation profile under different elastic properties

Figure 4.11 shows the side views of the valves with three representative bending stiffnesses, which we further refer as soft, normal, and stiff valves. The valves are plotted at different instances of vessel operation. Figure 4.11a indicates that soft valves experience valve depression at the middle of the valve under backflow. This deformation does not prevent backflow until the valve free ends fully close. Normal and stiff valves in Figure 4.11b and Figure 4.11c experience closures at the valve free ends, leading to a more effective backflow prevention than the soft valve. However, stiff valves are less responsive to changing flow rate, lengthening the time required for the valve to be fully open and closed, decreasing the maximum valve opening area during the forward flow and increasing the time the valve remains closed after the flow reversal. Finally, it is also worth noting the increased complexity in valve response as a function of bending stiffness compared to the stiffness analysis under a rigid vessel, especially against backflow. Valve response against backflow in Figure 3.4 shows monotonically increasing backflow reduction with decreasing valve bending stiffness, but this is not necessarily the case when vessel contraction is incorporated, even though both cases show faster deformation response by more flexible valves under changing flow conditions.

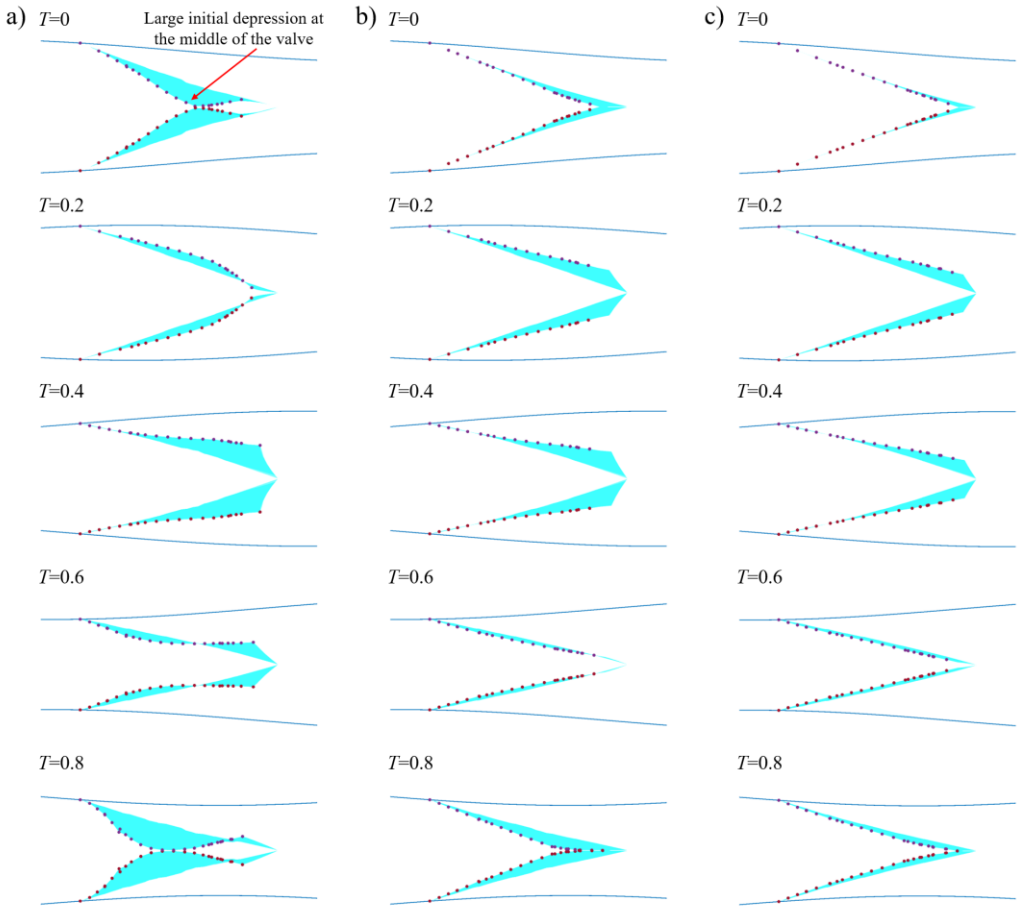

Figure 4.11 a) Deformation of valves with $K_b = 11$, b) with $K_b = 88$, c) with $K_b = 263$ at different instances of the vessel contraction cycle. The dots represent leaflet position at the centerline. The simulation parameters are $\Delta P = 140$, $\phi = 0.2$, $Re = 0.4$, and $K_s = 115$.

4.5.2 Flow rate and valve opening variation

The behavior of the elastic valves can be further characterized by analyzing the time evolution of the flow rate Q_s and the leaflet cross-sectional opening area A that are shown in Figure 4.12 for flow with and without an adverse pressure gradient. The flow rate Q_s is averaged over the entire simulation domain. Note that for a valve-less vessel, Q_s

remains constant as shown by the dotted lines in Figure 4.12a and Figure 4.12c. Figure 4.12b and Figure 4.12d also show the vessel radius at the valve location.

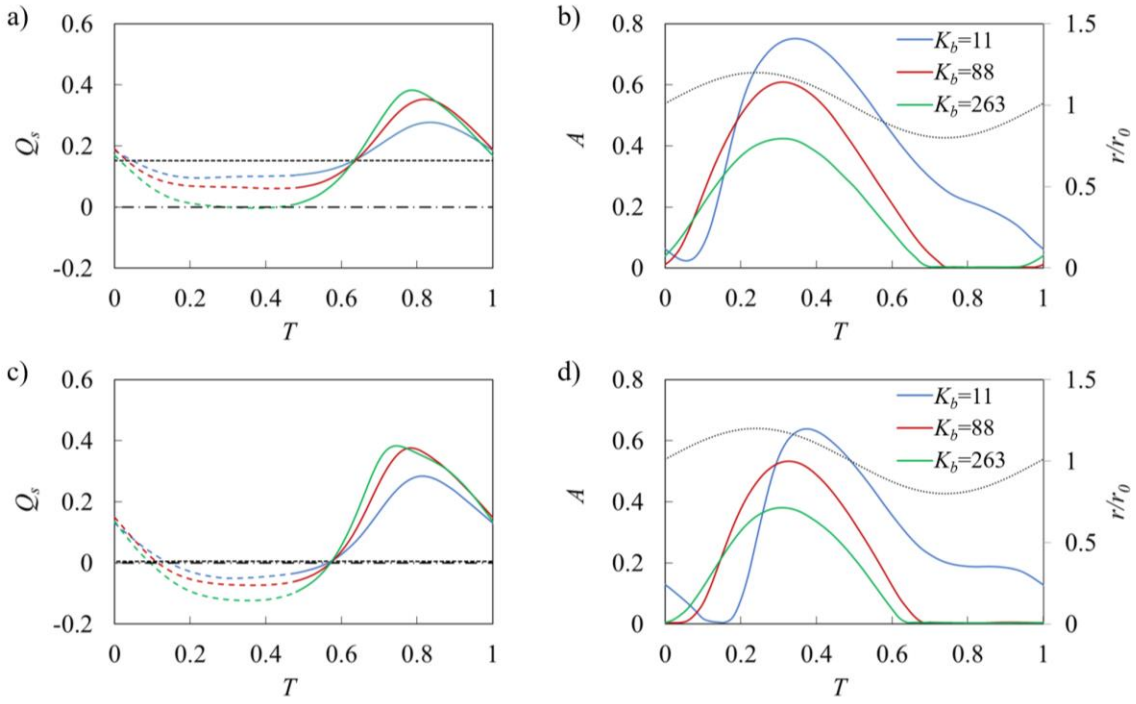

Figure 4.12 a) Time evolution of flow rate in vessels with $\Delta P = 0$. b) Time evolution of valve opening area A in vessels with $\Delta P = 0$. c) and d) are the same as a) and b) but with $\Delta P = 140$. The flow rate is averaged over contraction wavelength. The horizontal dashed line represents flow rate in the valve-less vessel while the dotted lines in b) and d) represent normalized vessel radius near the valve (r/r_0). Dashed lines in a) and c) indicate when $r/r_0 > 1$ while solid lines indicate $r/r_0 < 1$. Horizontal dash-dot lines in a) and c) denote $Q_s = 0$. The simulation parameters are $\phi = 0.2$, $Re = 0.4$, and $K_s = 115$.

The valves open when the vessel diameter at the valve location increases (Figure 4.12b and Figure 4.12d), which corresponds to the forward fluid flow through the valve (Figure 4.5). The valve opening is maximized when the vessel diameter is near its mean value. Softer valves can open more widely during flow through the valve and stay open longer. Furthermore, for such valves the opening starts later than for stiffer valves. Comparing the flow with and without an adverse pressure gradient we find that the adverse

pressure gradient suppresses valve opening with the effect being more significant for softer valves. This can be attributed to the lower flow velocity and favorable pressure gradient for valve opening when the flow is affected by an adverse pressure.

The valve kinematics strongly affects the flow rate in the vessel (Figure 4.12b and Figure 4.12d). When the valves are open, softer valves impose lower resistance on the flow leading to a faster flow. However, even with the softest valve, the instantaneous flow rate with an open valve is slower than in the case of a valve-less vessel. When the valves are closed, the flow rate increases and exceeds the valve-less flow rate. Stiffer valves that close sooner enable a larger mean flow rate. Thus, during the oscillation period, the fluid is mostly pumped when the valves are closed, and the fluid is transported by the contracting wave propagating along the vessel. This behavior is more evident when the flow is confronted with an adverse pressure gradient (Figure 4.12c). In this case, the flow rate is negative when the valves are open, and the fluid is transported in the positive direction only when the valves are closed. Note that for the same adverse pressure gradient valve-less vessel generates a nearly zero net flow.

We therefore conclude that valve elasticity has opposing effects on the pumping performance. Softer valves enable greater valve opening, reducing viscous losses when the flow is moving in the positive directions through the valve. On the other hand, stiffer valves can close more rapidly during backflow minimizing flow reversal during this phase. This indicates that an optimum valve of elasticity exists that maximizes the vessel pumping performance.

4.5.3 Pumping parameter variation

Figure 4.13 presents the pumping parameters as a function of valve bending elasticity K_b for vessels with $\Delta P = 140$ and two wave amplitudes $\phi = 0.2$ and $\phi = 0.25$. We indeed find that the flow rate is maximized when $K_b \approx 63$ (Figure 4.13a). This optimum bending elasticity is about the same for both contraction wave amplitudes. The pumping efficiency and economy (Figure 4.13c and Figure 4.13d) also exhibit maxima with K_b. Here, the optimum elasticity $K_b \approx 50$ is somewhat lower than that for the maximum flow rate.

We also find that work done by the vessel W gradually increases with increasing K_b (Figure 4.13b). The work increase is related to the higher viscous losses associated with less deformable valve leaflets [49] that exhibit a lower valve opening area (Figure 4.13e). These figures show that this trend is independent of the wave amplitude. While A_{max} steadily decreases with increasing K_b, the time the valve stays closed T_c is nearly independent of K_b for $K_b > 50$, and sharply decreases for lower K_b. This indicates that softer valves are unable to properly close and fail to prevent the backflow in the vessel.

In Figure 4.13, we also examine the effect of the leaflet in-plane stiffness K_s on the valve performance. We compare valves with $K_s = 23$, 115, and 575. We find that a nearly 25-fold change of in-plane stiffness has a minor effect on the vessel parameters such as flow rate Q, work done by the vessel W, efficiency η, and economy ε. Only a slight decrease of A_{max} is found for the valves with $K_s = 575$ compared to the less stiff valves. Interestingly, the time that valve is closed T_c is practically insensitive to changes in K_s.

Thus, we conclude that the valve behavior is mostly defined by the valve bending elasticity whereas in-plane stiffness plays a minor role.

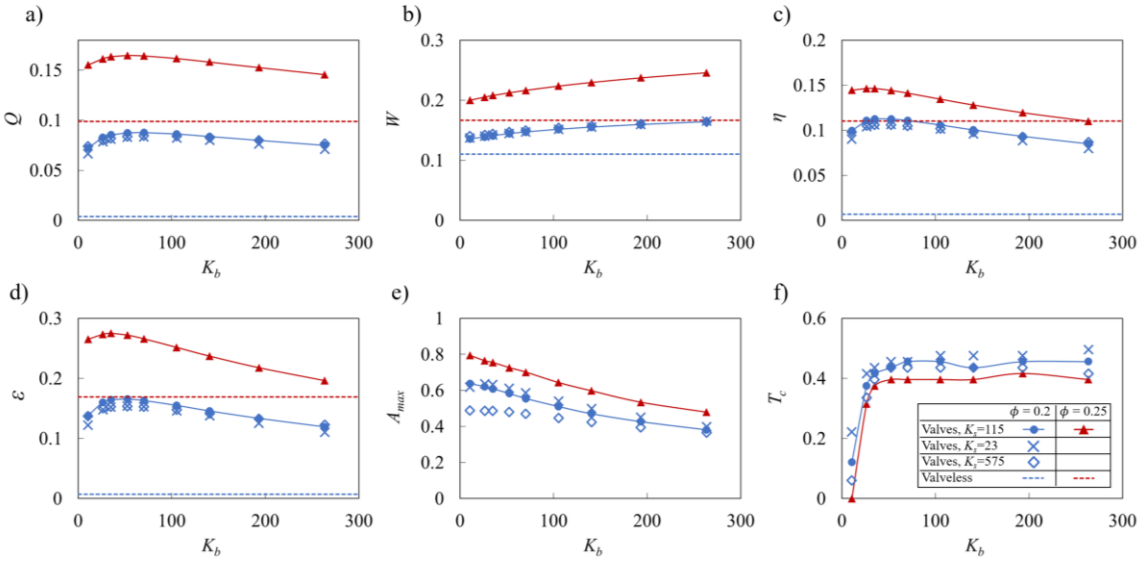

Figure 4.13 a) Flow rate, b) vessel work, c) pumping efficiency, d) pumping economy, e) maximum valve opening area A_{max}, and f) valve closure time T_c as a function of valve bending stiffness K_b for vessels with $\Delta P = 140$ and $Re = 0.4$. The dashed lines represent results from valve-less cases. The valve is considered closed when $A < 0.05$.

4.5.4 Variation of optimal K_b under different adverse pressure gradient

The emergence of an optimum K_b indicates that the vessel mechanical properties can be optimized for specific pumping conditions. Furthermore, the optimum K_b leading to the fastest pumping performance and the highest efficiency and economy are somewhat different due to the dependency of W on K_b. Indeed, increasing W with K_b results in the softer valve being more efficient while providing slightly slower pumping. In Figure 4.14, we examine the dependency of the optimum valve elasticity on the magnitude of the adverse pressure gradient. The figure shows that the optimum elasticity increases with ΔP. We relate this trend to the improved ability of stiffer valves to withstand backflow due to

an increasing adverse pressure gradient as such valves can close faster than softer valves (Figure 4.12d). When ΔP increases, flow rate in the vessel reduces and the ability to prevent the backflow has more significant effect on the pumping than increased viscous losses due to stiffer valves.

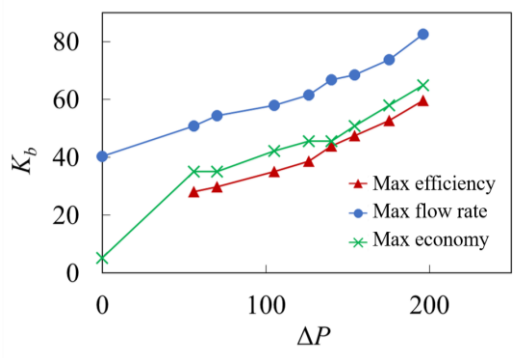

Figure 4.14 Optimal normalized bending stiffness yielding the maximum efficiency, economy, and flow rate under different adverse pressure gradients. The simulation parameters are $\phi = 0.2$, $Re = 0.4$, and $K_s = 115$.

4.6 ΔP-dependent contraction amplitude

In the lymphatic system, the vessel contraction amplitude depends on the magnitude of the adverse pressure gradient [14]. As shown in Figure 4.15, contraction amplitude gradually decreases with increasing ΔP. The decrease is more rapid for lower ΔP and the amplitude converges to a non-zero value when the pressure gradient increases beyond $\Delta P > 1000$ due to the inability of the lymphatic muscle cells to generate enough force for the pressure in the vessel proximal to the valve to exceed the pressure distal to the valve.

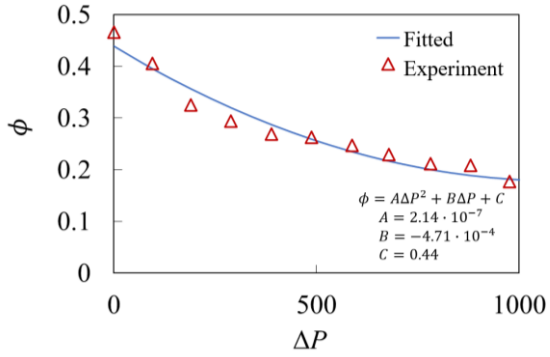

Figure 4.15 Contraction amplitude as a function of normalized pressure difference. Experimentally reported values [14] are shown by the triangles while the fit is shown by the solid line.

In Figure 4.16, we examine the effects of the pressure dependence of the contraction amplitude on the pumping performance. To isolate these effects, we compare normalized flow rate Q, work done by the vessel W, and pumping efficiency η for a vessel with pressure dependent contraction amplitude to a vessel with a constant contraction amplitude. For the later vessel, we set the contraction amplitude such that the amplitudes for both vessels are identical when $\Delta P = 0$. The data is presented for two values of Re.

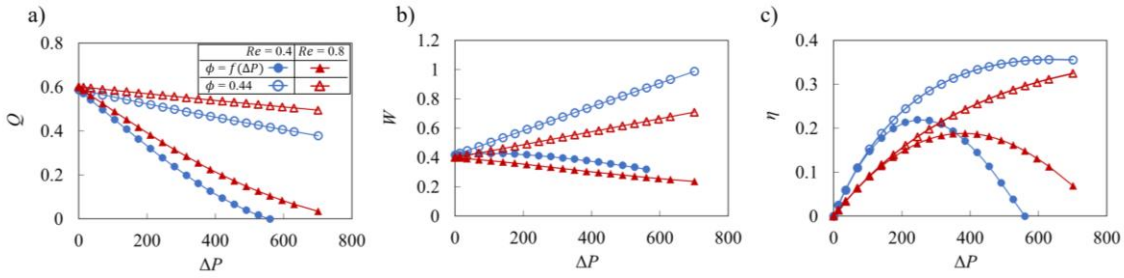

Figure 4.16 a) Flow rate, b) vessel work, and c) pumping efficiency as a function of the pressure gradient for vessels with and without pressure-dependent contraction amplitude. The valve elasticity is $K_b = 88$, and $K_s = 115$. Without adverse pressure gradient both the vessels exhibit an identical contraction amplitude of $\phi = 0.44$.

The simulations show that vessels with pressure dependent amplitude significantly underperform compared to the constant amplitude vessels, resulting in a rapid decrease of

the pumping flow rate with increasing adverse pressure gradient (Figure 4.16a). This trend is consistent with the results shown in Figure 4.10a indicating a reduction in pumping rate with lower contraction amplitude. Pressure dependent contraction amplitude also has significant effect on the work done by the pumping vessel. As shown in Figure 4.16b, constant contraction amplitude leads to an increasing amount of work as the adverse pressure increases. By contrast, the pressure dependent amplitude results in work that is nearly independent from ΔP. This result suggests that lymphatic vessel contraction amplitude is limited by the work of contractile muscles driving vessel contraction and that once exposed to an adverse pressure gradient, lymphatic muscle quickly achieves maximum capacity in terms of the work generated. It is also interesting to note that the work only slightly changes with Re. Furthermore, pressure dependent contraction amplitude decreases the pumping efficiency compared to the constant amplitude case (Figure 4.16c). Although the work is roughly constant with pressure, the decreasing Q in the pressure dependent vessels results in a rapid decrease in efficiency when ΔP is sufficiently large. As a result, the optimum pumping occurs at lower values of ΔP compared to the vessels with a constant contraction amplitude.

CHAPTER 5. ROLE OF VALVE PLACEMENT ON LYMPHATIC PUMPING

5.1 Introduction

Due to the need to establish fundamental understanding and evaluation of pumping performance under different parameters for a contracting vessel, many aspects of the model were not explored in the previous chapter. Two primary examples of this are the effects of valve placement and wavelength of the contraction wave. By fixing the valve spacing and contraction wave's wavelength to be equal to each other, synchronous valve deformation was induced for a given lymphangion. This allowed a simpler flow disruption by the valve, leading to a more fundamental investigation of valve's effect on pumping performance.

Although the simulated model's valve spacing or contraction wavelength are within the experimentally reported range (as shown in the previous chapter), it is highly unlikely for valve spacing and contraction wavelength to consistently match to induce synchronous motion. Thus, this chapter further utilizes the modified model of contracting vessel with valves from the previous chapter and explores the effect of valve spacing and contraction wavelength on pumping performance. Particularly for valve spacing, two distinct patterns are studied. First pattern assumes uniform inter-valve spacing with varying distance while the second pattern implements a pattern with repeated nonuniform valve placement. Combined with the variation of contraction wavelength, the effect of these three conditions on pumping performance is explored.

This chapter first investigates the effect of valve spacing under uniform valve placement. While varying the inter-valve spacing with a fixed contraction wavelength, fundamental understanding of the valve placement's effect on flow pattern and performance is studied via means such as axial velocity profile, centerline velocity profile, and flow rate gains between cases with and without valves under various valve spacing. Once this general understanding is established, flow performance metric like in the previous chapter is calculated over different valve spacing and contraction wavelength. Then, the chapter investigates the effect of nonuniform valve placement through axial velocity profile, centerline velocity profile, and flow rate gains between cases with and without valves. Finally, the same performance metric is evaluated, and the relationship between flow performance between two valve placement patterns is discussed.

5.1.1 Nondimensional numbers and simulation parameters

While the same dimensional and nondimensional variables are used from the previous chapter with contracting vessel, additional variables are introduced to account for variation of valve placement. The definition of these variables in relations to the model geometry is shown below in Figure 5.1.

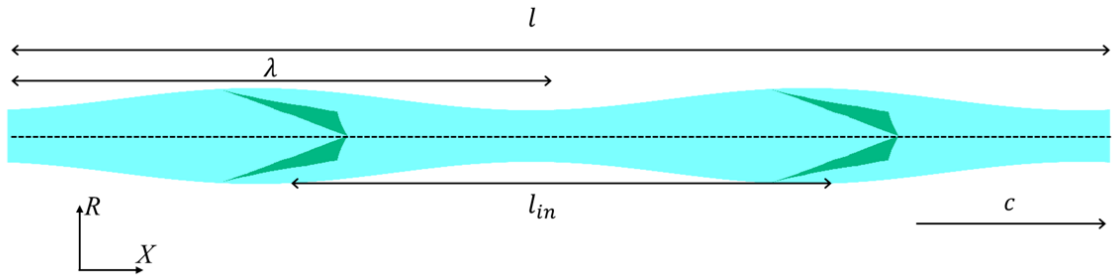

Figure 5.1 Model of a periodic contracting vessel fitted with two valves with relevant valve spacing parameters defined. Note that for this chapter, the number of valves within the

model n_{valves} can vary, as well as the total domain length l. Coordinate R denotes radial coordinate while X denote axial coordinate. Even though the simulations are conducted in a Cartesian coordinate system, radial coordinate is implemented for contraction since radial contraction is applied on the vessel.

Under uniform valve spacing, the distance between two neighboring valves is defined as l_{in}. Due to its periodic boundary condition, the length of the domain l, number of valves n_{valves}, and inter-valve distance under uniform valve spacing are related as $l_{in} = l/n_{valves}$. Nondimensionalized variables for l_{in} is defined as $L_{in} = l_{in}/\lambda$. The wavelength is normalized as $\Lambda = \lambda/2r_0$ and is used when inspecting the effect of contraction wavelength on pumping performance.

For studying the effect of irregular valve spacing on pumping performance, a single pattern of nonuniform valve placing was created for this chapter. The geometry of this model is shown in Figure 5.2.

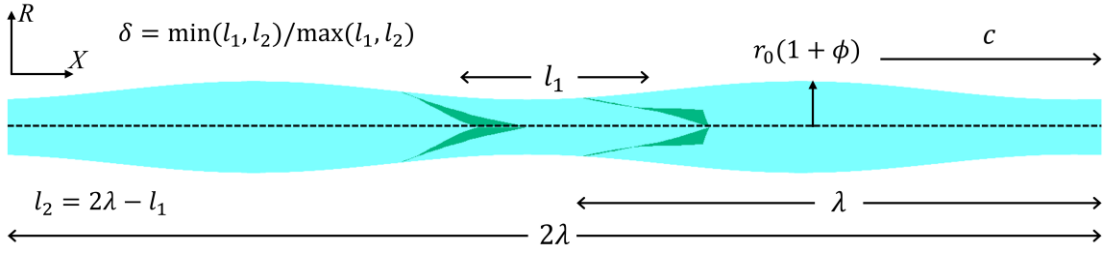

Figure 5.2 Model of a periodic contracting vessel fitted with two valves with nonuniform valve spacing. Coordinate R denotes radial coordinate while X denote axial coordinate. To gauge the degree of nonuniformity, a ratio between smaller and larger inter-valve spacing δ is defined.

For studying the effect of nonuniform valve spacing, a configuration with alternating valve spacing is used. For this configuration, only two valves are placed for each vessel length equaling to two contraction wavelengths, putting the average L_{in} to 1

for a given vessel segment of length 2λ. However, when the model is focused on a region with vessel length of 2λ and two valves, as seen in Figure 5.2, a distinct spacing pattern emerges. The two unique spacing can be separated as the inner inter-valve spacing l_1 and outer inter-valve spacing l_2. From these two alternating spacings, the degree of nonuniformity δ is defined as $\delta = \min(l_1, l_2)\,/\max(l_1, l_2)$, which is the ratio between smaller and larger of the two valve spacings. This configuration places the limit of δ as $0 < \delta \leq 1$. But in reality, the lower limit of δ will be greater than 0 to prevent overlapping of valves at such low values of δ. Also, note that the outer inter-valve spacing is still considered inter-valve spacing even at domain boundary since the model has a periodic boundary condition.

Parameters not specifically defined above have the same definition as previous chapter, as outlined in Table 4.2. However, there is one exception when describing the effect of adverse pressure gradient under different contraction wavelengths. Previous chapter uses pressure difference per contraction wavelength following relevant literature [50], and this definition and applied adverse pressure gradient could be used interchangeably through a constant multiplier since the contraction wavelength was a constant. However, this definition creates a variable Δp_λ under different λ, even though the applied adverse pressure gradient is constant. To address this, a normalized adverse pressure gradient $dP_x = (\partial p/\partial \mathrm{x})_x \mathrm{r_0}^3 \rho/\mu^2$, where $(\partial p/\partial \mathrm{x})_x$ is the applied adverse pressure gradient.

Finally, note that this chapter mostly keeps vessel length 60 times r_0, making $l/r_0 = 60$. However, to get finer data points of L_{in}, l/r_0 may extend to $l/r_0 = 75, 80, 90$

in some cases. Results from different vessel lengths were compared in a consistent manner by keeping their $\Delta P, dP_x, Re, \phi, K_b, K_s, AR, L_{in}, \Lambda$, and δ from their shorter counterparts.

5.1.2 Survey of relevant experimental data

Although most of the relevant experimental data from previous chapter still applies, further examination is done for contraction wavelength and valve spacing. For contraction wavelength, experimental data from previous chapter reports a wide range of normalized wavelength Λ between 0 and 30. Even when the contraction wavelength is varied, our simulated Λ is from 5 to 15 with majority of cases around $\Lambda = 7.5$, which falls well within the experimental range.

Previous chapter sets inter-valve spacing equal to the contraction wavelength, which makes $L_{in} = l_{in}/\lambda = 1$ and $\delta = 1$. This can be compared with the experimentally reported lymphangion length since a lymphangion is defined as a region between two consecutive valves. Work by Margaris and Black [99] reports a collecting lymphangion length of $1{\sim}2$mm, but when compared with vessel diameter, this puts the ratio between lymphangion length and vessel diameter as $l_{in}/2r_0 = 1{\sim}10$. Our work varies valve spacing from $l_{in}/2r_0 = 3{\sim}37.5$ with majority of cases tested in $l_{in}/2r_0 \sim 7.5$. Although the maximum ratio can go over the range reported experimentally, majority of the cases fall within the experimental range, thus making a reasonable variation of valve spacing when compared to the vessel diameter.

Furthermore, the valve spacing can be compared with the contraction wavelength calculated from previous chapter, which is in the range of 0 to 81mm. Although this is a very large range for calculating $L_{in} = l_{in}/\lambda$, we can see that minimum L_{in} can fall as low

as L_{in}~0.01 if the minimum spacing of 1mm and maximum wavelength of 81mm is used. Considering that our work has a range of $L_{in} = 0.2\sim4$, this is well within the range of experimentally reported L_{in}.

5.2 General flow pattern and valve deformation

Like in the previous chapter, flow pattern and valve deformation are first analysed. The axial velocity profile and valve deformation for $L_{in} = 0.67$, $\Lambda = 7.5$, $\Delta P = 140$, $\phi = 0.25$, $Re = 0.4$, $K_b = 88$, and $K_s = 115$ under different phases of the contraction cycle T is shown below at Figure 5.3.

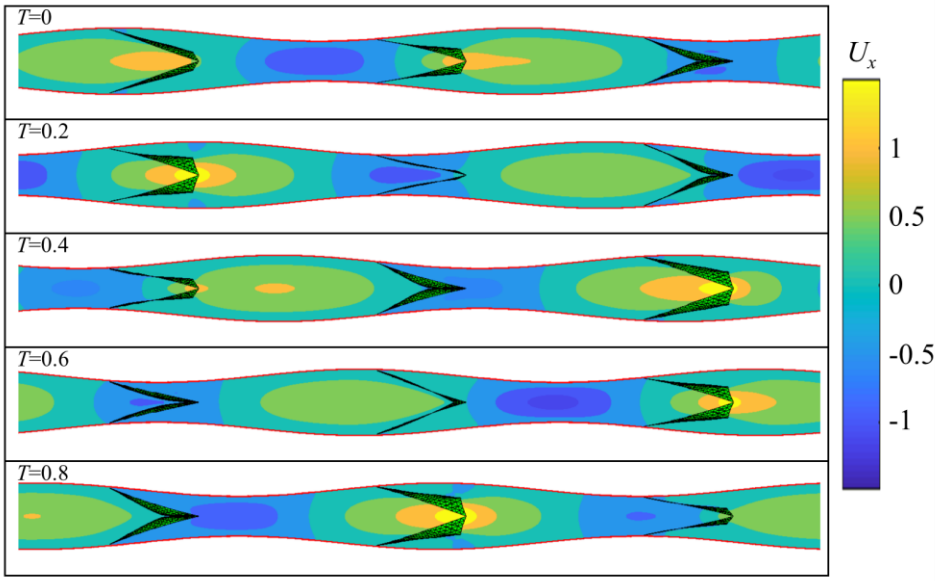

Figure 5.3 Axial flow velocity U_x for $L_{in} = 0.67$, $\Lambda = 7.5$, $\Delta P = 140$, $\phi = 0.25$, $Re = 0.4$, $K_b = 88$, and $K_s = 115$ under different phases of the contraction cycle T. Note the asynchronous valve deformation due to mismatch between the valve placement and vessel contraction wavelength.

Unlike cases where $L_{in} = 1$ from Figure 4.5, one of the most notable features in Figure 5.3 is the asynchronous valve deformation. Unlike in the previous chapter where all

valves underwent the same vessel expansion and contraction for a given time, different valves can now undergo different vessel expansion stage and consequentially, different velocity packets encountered for a given time. Note that a valve is expected to deform synchronously only when L_{in} is an integer value.

The impact of asynchronous valve deformation is also reflected on velocity profile with nonuniform disturbance by the valves. Valves no longer simultaneously encounter the same velocity packets for a given time, leading to different valves passing forward flow with flow reduction and preventing backflow at the same time. This also means that unlike in synchronous valve deformation, there is a higher likelihood for at least one valve to encounter a negative velocity packet to prevent backflow during any given stage in its contraction cycle. And once backflow prevention via valve occlusion occurs in at least one of the valves, the other non-disturbed negative velocity packets also experience partial reduction in their magnitudes due to mass conservation, as shown most notably in $T = 0.4$ in Figure 5.3. Given that a valve improves pumping through backflow prevention, this observation indicates that asynchronous valve deformation may improve pumping due to its higher likelihood for backflow prevention by at least one of the valves during a contraction cycle.

To further investigate the effect of asynchronous valve deformation, axial velocity difference between cases with and without valves is plotted as Figure 5.4.

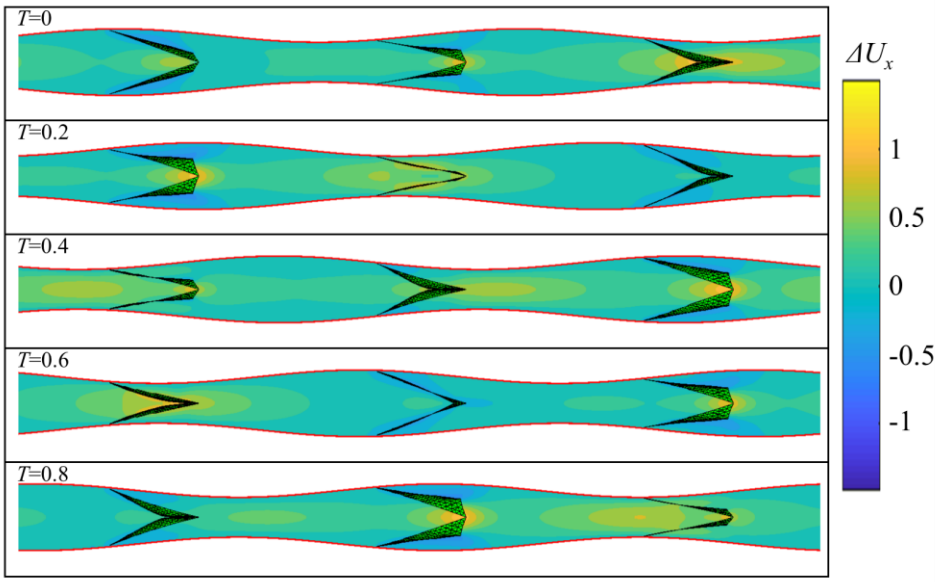

Figure 5.4 Axial flow velocity difference ΔU_x for $L_{in} = 0.67$, $\Lambda = 7.5$, $\Delta P = 140$, $\phi = 0.25$, $Re = 0.4$, $K_b = 88$, and $K_s = 115$ under different phases of the contraction cycle T. Note the asynchronous valve deformation due to mismatch between the valve placement and vessel contraction wavelength.

Like the analysis from Figure 5.3, Figure 5.4 shows nonuniform improvement in axial velocity during different stages of the contraction cycle. However, there exists some region of velocity increase during all stages of the contraction cycle unlike its synchronous counterparts in Figure 4.6. Regions of velocity increase despite minimum valve interference can also be observed in $T = 0.4$ and 0.8, supporting the observation from Figure 5.3. These findings indicate that asynchronous valve deformation caused by mismatching valve spacing with contraction wavelength not only improves pumping by inducing more effective backflow prevention, but also allows a smoother improvement in pumping compared to its valveless counterpart.

5.3 Uniform valve spacing

5.3.1 Centerline axial velocity profile

To further investigate the effect of uniform valve spacing L_{in} on flow profile and pumping performance, centerline velocity profile of axial velocity is plotted under different stages of the contraction cycle. Centerline velocity profiles under two different uniform valve spacings of $L_{in} = 0.67$ and 1 are plotted in Figure 5.5, allowing a further comparison between cases with uniform and nonuniform valve deformations.

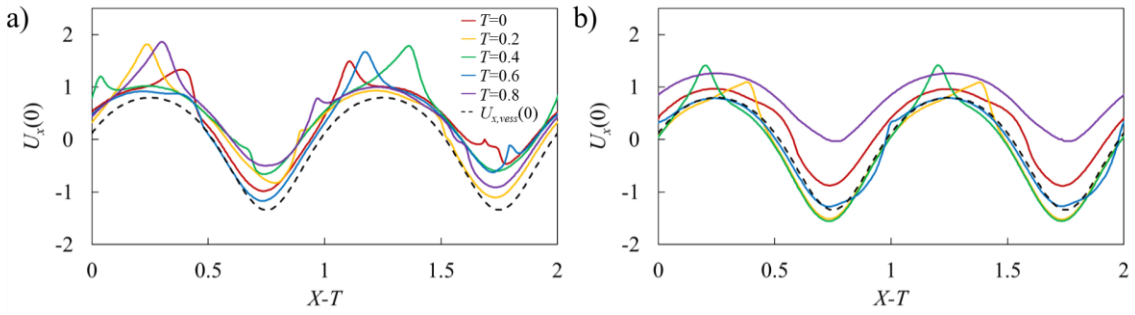

Figure 5.5 a) Centerline axial velocity $U_x(0)$ for $L_{in} = 0.67$, $\Lambda = 7.5$, $\Delta P = 140$, $\phi = 0.25$, $Re = 0.4$, $K_b = 88$, and $K_s = 115$ under different phases of the contraction cycle T. b) Centerline axial velocity $U_x(0)$ for $L_{in} = 1.0$, $\Lambda = 7.5$, $\Delta P = 140$, $\phi = 0.25$, $Re = 0.4$, $K_b = 88$, and $K_s = 115$ under different phases of the contraction cycle T. Note the centerline velocities are plotted under a moving frame of reference $X - T$ while black dashed lines show centerline velocity for cases without valves.

Several notable features can be seen from Figure 5.5. First, cases with nonuniform valve spacing in Figure 5.5a shows non-repeating centerline velocity profiles for every $X - T$ for all stages of the contraction cycle. Due to asynchronous valve deformation from non-integer L_{in}, this is expected and alluded from Figure 5.3 and Figure 5.4. Second, Figure 5.5a shows a narrower distribution of its centerline velocity throughout all stages of the contraction cycle. This supports the observation of Figure 5.4, where a more even

distribution of flow increase throughout the contraction cycle under asynchronous valve deformation may lead to a more consistent improvement in pumping.

Finally, it is also worth noting the position of centerline velocities relative to their valveless counterparts marked in black dashed lines. Unlike synchronous deformation in Figure 5.5b, centerline velocities in Figure 5.5a do not go lower than their valveless counterparts in all stages of the cycle throughout most of $X - T$. This is noticeably different from synchronous cases where centerline velocities during roughly half of the contraction cycle is slightly or noticeably below its valveless counterparts due to loss in forward flow from valve. Much like the findings from previous two figures, this may indicate an overall flow improvement through mismatching valve spacing and contraction wavelength. However, Figure 5.5b shows a significantly large improvement in centerline velocity profile during certain stages of the contraction cycle unlike its asynchronous counterparts in Figure 5.5a. Although hinted, this means that further analysis is needed to accurately capture the variation in flow performance by valve spacing compared to contraction wavelength.

5.3.2 Time-averaged gain in flow rate under different valve spacing

To further understand the effect of uniform valve spacing on flow, an additional parameter is introduced. For a given axial position X, flow rate is evaluated as a function of time, giving $Q(X,T)$. This flow rate is then compared against cases without valves as $\Delta Q_{total}(X,T) = Q(X,T) - Q_{vess}(X,T)$, where $Q_{vess}(X,T)$ is flow rate under a valveless vessel. This value is then split based on whether $Q_{vess}(X,T)$ undergoes forward flow for a

given time and space (i.e. $Q_{vess}(X,T) > 0$) or backward flow (i.e. $Q_{vess}(X,T) < 0$). The time averaged value of this for forward flow is defined as

$$\Delta Q_{for}(X) = \frac{1}{c\pi r_0^2 \tau}\int_0^1 \Delta Q_{f}(X,T)dT \tag{32}$$

$$\Delta Q_f(X,T) = \begin{cases} \Delta Q_{total}(X,T)\ if\ Q_{vess} > 0 \\ 0\ if\ Q_{vess} < 0 \end{cases} \tag{33}$$

The counterpart for backflow is defined as

$$\Delta Q_{back}(X) = \frac{1}{c\pi r_0^2 \tau}\int_0^1 \Delta Q_{b}(X,T)dT \tag{34}$$

$$\Delta Q_b(X,T) = \begin{cases} 0\ if\ Q_{vess} > 0 \\ \Delta Q_{total}(X,T)\ if\ Q_{vess} < 0 \end{cases} \tag{35}$$

The difference in flow rates between the cases with and without valves averaged over a contraction cycle provides a more accurate evaluation of pumping improvement under different valve configuration. Then, by splitting the improvement between when positive or negative velocity packets pass through, even more detailed analysis can be made in pumping improvement. Plots of ΔQ_{for} and ΔQ_{back} under three different L_{in} of $L_{in} = 0.67, 1, 1.33$ are plotted in Figure 5.6.

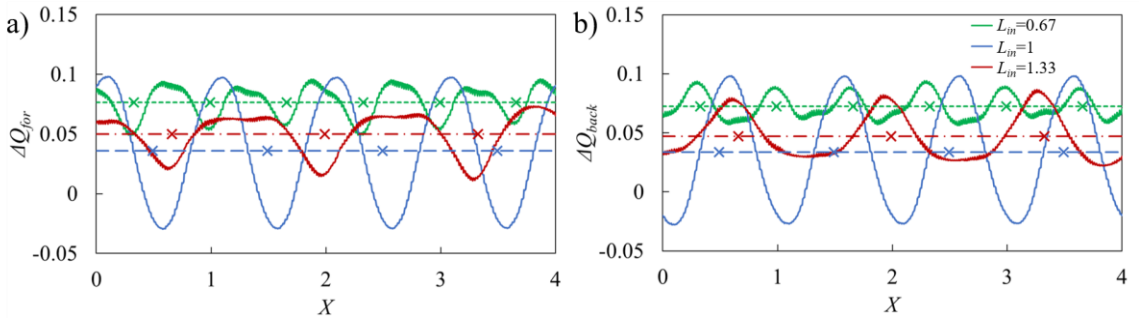

Figure 5.6 a) Time-averaged normalized flow rate gain under forward flow ΔQ_{for} for $\Lambda = 7.5$, $\Delta P = 140$, $\phi = 0.25$, $Re = 0.4$, $K_b = 88$, and $K_s = 115$ under different L_{in}. Note the dashes with matching colors represent spatially averaged values for respective time-averaged flow rate gains. b) Time-averaged normalized flow rate gain under backward flow ΔQ_{back} for $\Lambda = 7.5$, $\Delta P = 140$, $\phi = 0.25$, $Re = 0.4$, $K_b = 88$, and $K_s = 115$ under different L_{in}. Note the dashes with matching colors represent spatially averaged values for respective time-averaged flow rate gains while the mean axial positions of every valve for a given case are marked with crosses.

Two plots of ΔQ_{for} and ΔQ_{back} in Figure 5.6 reveal several interesting features, especially when valve spacing is varied compared to contraction wavelength. First in general, there is a noticeable drop in ΔQ_{for} and bump in ΔQ_{back} around the valve locations, where their mean axial positions are noted in crosses in Figure 5.6. This supports the effect of valve on flow as shown previously. When positive velocity packets encounter forward flow shown in Figure 5.6a, dissipation of forward flow momentum by the valves' flow resistance creates a reduction in flow rate gained. In a limiting case of $L_{in} = 1$, flow rate is actually lower than the valveless counterpart, noted by the negative ΔQ_{for} around valve locations. When the valve encounters backflow, the flow rate gain increases around the valve location, again supporting the valves' role of backflow reduction. Overall, the shapes of ΔQ_{for} and ΔQ_{back} deviate from a sinusoidal pattern if L_{in} is not an integer.

More evenly distributed reduction in backflow under asynchronous valve deformation also increases minimum gain in flow rate throughout model while the

difference between maximum and minimum ΔQ_{for} and ΔQ_{back} decreases, supporting the observation of centerline velocity profile in Figure 5.5. Although the maximum ΔQ_{for} and ΔQ_{back} is higher for $L_{in} = 1$ compared to $L_{in} = 1.33$, again consistent with Figure 5.5, this increased flow rate gain is not enough to compensate for increased minimum ΔQ_{for} and ΔQ_{back} under asynchronous valve deformation. Thus, when the flow rate gain is also averaged over space, noted in corresponding dashed lines, average flow rate gain in forward flow and backflow under $L_{in} = 1$ is the lowest of the three valve placement configurations plotted.

Finally, having lower non-integer L_{in} increases spatially averaged ΔQ_{for} and ΔQ_{back}, thus increasing pumping performance under both forward and backward flows. Furthermore, the difference in maximum and minimum ΔQ_{for} and ΔQ_{back} is smaller when L_{in} is a lower non-integer value. This may be attributed from the increased number of valves to create a smaller and uniform inter-valve spacing, which provides a greater frequency of backflow reduction occurring from at least one valves within the system. Furthermore, increased number of valves may provide a more evenly distributed backflow reduction throughout the contraction cycle, thus providing a smaller variation in flow rate gain regardless of proximity to valves or if the valves encounter forward or backward flow. Overall, this demonstrates that through a more effective implementation of backflow reduction, asynchronous valve deformation by mismatching of valve spacing and contraction wavelength improves overall pumping and provides pumping improvement more steadily.

5.3.3 Pumping parameter variation

The effect of uniform valve spacing on pumping parameters is plotted on Figure 5.7. Of the parameters listed on Table 4.2, only the flow rate Q, work done by the vessel W, and pumping efficiency η are plotted as a function of uniform valve spacing relative to contraction wavelength L_{in}. For flow rate, there is a noticeable dip in integer L_{in} with generally increasing flow rate with lower L_{in}, which is expected from previous analysis. The dip of Q at $L_{in} = 1$ is slightly lower than Q at $L_{in} = 2$, indicating that pumping with twice the valve spacing and half the number of valves under synchronous valve deformation has little effect on pumping performance between $L_{in} = 1$ and 2. In fact, having less valves is slightly more advantageous in most cases by reducing the flow resistance caused by the valves.

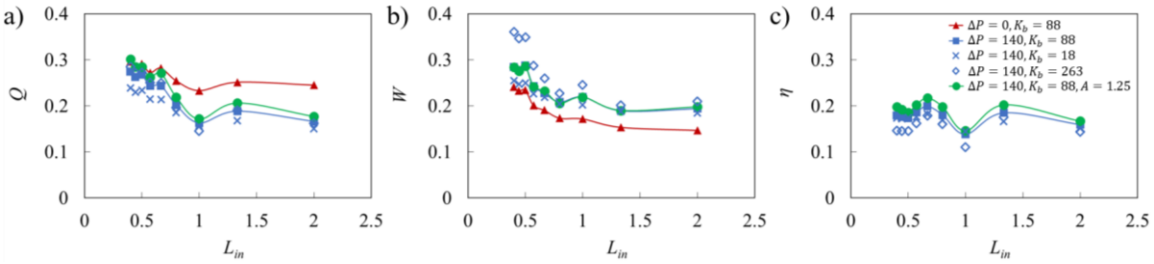

Figure 5.7 a) Flow rate, b) vessel work, and c) pumping efficiency as a function of normalized valve spacing L_{in} for vessels with $\Lambda = 7.5$, $Re = 0.4$, $\phi = 0.25$, and $K_s = 115$. Unless stated otherwise, the valve aspect ratio AR is kept at $AR = 1.75$.

Flow rate as a function of L_{in} follows a similar pattern under different valve elastic and geometric parameters, as well as adverse pressure gradient applied. However, there are some noticeable deviations under $\Delta P = 0$ and $K_b = 18$. When there is no adverse pressure gradient applied, the effect of greater backflow reduction from asynchronous valve deformation is reduced as there is less backflow from no ΔP, which is consistent with

findings from centerline velocity analysis at Figure 4.7. Consequentially, the dip in Q at $L_{in} = 1$ is less pronounced while the flow rate is much higher at higher L_{in} compared to cases with applied adverse pressure gradient.

A noticeable drop in Q compared to other cases occurs as L_{in} is reduced under lower valve bending stiffness K_b. This may be consistent with analysis in Section 4.5, where very flexible valves do not occlude properly under backflow. This added delay to prevent backflow from improper valve closure results in increased backflow and reduced Q. And since lower L_{in} means increased number valves within the model, the less effective backflow reduction at lower K_b stacks up as L_{in} decreases, creating a greater drop in Q compared to other cases. Finally, a minor increase in Q can be seen for valves with lower aspect ratios, which can be attributed to lower flow resistance from valves due to their shorter lengths.

For work done by the vessel W, there is a generally increasing trend as L_{in} becomes lower. This is expected since lower L_{in} under uniform valve spacing means higher number of valves within the system, which requires more work supplied from the vessel contraction towards valve deformation.

Aside from the general trend, there are consistent bumps in W for all cases at $L_{in} = 1$ and $L_{in} = 0.5$ although not as significant as decrease in Q around $L_{in} = 1$. This may be attributed to synchronous valve deformation, as they bring about a larger change in velocity profile throughout a contraction cycle as seen in Figure 5.5. This more drastic change in flow throughout a contraction in turn may lead to synchronous valve deformation requiring more work to deform from one configuration to another. Although not an integer, $L_{in} =$

0.5 has an alternating valve deformation with synchronous valve deformation for every other nearby valve. This leads to less evenly distributed backflow prevention from at least one of the valves throughout a contraction cycle, causing a larger change in velocity within a given contraction cycle and larger work needed for valve deformation compared to cases with similar valve spacings. Changes in W under a larger integer L_{in} such as $L_{in} = 2$ are more subtle as there are less valves within the model to have a significant impact.

Variation of W is much more drastic under different K_b, especially on lower L_{in}. This is expected from analysis of Figure 4.13, which shows a monotonically increasing W with increasing K_b. Since cases with lower L_{in} have more valves within the model, the effect of K_b on W becomes more apparent with cases with lower K_b having lower W. Cases with $\Delta P = 0$ also has a noticeable decrease in W compared to cases with adverse pressure gradient. This is an expected behavior from the analysis of Figure 4.10 with valves requiring more work to deform while overcoming greater adverse pressure gradient. Finally, cases with lower aspect ratio have almost an identical profile of W compared to cases with larger AR.

When combined, the efficiency plot under different L_{in} shows two distinct local maxima with much more distinct dips around $L_{in} = 1$. Note that efficiency under $\Delta P = 0$ is not shown since setting $\eta = 0$ when $\Delta P = 0$ due to efficiency's definition. Despite the increase in Q, cases with lower L_{in} do not continue to increase with decreasing L_{in} due to an increase in W being more rapid with decreasing L_{in}. The rapid increase in W and decreased η under lower L_{in} may explain why lymphatic valves are not actually placed

closely, as lymphatic contraction cannot supply a large W like in lower L_{in} while pumping under such configuration is not as efficient.

The effect of W is also highlighted when η is compared between $L_{in} = 1$ and $L_{in} = 2$, where efficiency at $L_{in} = 1$ is more noticeably less than when $L_{in} = 2$ due to a larger work done by the vessel when $L_{in} = 1$. Caused by a significantly larger W at stiffer valves, efficiency is overall lower under stiffer valves. Finally, a minor increase in η is noted for cases with lower valve aspect ratio due to an increase in Q with lower AR.

5.4 Contraction wavelength with uniform valve spacing

5.4.1 Pumping parameter variation

In previous sections, the variation of L_{in} was carried out by changing the inter-valve spacing l_{in} by varying the number of valves n_{valves}. Thus, contraction wavelength λ was kept constant at $\Lambda = 7.5$. Even though varying only the inter-valve spacing captures the effect of mismatching contraction wavelength and valve spacing has on pumping, the contraction wavelength is also varied to change L_{in} to investigate any additional effect that different contraction wavelength has on pumping performance.

Since much of the understanding in flow behavior under different L_{in} has been already investigated, this section only focuses on the variation of pumping parameters due to the change in Λ and inter-valve spacing, resulting in variation of L_{in} under different contraction wavelength. The plots of Q, W, and η under this condition are shown below at Figure 5.8. Note that due to the variation of ΔP from changing Λ, normalized pressure gradient dP_x is kept at a constant value of $dP_x = 9$ for this case. Also, note that contraction

wave speed varies with different Λ, meaning that the normalization factor for Q and W change with Λ and Λ^2 under a constant contraction period, respectively.

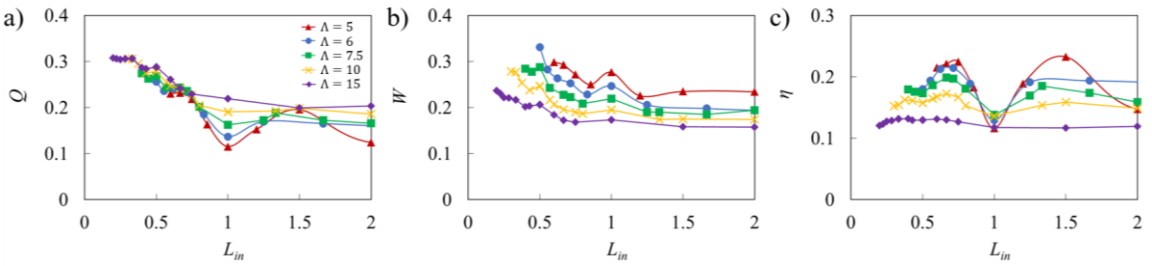

Figure 5.8 a) Flow rate, b) vessel work, and c) pumping efficiency as a function of normalized valve spacing L_{in} under different Λ for vessels with $dP_x = 9$, $Re = 0.4$, $\phi = 0.25$, $K_b = 88$, $K_s = 115$, and $AR = 1.75$.

In general, the pumping performance has a similar trend regardless of the changes in Λ. Flow rates increase with decreasing L_{in}, work done by the vessel also increases with decreasing L_{in}, and the efficiency has a large dip near $L_{in} = 1$ while remaining relatively steady otherwise.

However, as Λ increases, the particular effect around $L_{in} = 1$ seen in previous section becomes less noticeable, eventually disappearing around $\Lambda = 15$. In an extreme case around $\Lambda = 15$, the flow rate and work done by the vessel increase smoothly and more gradually with decreasing L_{in}, leading to a steady efficiency regardless of inter-valve spacing. This behavior is similar to when the system experiences no applied adverse pressure gradient at Figure 5.7, where backflow reduction becomes less significant due to increased overall pumping from vessel contraction. As Λ increases under a constant contraction period τ, the contraction wave speed correspondingly increases, creating a situation under high Reynolds number much like in Figure 4.8 with $Re = 0.6$. Note that although the peristaltic Reynolds number remain the same under different Λ since

contraction period τ is not changed, the increase in contraction wave speed increases forward flow supplied from vessel contraction, comparable to the high Reynolds number cases in Figure 4.8. Forward flow supplied by high contraction wave speed mitigates applied adverse pressure gradient, makes backflow prevention less important and emphasizes the valve's ability to minimize loss in forward flow from the valve's flow disruption.

This reduces the advantage that models with more valves have in preventing backflow. On the other hand, models with less valves have increased pumping from less flow disruption by the valves, leading to a more gradual increase in Q with lower L_{in}. Furthermore, asynchronous valve deformation reduced backflow more effectively by having a larger portion of the contraction cycle where at least one valve within the model reduces backflow and aids backflow reduction in non-interacting negative velocity packets through mass conservation. But this means that asynchronous valve deformation can have the same effect on flow disruption of forward flow, where there is a greater percentage within a given contraction cycle that at least one valve disrupts forward flow. Then much like backflow reduction, other positive velocity packets are affected by this flow disruption, bringing down the forward flow overall in a greater level. Contrarily, synchronous valve contraction under integer L_{in} will reduce forward flow less, thus reducing the dip in flow rate seen under $\Lambda = 15$.

The reduction in bump for W around $L_{in} = 1$ under higher Λ also follows the analysis from Figure 4.8 under higher Re. Greater forward flow supplied by higher contraction wave speed mitigates the effect of adverse pressure gradient and increases

overall forward flow from vessel contraction. This in turn reduces the magnitude of backflow, thus reducing the positive flow gained from valve's backflow prevention as shown in Figure 4.8d. This less work from the vessel will go to the valves' occlusion against backflow, regardless of how advantageous different valve placement is, thus smoothing out W even around integer L_{in} values.

5.5 Irregular valve spacing

After the effect of uniform valve spacing on pumping has been investigated in previous sections, this section studies variation of pumping under irregular valve spacing, specifically an alternating valve spacing regime outlined in Figure 5.2. Although many fundamental findings have been made through valve placement with uniform spacing, the valves are most likely not spaced uniformly in an actual lymphatic chain. Furthermore, tight valve spacing of $L_{in} < 0.5$ may also be an unrealistic placement even though pumping under tightly spaced valves generally has a higher flow rate.

To explore beyond these limitations, the effect of nonuniform valve placement such as alternating valve spacing on pumping is studied in this section. Like in the previous section, this section will first look at the general flow profile, centerline velocity, and flow rate gain under a model with alternating valve spacing with $0 < \delta \leq 1$. Once a general understanding on the effect of δ on pumping is established, this section will explore the effect of δ on pumping parameters like flow rate, work done by the vessel, and efficiency.

First, flow pattern and valve deformation are first analysed under an alternating valve spacing with $\delta \neq 1$. The axial velocity profile and valve deformation for $\delta = 0.4$,

$\Lambda = 7.5$, $\Delta P = 140$, $\phi = 0.25$, $Re = 0.4$, $K_b = 88$, and $K_s = 115$ under different phases of the contraction cycle T is shown below at Figure 5.9.

In general, the different valve spacings between two consecutive valves create a similar asynchronous valve deformation and flow disruption from cases with $L_{in} \neq 1$, even though the average L_{in} in all valves would be 1. This means that the total time of backflow reduction from at least one valve seem to increase when $\delta \neq 1$. And considering that backflow reduction of at least one of the negative velocity packets in the model reduces backflow magnitude in other packets, this configuration of alternating valve spacing may provide improved pumping through a more effective backflow reduction.

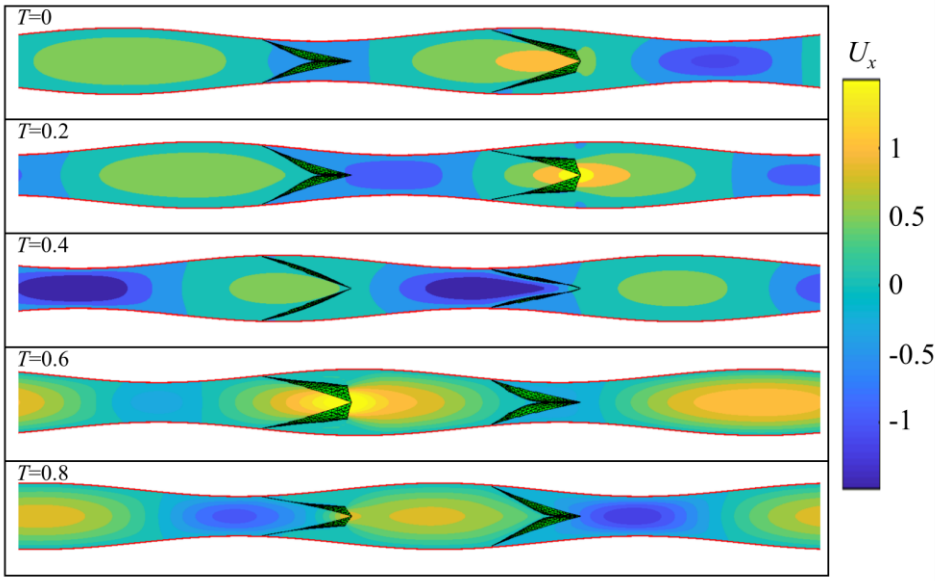

Figure 5.9 Axial flow velocity U_x for $\delta = 0.4$, $\Lambda = 7.5$, $\Delta P = 140$, $\phi = 0.25$, $Re = 0.4$, $K_b = 88$, and $K_s = 115$ under different phases of the contraction cycle T. Note the asynchronous valve deformation due to mismatch between the valve placement and vessel contraction wavelength. Note that due to the model's periodic boundary condition, a combined length between a distance from the right valve to the flow outlet on the right and a distance from flow inlet on the left to the left valve can be also considered an inter-valve spacing from the right valve to the left valve.

Although a greater degree of backflow reduction can be expected from $\delta \neq 1$, a constant number of valves within the model means that the improvement in net flow through variation of δ will be limited. To highlight this, a difference in axial velocities between cases with and without valves is plotted at Figure 5.10. Note that the case with valves has the same model parameters as Figure 5.9. Like ΔU_x plot in Figure 5.4, a wider distribution of backflow improvement can be seen throughout the contraction cycle. However, unlike in uniform valve spacing with asynchronous contraction, some portion of the contraction cycle like at $T = 0.4$ experience a noted lack of flow improvement. In such instances, regions of backflow are either too far from valve or just starting to interact with a valve, in which the valve will begin to deform and not yet block any flow. The density of valves for a given length of a model is not enough to prevent backflow more frequently compared to its counterparts under uniform valve spacing.

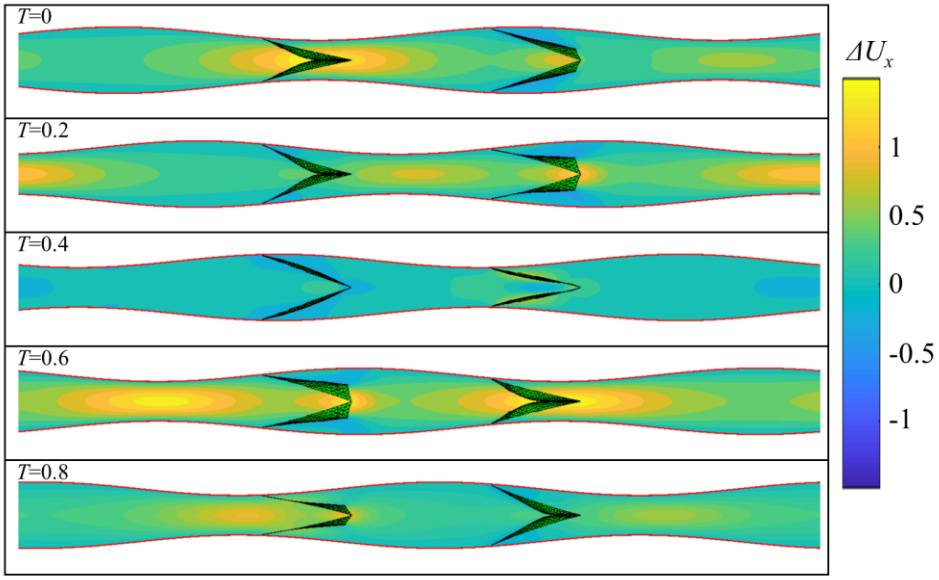

Figure 5.10 Axial flow velocity difference ΔU_x for $\delta = 0.4$, $\Lambda = 7.5$, $\Delta P = 140$, $\phi = 0.25$, $Re = 0.4$, $K_b = 88$, and $K_s = 115$ under different phases of the contraction cycle T.

Note the asynchronous valve deformation due to mismatch between the valve placement and vessel contraction wavelength.

5.5.1 Centerline axial velocity profile and time-averaged flow rate gain

The limited benefit of alternating valve spacing with a fixed number of valves is further investigated with a centerline axial velocity profile comparison between two different valve spacing regimes with $\delta = 0.4$ and $\delta = 1$, shown below on Figure 5.11. Centerline velocity profile of nonuniform valve spacing under $\delta = 0.4$ does share some characteristics with comparable cases under uniform valve spacing such as reduced bandwidth between the highest and lowest centerline velocity, characterizing a distributed backflow reduction throughout the contraction cycle. Still, many aspects of Figure 5.11a resemble features of its counterpart with uniform valve spacing and synchronous deformation in Figure 5.11b. A good example would be a greater concentration of centerline velocity profile near the valveless counterpart noted in black dashed line. Unlike the case with uniform valve spacing in Figure 5.5a, where almost all of the centerline profile clearly stays above the valveless counterpart, instances in contraction cycle like $T = 0.4$ in Figure 5.11a almost coincide and often fall below $U_{x,vess}(0)$. Overall, the centerline velocity profile shows that alternating valve spacing partially incorporates the benefit of increased pumping through a more effective backflow reduction. However, this valve configuration is limited by the fixed number of valves, where more frequent backflow reduction from shorter inter-valve spacing is balanced by the less frequent backflow reduction by the other, longer inter-valve spacing.

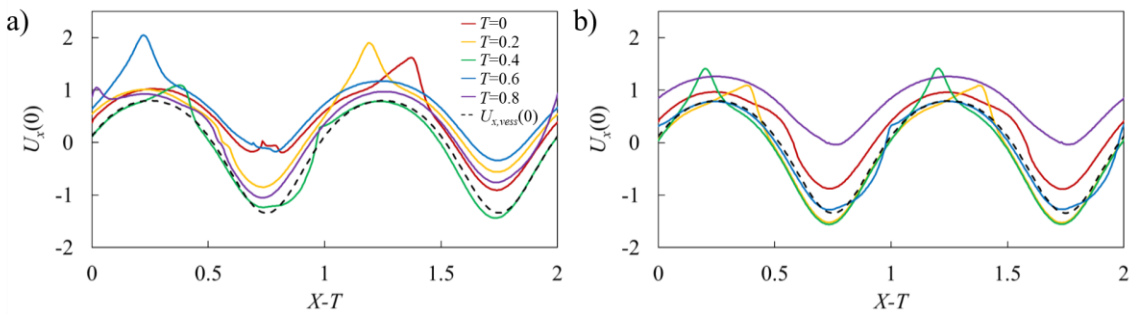

Figure 5.11 a) Centerline axial velocity $U_x(0)$ for $\delta = 0.4$, $\Lambda = 7.5$, $\Delta P = 140$, $\phi = 0.25$, $Re = 0.4$, $K_b = 88$, and $K_s = 115$ under different phases of the contraction cycle T. b) Centerline axial velocity $U_x(0)$ for $\delta = 1.0$, $\Lambda = 7.5$, $\Delta P = 140$, $\phi = 0.25$, $Re = 0.4$, $K_b = 88$, and $K_s = 115$ under different phases of the contraction cycle T. Note the centerline velocities are plotted under a moving frame of reference $X - T$ while black dashed lines show centerline velocity for cases without valves.

In addition to the centerline velocity profile, flow rate gains from forward and backward flow in Figure 5.12 shows alternating valve spacing as a combination of synchronous and asynchronous uniform valve spacing.

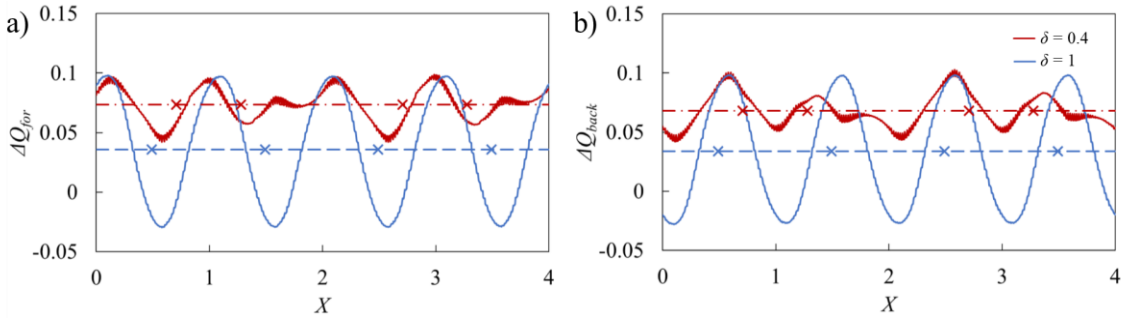

Figure 5.12 a) Time-averaged normalized flow rate gain under forward flow ΔQ_{for} for $\Lambda = 7.5$, $\Delta P = 140$, $\phi = 0.25$, $Re = 0.4$, $K_b = 88$, and $K_s = 115$ under different δ. Note the dashes with matching colors represent spatially averaged values for respective time-averaged flow rate gains. b) Time-averaged normalized flow rate gain under backward flow ΔQ_{back} for $\Lambda = 7.5$, $\Delta P = 140$, $\phi = 0.25$, $Re = 0.4$, $K_b = 88$, and $K_s = 115$ under different δ. Note the dashes with matching colors represent spatially averaged values for respective time-averaged flow rate gains while the mean axial positions of every valve for a given case are marked with crosses. Finally, the alternating valve spacing is repeated twice throughout the domain, thus placing four valves with two smaller and two longer inter-valve spacings in the model.

Clearly, a more distributed backflow reduction by at least one of the valves brings about a more effective backflow reduction overall, as noted by the increased minimum ΔQ_{for} and ΔQ_{back} compared to the uniformly spaced, synchronously deforming counterpart at $\delta = 1$. Considering that the maximum flow rate gain does not vary much between different δ, this brings up the average flow rate gain significantly overall. However, the existence of less extensive gain peaks and dips highlight the limitation of alternate valve spacing. The smaller dips of ΔQ_{for} near the second and fourth valves from the left, highlighted by crosses on Figure 5.12a, indicate that forward flow loss is smaller under these dips. But the smaller peaks of ΔQ_{back} at the same valves on Figure 5.12b show that pumping improvement from backflow reduction is limited by these valves.

5.5.2 Pumping parameter variation

As seen in previous sections, alternating inter-valve spacing produces more effective backflow reduction compared to uniformly-spaced, synchronous valve deformation. However, when compared to uniformly-space, asynchronous valve deformation in Section 5.3, the alternating inter-valve spacing is limited in its pumping performance. To further analyze the effects of two valve placement regimes, pumping parameters of flow rate, work done by the vessel, and pumping efficiency are also plotted against the degree of nonuniform valve placement δ on Figure 5.13. Note that like in previous figures, efficiency for $\Delta P = 0$ is not plotted since the efficiency would be 0 based on the definition of pumping efficiency.

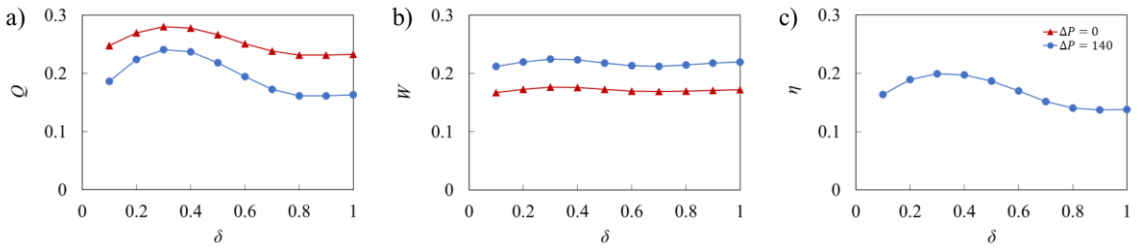

Figure 5.13 a) Flow rate, b) vessel work, and c) pumping efficiency as a function of valve nonuniformity δ for vessels with $\Lambda = 7.5$, $Re = 0.4$, $\phi = 0.25$, $K_b = 88$, and $K_s = 115$.

As mentioned in previous sections, having an alternating inter-valve spacing between consecutive lymphangions increase net flow, peaking around $\delta = 0.3$. This behavior is also consistent when there is no adverse pressure gradient applied, even though the increase in Q is smaller than with adverse pressure gradient. Again, this may be contributed to the decreased importance in backflow prevention since there is more forward flow created by vessel contraction without an applied adverse pressure gradient.

Despite the limited increase in flow rate, having an alternating inter-valve spacing displays a significant advantage in work done by the vessel. Because the number of valves is fixed under different δ, the work done by the vessel stays relatively constant even though flow rate increases and peaks around $\delta = 0.3$. This behavior is starkly different than cases with uniform valve spacing and varying valve number, where cases with decreasing L_{in} and increasing number of valves also have increasing W. The relatively constant W under different δ may have some physiological implication, as analysis from Section 4.6 suggests that lymphatic vessel may contract quickly to generate its maximum work for contraction regardless of operating conditions. Finally, when the flow rates and work done by the vessel are combined together, the pumping efficiency has similar trend as flow rate, peaking around $\delta = 0.3$.

Overall, limitation in number of valves to provide a more effective backflow reduction yields a partial, yet still significant, improvement in flow rate. But with a constant W under different δ suggests that nonuniform valve placement such as alternating inter-valve spacing may operate under comparable or higher pumping efficiency. Furthermore, the relatively constant W under different δ suggests that the analysis of nonuniform valve placement with a fixed number of valves may have a greater implication in actual lymphatic operation considering that the actual lymphatic system may exhibit a similar W.

CHAPTER 6. LYMPHATIC FILARIAL WORM MODEL

6.1 Introduction

This chapter investigates the final objective, which is the behavior of lymphatic filarial worm within lymphatic system. This chapter specifically focuses on filarial worm's interaction with lymphatic valve and how the interaction affects worm's migration under applied flow condition. A model of a filarial worm is newly this developed and integrated into the existing model of a vessel and a valve. For this chapter, a model with rigid vessel wall is used to focus on the interaction between valve and the filarial worm without considering the additional factors from vessel contraction.

6.1.1 Overview of lymphatic filariasis

Lymphatic filariasis is a debilitating condition of the lymphatic system and is a concerning public health issue affecting over one hundred million people worldwide, mostly in tropical regions [36, 37]. Lymphatic filariasis is caused by two parasitic filarial worm species, *W. bancrofti* and *B. malayi*, where *W. bancrofti* makes up about 90% of the total infection worldwide [37]. These filarial worms live in both mosquitoes and humans, but a part of worm's larval stage, adult life, reproduction, and death take place in human hosts. Once entered a human host via a mosquito bite, these worms specifically target the lymphatic system as their nests, where they can live over a decade [35].

During their lifecycle, adult filarial worms' residence and death in lymphatic vessels cause obstruction in lymph flow, causing symptomatic infection and impairment of lymph transport in some of the infected hosts. If left untreated, the repeated obstruction of

adult and dead worms can bring about lymphedema and sometimes hydrocele or limb elephantiasis [35].

Despite the pervasiveness and seriousness of filariasis, many aspects like the infective stage of the filariasis remain unknown. For example, there is little study done on understanding the migratory behavior of filarial larvae in its infective L3 stage, where the larval worms can arrive at specific regions of within the host body. Through computational modelling, this chapter aims to explore a part of this migratory behavior in a mechanical perspective and aims to understand how different conditions within the lymphatic system may aid or hinder the worm's migratory behavior.

6.2 Thrashing worm model

The filarial worm is modelled as a long hexagonal rod with high aspect ratio, where the worm aspect ratio AR_w is defined as the ratio between worm length l_{worm} and the span of worm cross section d_{worm}. For our work, AR_w is set between 45 and 100, which covers initial infective larval stage L3 to approximately a later larval stage of L4 [47, 48]. However, most of the cases tested had $AR_w = 100$, placing the worm simulated in later L3 to L4 larval stage. Finally, the mean diameter of the lymphatic vessel is set around $10d_{worm}$, which places the mean diameter of the vessel around $300{\sim}500\mu m$ based on the experimentally reported values of filarial worm width during the L3 and L4 larval stages [47, 48].

The geometry of the worm and its mechanism for movement are shown below in Figure 6.1. The thrashing of worm is created based on the locomotion models of filarial worm's well-studied nematode cousin *C. elegans* [43-46].

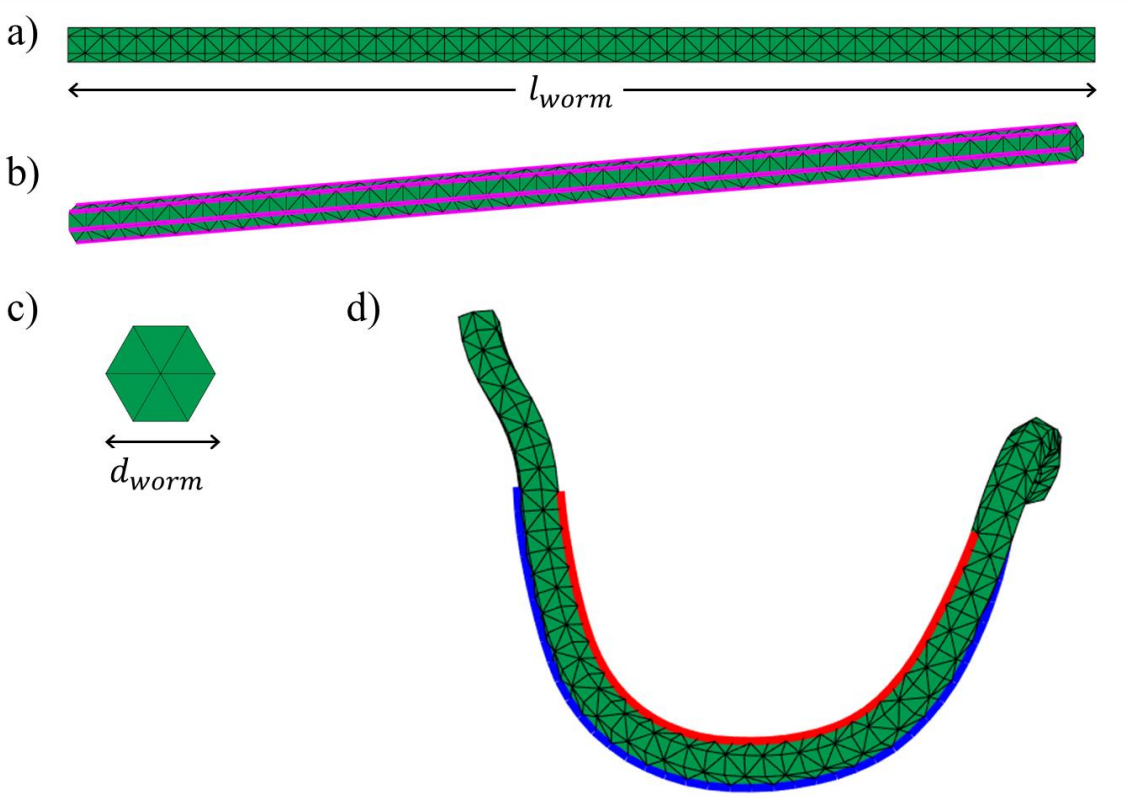

Figure 6.1 Geometry of filarial worm under its initial, undeformed state and during thrashing. a) Undeformed geometry of a filarial worm model showing its length l_{worm}. b) Sides of a filarial worm highlighted in pink. Note that there are six sides in a worm model due to its hexagonal cross section. c) Undeformed geometry of a filarial worm model showing its span d_{worm}. d) Filarial worm during thrashing. The thrashing occurs by ipsilateral contraction and expansion of the two opposite sides of the worm. The red line in the figure highlights applied contraction by changing the equilibrium length of each LSM bond uniformly while the expansion with same strength occurs on the opposite side by expanding the LSM bond's equilibrium length. Note that contraction and expansion do not need to occur through the entire length of the worm's side.

As seen in Figure 6.1b, the model of a filarial worm is split into six distinct sides due to its hexagonal cross section. Deformation that drives worm thrashing occurs only at bonds along a side. As seen in Figure 6.1d, the deformation occurs as a pair of contraction and expansion highlighted in red and blue, respectively. The contraction and expansion occur through a variation of equilibrium length of each LSM bond along the respective

side within the region of contraction/expansion, leading to a creation of contraction/expansion force on a stretching spring that connects two LSM nodes. Also seen in Figure 6.1, the contraction and expansion do not need to occur along the entire length of the side, as long as each contraction and expansion occurs at the same strength per bond while the affected LSM bond must correspondingly has an opposite deformation occurring on the respective LSM bond on the opposite side.

6.2.1 Nondimensional number and simulation parameters

The strength of each contraction/expansion pair is defined as $S = l_{new}/l_0$, where l_{new} is the new equilibrium length of a given LSM bond, and l_0 is the undeformed equilibrium length of a given LSM bond. If $S > 1$, then an LSM bond experiences expansion force compared to its undeformed state, while $S < 1$ induces contraction. The contraction strength is greater for lower values of S while expansion strength is greater for higher values of S. Despite a deformation created, this force application keeps total force and moment created internally by the contraction/expansion pair equal to zero. This is because the two LSM nodes that an LSM bond connects experience force in equal and opposite direction due to any contraction or expansion. Furthermore, because forces are only created in the direction of the LSM bond, there is no rotational force created either.

The strength of each contraction/expansion pair are applied in probability with Gaussian distribution. The mean value of this distribution determines the strength of thrashing, referred to as S_{mean} and will be used interchangeably with S hereafter. The expansion/contraction regularly at a frequency f_{cont} and is normalized as a $Wo_{worm} = d_{worm}\sqrt{2\pi f_{cont}\rho/\mu}$. Note that density ρ denote that of surrounding fluid, not of worm.

Morse potential-based repulsion between nodes of the model is implemented to prevent crossing of different bodies within the model. Elastic properties of valves such as bending and in-plane stiffness are defined with the same definitions as previous chapters. Elastic properties of worm are noted with an additional subscript of worm and are defined with modified variables than what was used for valves in a rigid vessel model. The bending stiffness is normalized as $K_{b,r,worm} = 160k_{b,worm}/\sqrt{3}\pi d_{worm}^3 \Delta P_{app}$, and in-plane stiffness is defined as $K_{s,r,worm} = k_{s,worm}/\Delta P_{app} d_{worm}$.

Finally, unlike *C. elegans* which produces undulation for self-propulsion, lymphatic filarial worm is reported to have little or no ability to propel by itself [39]. The worm model's thrashing parameters are adjusted to ensure this by randomly selecting elements such as contraction strength, side of contraction in a worm, and region of contraction within a worm.

6.3 Migration of filarial worm in a rigid vessel

Inspection of the filarial worm's behavior and interaction with the surrounding environment will focus on two aspects: variation under different thrashing strength S_{mean} and change in worm kinematics when interacting with valves. The worm is first inspected visually to identify notable changes. Then, worm's motion is further analyzed through variables such as mean axial position of worm over time.

6.3.1 General worm behavior under oscillating pressure difference

Profile of filarial worm inside a rigid vessel with a lymphatic valve under applied oscillating pressure difference is shown below as Figure 6.2. Some relevant parameters are

$Re_r = 1.2$, $Wo = 0.4$, $K_{s,r} = 0.04$, $K_{s,r,worm} = 1.6$, $K_{b,r} = 0.1$, $K_{b,r,worm} = 0.1$, $S_{mean} = 0.4$, and $Wo_{worm} = 0.5$. Note that initial geometry of filarial worm is contracted by applying contraction/expansion to a random side pair with S_{mean} until the geometry no longer changes. This is done to ensure that the filarial worm starts inside the lymphatic vessel while not stretched out to interfere with the lymphatic valve.

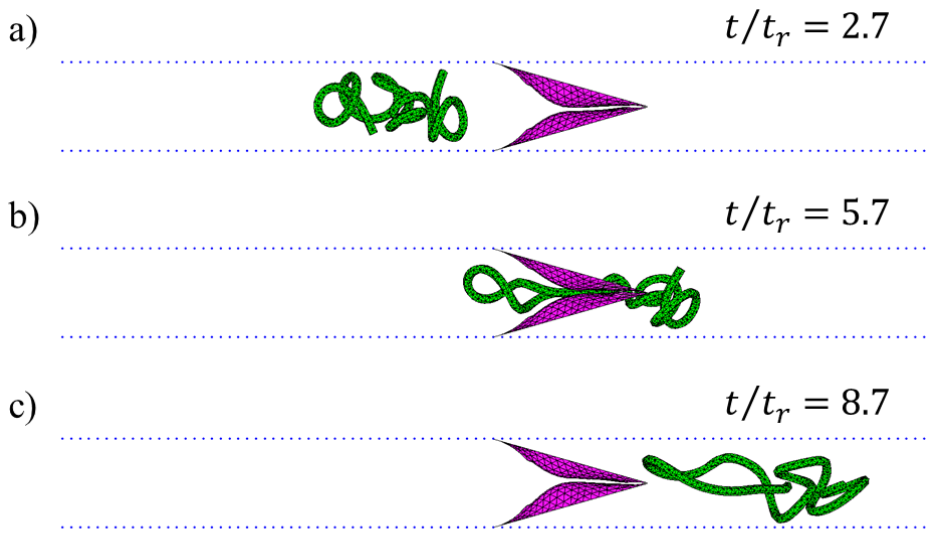

Figure 6.2 Filarial worm, valve, and vessel profile noted in green, magenta, and blue, respectively, under different time. The simulation parameters are $Re_r = 1.2$, $Wo = 0.4$, $K_{s,r} = 0.04$, $K_{s,r,worm} = 1.6$, $K_{b,r} = 0.1$, $K_{b,r,worm} = 0.1$, $S_{mean} = 0.4$, and $Wo_{worm} = 0.5$.

As expected, the most change in worm's geometry occurs when the filarial worm interacts with the lymphatic valves even though random contraction is still applied before the worm meets the valve. Compared to the coiled status of the worm before interaction, the valve forces the worm to be straighter, while the valve leaflets also experience minor extra deformation due to the worm's passing. After its interaction with the valve, the worm again remains unchanged in its shape. From visual inspection, the filarial worm's migration

is heavily influenced by applied flow condition and interaction with lymphatic valves. Furthermore, the lymphatic valve's interaction with worm may have some disruptive effect on overall flow as well although the disruption may be minor and brief during the worm's passage through the valve.

To see the effect of different S_{mean}, the profile of worm, valve, and vessel are plotted for $S_{mean} = 0.6$ below at Figure 6.3. All other simulation parameters are equal to that of Figure 6.2.

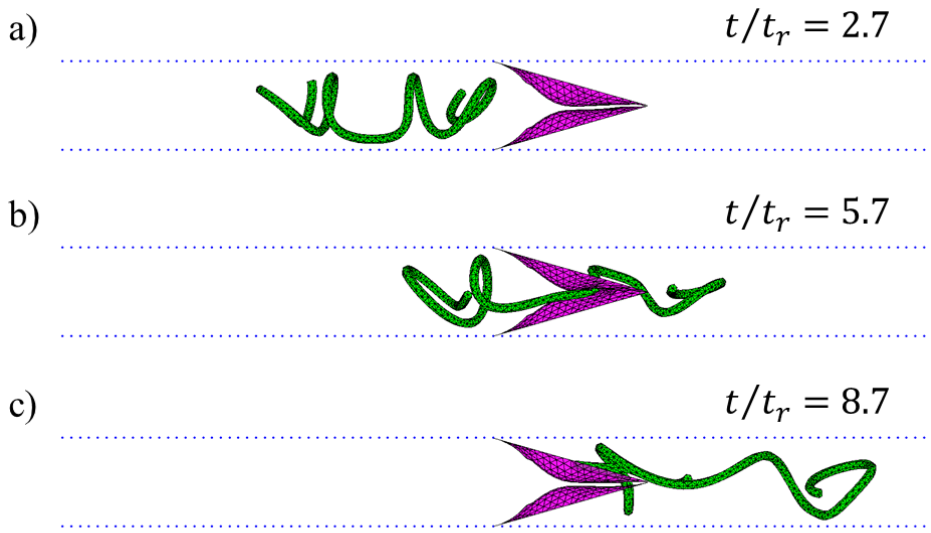

Figure 6.3 Filarial worm, valve, and vessel profile noted in green, magenta, and blue, respectively, under different time. The simulation parameters are $Re_r = 1.2$, $Wo = 0.4$, $K_{s,r} = 0.04$, $K_{s,r,worm} = 1.6$, $K_{b,r} = 0.1$, $K_{b,r,worm} = 0.1$, $S_{mean} = 0.6$, and $Wo_{worm} = 0.5$.

Like in the previous case with $S_{mean} = 0.4$, the filarial worm's own thrashing has a limited effect on overall shape until the worm starts to interact with the valve. However, interaction with the valve has a less noticeable effect for the worm in Figure 6.3. Even though the worm starts with a looser curl, the valve flattens and straightens the worm much

like in Figure 6.2. But once through the valve, the filarial worm recovers much less curl compared to its counterpart under $S_{mean} = 0.4$. This indicates that filarial worm with different thrashing strengths such as dead worms or worms under different larval stages may navigate through the lymphatic system differently.

6.3.2 Filarial worm kinematics, position and displacement

Although the visual inspection of worm profile in relation to lymphatic valve deformation provided some insights into worm migration, more analysis is conducted to quantifiably identify changes in worm movement under different phases of the flow and under different thrashing strengths. First, the axial position of the centroid of the worm is plotted over time under different thrashing strengths and is shown at Figure 6.4. Note the simulation parameters are the same as in Figure 6.2 and Figure 6.3, and thrashing strengths are noted separately with differently colored lines.

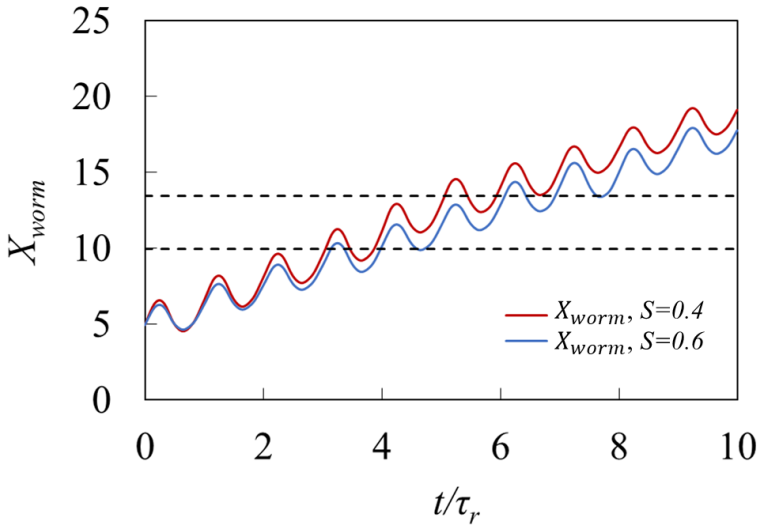

Figure 6.4 Filarial worm's normalized axial position of centroid over time under two different thrashing strengths. Note the horizontal dashes indicate the limits of axial position of the lymphatic valve.

Overall, the filarial worm has a net forward movement but with some oscillation. This behavior can be attributed to the oscillatory nature of the flow within the model, which is caused by the delay in valve response to changes in pressure difference. This means that from onset of backflow from pressure difference to valve occlusion, there will be some backflow, causing the worm to go back slightly. However, like the overall flow pumping, the net positive pumping in flow occurs, translating to an overall migration of the worm. As expected, the worm's movement is highly dominated by the surrounding flow pattern. However, we can see some diversion occurring between cases with different thrashing strengths, especially when the worm reaches the valves noted in black dashed lines. This again supports the analysis from previous section on interference in worm's migration by the lymphatic valve and its possibly varying effect depending on worm's thrashing strengths.

Although Figure 6.4 shows some interesting aspects of worm migration, the profile is dominated by the oscillating worm movement which masks the effect of interaction between the worm and the valve. To view this aspect more closely, a displacement of period-averaged axial position worm's centroid is plotted over time in Figure 6.5. By averaging the centroid axial position over a pumping period τ_r and plotting the axial position gain of the period-averaged centroid's axial position, this plot can more clearly show how the worm's movement changes near and through the valve.

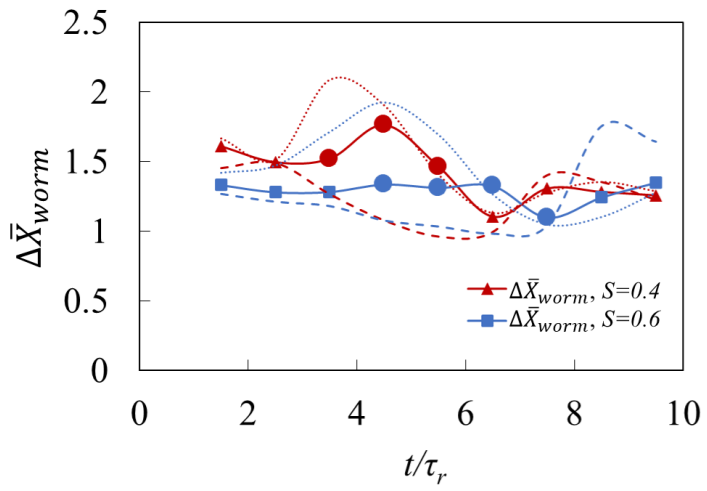

Figure 6.5 Period-averaged axial displacement of filarial worm's normalized centroid over time. Note that dashed lines indicate period-averaged displacement of minimum axial position of the worm while dotted lines indicate the period-averaged displacement of maximum axial position. If a centroid of the filarial worm is within the axial limits of the valve, the corresponding ranges in time are highlighted in circles.

First, we can see that the case with higher thrashing strength, noted in lower S value, has a higher axial displacement even before the interaction with lymphatic valve. This may be attributed to the greater degree of worm's proximity to the centerline of the vessel, which has a higher velocity. As noted in filled circles, worm with higher trashing strength further increases its speed by having a greater gain in displacement per consecutive pumping period when the worm interacts with the valve. As a result of that, the worm with $S = 0.4$ interacts with the valve for a shorter period of time, noted in $t/t_r \sim 3$ of interaction time with the valve. In comparison, worm with lower thrashing strength not only has unnoticeable increase in movement when it goes through the valve, but the time that the worm stays near the valve also increases to $t/t_r \sim 4$. This difference occurs even though both worms experience a significant "straightening" as it tries to pass through the valve's opening. This "straightening" can be seen from the increase in difference between period-

averaged maximum axial position of the worm, plotted in dotted lines, and period-averaged minimum axial position of the worm, plotted in dashed lines. In both thrashing strengths, the difference in axial positions of the worm's extremes drastically increase as the worm interacts with the valve.

Once much of the worm passes through the valve, both worms experience a brief decline in axial displacement. Then, the reversal in displacement of the maximum and minimum worm positions occur (referred also as front and back hereafter), making the axial displacement of the worm's back greater than its front and essentially shrinking the worm axially. This can be attributed to the delay flow the front and back of the worm experience, especially once the worm is axially stretched by the valve. As seen in Figure 6.3b and c, the front of the worm may be at the similar position as the back of the worm $3\tau_r$ before, making the displacement comparable to that of the front 3 cycles before. Eventually, when even the back of the worm is free from flow disturbance by the valve, the worm gradually recovers to its pre-valve profile. Overall, we can see that the valve's deformation and flow disruption affect worms with greater thrashing strength more.

6.3.3 Filarial worm velocity and flow velocity

Finally, the worm's movement is analyzed again in terms of the worm's mean axial velocity and its impact on the lymphatic flow by examining the average flow velocity per pumping cycle. The plot of both velocities is shown below at Figure 6.6.

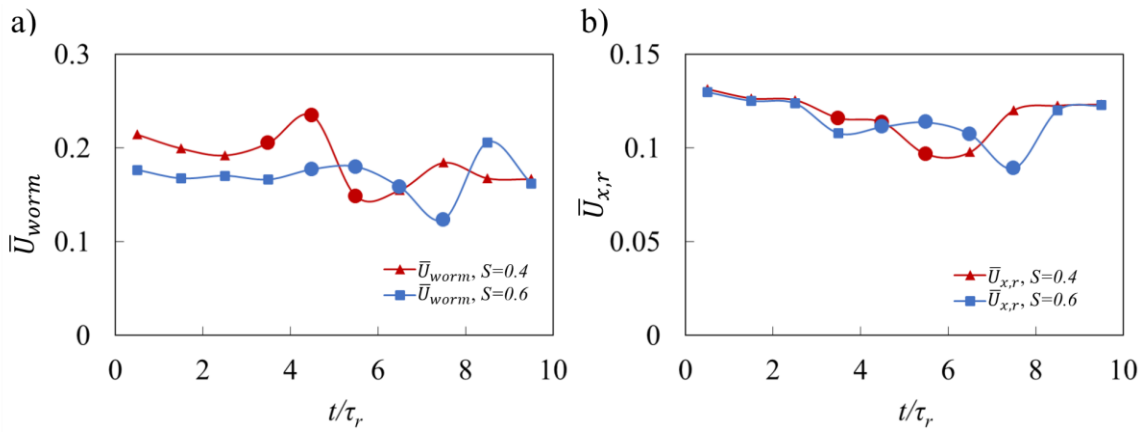

Figure 6.6 a) Period-averaged normalized axial velocity of filarial worm over time under different thrashing strengths. If a centroid of the filarial worm is within the axial limits of the valve, the corresponding ranges in time are highlighted in circles. b) Period-averaged normalized mean axial fluid velocity over time under different thrashing strengths. If a centroid of the filarial worm is within the axial limits of the valve, the corresponding ranges in time are highlighted in circles.

As demonstrated in Figure 6.5, the period-averaged velocities of the worm in both thrashing strengths show increase as the worm starts to interact with the valve. This may be attributed to the decreased cross-sectional area due to the valve, thus increasing the flow speed and worm axial velocity near the valve opening as the flow approaches from the forward direction. Once the worm and flow pass through the valve opening, the sudden, wider cross section of the vessel briefly decreases the flow velocity, thus decreasing the worm velocity as well. Eventually, the flow and worm's axial velocities recover to the value before interacting with the valve. Like in Figure 6.5, relatively unchanged axial velocity can be seen for $S = 0.6$, again highlighting the behavioral difference in worms with varying thrashing strengths.

The worm's interaction with the valve has a temporary yet noticeable effect on overall flow of the model. This can be noted in both thrashing strength and especially strong

at the end of the worm's interaction with the valve, noted in a dip in period-averaged flow velocity under a rigid vessel model, $\overline{U}_{x,r}$. This drop in velocity can be attributed to the worm's passage through the valve opening, blocking forward flow and allowing more backflow from incomplete valve closure.

CHAPTER 7. CONCLUDING REMARKS

7.1 Scientific contributions

The overarching objective and contribution of this thesis is the implementation of fully coupled 3D fluid-structure interaction model in the lymphatic system. This model specifically focused on the collecting lymphatics and its flexible valves' effect on flow, as there is very little study done about the lymphatic valves. By utilizing a combination of lattice-Boltzmann and lattice spring models, complex geometries like the lymphatic valves can be easily integrated into parallel high-performance computing with good computational speed, which is well suited for studies like the lymphatic system that requires multiple simulations of the model under a wide variety of parameters.

The focus and findings of this thesis can be divided into three main areas: lymphatic valves, lymphatic valve and vessel under vessel contraction, and incorporation of filarial worm into the lymphatic system model. First, the lymphatic model utilized a rigid vessel with flexible lymphatic valves and the role and importance of lymphatic valves were investigated under various valve and flow conditions, leading to a journal publication [49]. The model had a rigid vessel unlike its physiological counterpart because it was necessary to focus specifically on the role lymphatic valves. Under unidirectionally applied flow, our study showed that shorter and more flexible valves reduce flow resistance from the valves, thus facilitate a better pumping. However, very short valves cannot properly prevent backflow, meaning that there exists some critical range of aspect ratio AR_{cr} where the flow is optimized. When flow varied as a function of time, our study demonstrated that there is a delay in valve response under changing flow condition computationally supporting the

experimental observation of valve hysteresis. When time-dependent flow was applied under different valve aspect ratio (or length), optimal aspect ratios with maximum net pumping were found, supporting the findings from our unidirectional flow study. Finally, the valve resistances were calculated under different valve properties and pressure difference applied and showed that existing model of the lymphatic valve resistance may be improved by providing a more pinpointed valve resistance under different properties of the valve.

The second objective of the thesis led to a creation of a lymphatic model with a contracting vessel based on peristaltic contraction, thus more closely resembling the conditions and geometries of the actual lymphatic system. This objective also led to a publication that is currently in press [115]. Instead of driven by an applied flow condition, vessel contraction like the lymphatic muscle contraction powered the flow while adverse pressure gradient is applied. Prescribed peristaltic contraction is implemented as a good baseline for valve-less behavior as there have been extensive work done on peristaltic pumping in general. General study of flow and centerline velocity showed that lymphatic pumping achieves its benefit from its valveless counterparts through prevention of backflow. The degree of effective backflow prevention varies by many factors such as speed and wavelength of contraction wave, amplitude of contraction of the vessel, applied adverse pressure gradient, elastic properties of the valve, and inter-valve spacing. Under all valve and vessel conditions investigated, optimal conditions with maximum flow efficiency existed, demonstrating the complex relation that lymphatic valves and vessels have on effective pumping. Notably, valve bending stiffness had optimal condition for flow rate as well, demonstrating that extremely flexible valves occlude properly to prevent

backflow. Different inter-valve spacing also indicated that backflow prevention and lymphatic pumping may not be as effective if applied vessel contraction leads to synchronous deformation on multiple valves, as these overlapped occlusion across multiple valves do not provide proportionally increased backflow prevention. Finally, an incorporation of experimentally reported vessel contraction amplitude as a function of applied pressure gradient suggested that lymphatic vessels may rapidly apply its maximum work regardless of the adverse pressure gradient.

The final objective incorporated the model of a lymphatic filarial worm into the existing lymphatic model. Although greater investigation is needed, studies on lymphatic filariasis during its infective migratory phase is extremely limited, and a computational model of that stage is almost non-existent to our knowledge. Often neglected within the neglected tropical condition of lymphatic filariasis, the combined model of a filarial worm and the simplified lymphatic system showed that filarial worm and lymphatic valve may interact differently under different worm parameters such as worm's thrashing strength. Furthermore, the filarial worm's interference to proper valve occlusion may lead to temporary reduction in pumping capacity when the worm flows through the valve.

7.2 Future works

Despite the numerous aspects of the lymphatic valve and vessel this thesis explored, there are still many more aspects unexplored in this thesis. Some of the potential avenues for future work are listed below.

1. **Incorporation of valve resistance model into lumped parameter models:** Although a model of valve resistance under different valve and vessel

conditions are created, incorporation of this mode into the lumped parameter model is still needed. Combining the results from our model with the lumped parameter model brings in the advantages of two models by allowing high speed calculation of a long chain of lymphangions while incorporating more detailed model of valve resistance.

2. **Further investigation of flow response under vessel contraction**: Due to a large range of parameters to be investigated, many parameters were necessarily unexplored or relied on studies under a rigid vessel model. Valve aspect ratio is an important example of this. Although analyzed extensively under a rigid vessel model, analysis of valve response under different bending stiffness in a contracting vessel indicates that more complex relationship may exist between valve geometric properties and flow response. Interaction between different solid components within the model may also need further investigation, as interactions like adhesion may lead to different valve response under changing flow condition from a fully closed state.
3. **Nonuniform vessel contraction**: Although the peristaltic contraction of the lymphatic vessel is a good representation, physiological lymphatic vessels experience less uniform and less sinusoidal contraction while the contraction itself can travel bi-directionally [95]. These nonuniform contractions also produce retrograde contraction where the contraction wave travels against the valve opening, while contractions and flow near lymphatic junctions may bring an additional complexity.

4. **Shear stress-sensitive vessel contraction**: Although our work explored flow under different contraction amplitudes based on adverse pressure gradient, other factors that affect vessel contraction such as shear stress has not been explored [96, 97]. This means that coupling of vessel contraction to flow condition may be needed for more physiological representation of vessel contraction. Eventually, vessel contraction not prescribed but driven by a well-studied lymphatic muscular contraction model can be incorporated to provide full representation of physiological vessel contraction.
5. **Diversification of valve spacing**: The current model utilizes three major valve placement schemes: synchronous and uniformly spaced valves, asynchronous and uniformly spaced valves, and asynchronous and nonuniformly spaced valves. Even though our model covers many valve configurations, a greater inspection of valve placement of the actual lymphatic system may be needed. By doing so, a more physiological valve placement pattern can be found and incorporated into the existing model.
6. **Further investigation of filarial worm migration behavior in the lymphatic system**: Although the computational investigation of filarial worm migration itself is notable due to its rarity, the model is at its early stage mainly due to many unknown parameters from limited experimental studies on filarial worm migration pattern. Further studies of filarial worm under more diverse thrashing patterns, wider lymphatic valve and vessel parameters, and diverse navigational challenges are needed.

REFERENCES

1. Dixon, J.B., *Lymphatic lipid transport: sewer or subway?* Trends in Endocrinology & Metabolism, 2010. **21**(8): p. 480-487.

2. Swartz, M.A., *The physiology of the lymphatic system.* Advanced drug delivery reviews, 2001. **50**(1-2): p. 3-20.

3. Ikomi, F. and G. Schmid-Schonbein, *Lymph pump mechanics in the rabbit hind leg.* American Journal of Physiology-Heart and Circulatory Physiology, 1996. **271**(1): p. H173-H183.

4. McGeown, J., N. McHale, and K. Thornbury, *Arterial pulsation and lymph formation in an isolated sheep hindlimb preparation.* The Journal of physiology, 1988. **405**(1): p. 595-604.

5. Reddy, N.P., V. Palmieri, and G. Cochran, *Subcutaneous interstitial fluid pressure during external loading.* American Journal of Physiology-Regulatory, Integrative and Comparative Physiology, 1981. **240**(5): p. R327-R329.

6. Skalak, T., G. Schmid-Schönbein, and B. Zweifach, *New morphological evidence for a mechanism of lymph formation in skeletal muscle.* Microvascular research, 1984. **28**(1): p. 95-112.

7. Webb Jr, R.C. and T. Starzl, *The effect of blood vessel pulsations on lymph pressure in large lymphatics.* Bulletin of the Johns Hopkins Hospital, 1953. **93**(6): p. 401.

8. Davis, M.J., E. Rahbar, A.A. Gashev, D.C. Zawieja, and J.E. Moore, *Determinants of valve gating in collecting lymphatic vessels from rat mesentery.* American Journal of Physiology-Heart and Circulatory Physiology, 2011. **301**(1): p. H48-H60.

9. Quick, C.M., A.M. Venugopal, A.A. Gashev, D.C. Zawieja, and R.H. Stewart, *Intrinsic pump-conduit behavior of lymphangions.* American Journal of Physiology-Regulatory, Integrative and Comparative Physiology, 2007. **292**(4): p. R1510-R1518.

10. Zawieja, D.C., *Contractile physiology of lymphatics.* Lymphatic research and biology, 2009. **7**(2): p. 87-96.

11. Tian, W., S.G. Rockson, X. Jiang, J. Kim, A. Begaye, E.M. Shuffle, A.B. Tu, M. Cribb, Z. Nepiyushchikh, and A.H. Feroze, *Leukotriene B4 antagonism*

ameliorates experimental lymphedema. Science translational medicine, 2017. **9**(389): p. eaal3920.

12. Gary, D.E., *Lymphedema diagnosis and management.* Journal of the American Academy of Nurse Practitioners, 2007. **19**(2): p. 72-78.

13. Brouillard, P., L. Boon, and M. Vikkula, *Genetics of lymphatic anomalies.* The Journal of clinical investigation, 2014. **124**(3): p. 898-904.

14. Davis, M.J., J.P. Scallan, J.H. Wolpers, M. Muthuchamy, A.A. Gashev, and D.C. Zawieja, *Intrinsic increase in lymphangion muscle contractility in response to elevated afterload.* American Journal of Physiology-Heart and Circulatory Physiology, 2012. **303**(7): p. H795-H808.

15. Eisenhoffer, J., A. Kagal, T. Klein, and M. Johnston, *Importance of valves and lymphangion contractions in determining pressure gradients in isolated lymphatics exposed to elevations in outflow pressure.* Microvascular research, 1995. **49**(1): p. 97-110.

16. Lapinski, P.E., B.A. Lubeck, D. Chen, A. Doosti, S.D. Zawieja, M.J. Davis, and P.D. King, *RASA1 regulates the function of lymphatic vessel valves in mice.* The Journal of clinical investigation, 2017. **127**(7): p. 2569-2585.

17. Petrova, T.V., T. Karpanen, C. Norrmén, R. Mellor, T. Tamakoshi, D. Finegold, R. Ferrell, D. Kerjaschki, P. Mortimer, and S. Ylä-Herttuala, *Defective valves and abnormal mural cell recruitment underlie lymphatic vascular failure in lymphedema distichiasis.* Nature medicine, 2004. **10**(9): p. 974.

18. Sabine, A., E. Bovay, C.S. Demir, W. Kimura, M. Jaquet, Y. Agalarov, N. Zangger, J.P. Scallan, W. Graber, and E. Gulpinar, *FOXC2 and fluid shear stress stabilize postnatal lymphatic vasculature.* The Journal of clinical investigation, 2015. **125**(10): p. 3861-3877.

19. MacDonald, A.J., K.P. Arkill, G.R. Tabor, N.G. McHale, and C.P. Winlove, *Modeling flow in collecting lymphatic vessels: one-dimensional flow through a series of contractile elements.* American Journal of Physiology-Heart and Circulatory Physiology, 2008. **295**(1): p. H305-H313.

20. Pan, W.R., C.M. le Roux, and S.M. Levy, *Alternative lymphatic drainage routes from the lateral heel to the inguinal lymph nodes: anatomic study and clinical implications.* ANZ journal of surgery, 2011. **81**(6): p. 431-435.

21. Wilson, J.T., R. van Loon, W. Wang, D.C. Zawieja, and J.E. Moore, *Determining the combined effect of the lymphatic valve leaflets and sinus on resistance to forward flow.* Journal of biomechanics, 2015. **48**(13): p. 3584-3590.

22. Dixon, J.B., S.T. Greiner, A.A. Gashev, G.L. Cote, J.E. Moore, and D.C. Zawieja, *Lymph flow, shear stress, and lymphocyte velocity in rat mesenteric prenodal lymphatics.* Microcirculation, 2006. **13**(7): p. 597-610.

23. Moore, J.E. and C.D. Bertram, *Lymphatic system flows.* Annual review of fluid mechanics, 2018. **50**: p. 459-482.

24. Baish, J.W., C. Kunert, T.P. Padera, and L.L. Munn, *Synchronization and random triggering of lymphatic vessel contractions.* PLoS computational biology, 2016. **12**(12): p. e1005231.

25. Bertram, C., C. Macaskill, M. Davis, and J. Moore, *Development of a model of a multi-lymphangion lymphatic vessel incorporating realistic and measured parameter values.* Biomechanics and modeling in mechanobiology, 2014. **13**(2): p. 401-416.

26. Bertram, C., C. Macaskill, and J. Moore, *Simulation of a chain of collapsible contracting lymphangions with progressive valve closure.* Journal of biomechanical engineering, 2011. **133**(1): p. 011008.

27. Bertram, C., C. Macaskill, and J. Moore, *Incorporating measured valve properties into a numerical model of a lymphatic vessel.* Computer methods in biomechanics and biomedical engineering, 2014. **17**(14): p. 1519-1534.

28. Bertram, C.D., C. Macaskill, M.J. Davis, and J.E. Moore, *Consequences of intravascular lymphatic valve properties: a study of contraction timing in a multi-lymphangion model.* American Journal of Physiology-Heart and Circulatory Physiology, 2016. **310**(7): p. H847-H860.

29. Jamalian, S., C.D. Bertram, W.J. Richardson, and J.E. Moore, *Parameter sensitivity analysis of a lumped-parameter model of a chain of lymphangions in series.* American Journal of Physiology-Heart and Circulatory Physiology, 2013. **305**(12): p. H1709-H1717.

30. Jamalian, S., M.J. Davis, D.C. Zawieja, and J.E. Moore, *Network scale modeling of lymph transport and its effective pumping parameters.* PloS one, 2016. **11**(2): p. e0148384.

31. Razavi, M.S., T.S. Nelson, Z. Nepiyushchikh, R.L. Gleason, and J.B. Dixon, *The relationship between lymphangion chain length and maximum pressure generation established through in vivo imaging and computational modeling.* American Journal of Physiology-Heart and Circulatory Physiology, 2017. **313**(6): p. H1249-H1260.

32. Reddy, N.P., T.A. Krouskop, and P.H. Newell Jr, *A computer model of the lymphatic system.* Computers in biology and medicine, 1977. **7**(3): p. 181-197.

33. Kunert, C., J.W. Baish, S. Liao, T.P. Padera, and L.L. Munn, *Mechanobiological oscillators control lymph flow.* Proceedings of the National Academy of Sciences, 2015. **112**(35): p. 10938-10943.

34. Rahbar, E. and J.E. Moore, *A model of a radially expanding and contracting lymphangion.* Journal of biomechanics, 2011. **44**(6): p. 1001-1007.

35. Kilarski, W.W., C. Martin, M. Pisano, O. Bain, S.A. Babayan, and M.A. Swartz, *Inherent biomechanical traits enable infective filariae to disseminate through collecting lymphatic vessels.* Nature communications, 2019. **10**(1): p. 1-14.

36. Chakraborty, S., M. Gurusamy, D.C. Zawieja, and M. Muthuchamy, *Lymphatic filariasis: perspectives on lymphatic remodeling and contractile dysfunction in filarial disease pathogenesis.* Microcirculation, 2013. **20**(5): p. 349-364.

37. Taylor, M.J., A. Hoerauf, and M. Bockarie, *Lymphatic filariasis and onchocerciasis.* The Lancet, 2010. **376**(9747): p. 1175-1185.

38. Babayan, S.A., T. Attout, A. Harris, M.D. Taylor, L. Le Goff, P.N. Vuong, L. Rénia, J.E. Allen, and O. Bain, *Vaccination against filarial nematodes with irradiated larvae provides long-term protection against the third larval stage but not against subsequent life cycle stages.* International journal for parasitology, 2006. **36**(8): p. 903-914.

39. Kassis, T., H.M. Skelton, I.M. Lu, A.R. Moorhead, and J.B. Dixon, *An integrated in vitro imaging platform for characterizing filarial parasite behavior within a multicellular microenvironment.* PLoS neglected tropical diseases, 2014. **8**(11): p. e3305.

40. Myburgh, E., R. Ritchie, A. Goundry, K. O'Neill, F. Marchesi, and E. Devaney, *Attempts to image the early inflammatory response during infection with the lymphatic filarial nematode Brugia pahangi in a mouse model.* Plos one, 2016. **11**(12): p. e0168602.

41. Sukhdeo, M. and S. Sukhdeo, *Optimal habitat selection by helminths within the host environment.* Parasitology, 1994. **109**(S1): p. S41-S55.

42. Sukhdeo, M.V. and A.D. Bansemir, *Critical resources that influence habitat selection decisions by gastrointestinal helminth parasites.* International Journal for Parasitology, 1996. **26**(5): p. 483-498.

43. Fang-Yen, C., M. Wyart, J. Xie, R. Kawai, T. Kodger, S. Chen, Q. Wen, and A.D. Samuel, *Biomechanical analysis of gait adaptation in the nematode Caenorhabditis elegans.* Proceedings of the National Academy of Sciences, 2010. **107**(47): p. 20323-20328.

44. Gjorgjieva, J., D. Biron, and G. Haspel, *Neurobiology of Caenorhabditis elegans locomotion: where do we stand?* Bioscience, 2014. **64**(6): p. 476-486.

45. Mailler, R., J. Avery, J. Graves, and N. Willy. *A biologically accurate 3d model of the locomotion of caenorhabditis elegans*. in *2010 International Conference on Biosciences*. 2010. IEEE.

46. Niebur, E. and P. Erdös, *Theory of the locomotion of nematodes: dynamics of undulatory progression on a surface.* Biophysical journal, 1991. **60**(5): p. 1132-1146.

47. Mutafchiev, Y., O. Bain, Z. Williams, J.W. McCall, and M.L. Michalski, *Intraperitoneal development of the filarial nematode Brugia malayi in the Mongolian jird (Meriones unguiculatus).* Parasitology research, 2014. **113**(5): p. 1827-1835.

48. Mak, J., P. Lim, B. Sim, and L. Liew, *Brugia malayi and B. pahangi: cultivation in vitro of infective larvae to the fourth and fifth stages.* Experimental parasitology, 1983. **55**(2): p. 243-248.

49. Ballard, M., K.T. Wolf, Z. Nepiyushchikh, J.B. Dixon, and A. Alexeev, *Probing the effect of morphology on lymphatic valve dynamic function.* Biomechanics and modeling in mechanobiology, 2018. **17**(5): p. 1343-1356.

50. Shapiro, A.H., M.Y. Jaffrin, and S.L. Weinberg, *Peristaltic pumping with long wavelengths at low Reynolds number*. Journal of fluid mechanics, 1969. **37**(4): p. 799-825.

51. Takabatake, S., K. Ayukawa, and A. Mori, *Peristaltic pumping in circular cylindrical tubes: a numerical study of fluid transport and its efficiency.* Journal of Fluid Mechanics, 1988. **193**: p. 267-283.

52. Lu, I., T. Kassis, A. Rogers, A. Schudel, J. Weil, C. Evans, A. Moorhead, S. Thomas, and J. Dixon, *Optimization of culture and analysis methods for enhancing long-term Brugia malayi survival, molting and motility in vitro.* Parasitology Open, 2018. **4**.

53. Alexeev, A., R. Verberg, and A.C. Balazs, *Modeling the motion of microcapsules on compliant polymeric surfaces.* Macromolecules, 2005. **38**(24): p. 10244-10260.

54. Alexeev, A., R. Verberg, and A.C. Balazs, *Designing compliant substrates to regulate the motion of vesicles.* Physical review letters, 2006. **96**(14): p. 148103.

55. Ladd, A. and R. Verberg, *Lattice-Boltzmann simulations of particle-fluid suspensions.* Journal of statistical physics, 2001. **104**(5-6): p. 1191-1251.

56. Succi, S., *The lattice Boltzmann equation: for fluid dynamics and beyond*. 2001: Oxford university press.

57. Freudiger, S., J. Hegewald, and M. Krafczyk, *A parallelisation concept for a multi-physics lattice Boltzmann prototype based on hierarchical grids.* Progress in Computational Fluid Dynamics, an International Journal, 2008. **8**(1-4): p. 168-178.

58. Kandhai, D., A. Koponen, A.G. Hoekstra, M. Kataja, J. Timonen, and P.M. Sloot, *Lattice-Boltzmann hydrodynamics on parallel systems.* Computer Physics Communications, 1998. **111**(1-3): p. 14-26.

59. Satofuka, N. and T. Nishioka, *Parallelization of lattice Boltzmann method for incompressible flow computations.* Computational Mechanics, 1999. **23**(2): p. 164-171.

60. Velivelli, A. and K. Bryden, *Parallel performance and accuracy of lattice Boltzmann and traditional finite difference methods for solving the unsteady two-dimensional Burger's equation.* Physica A: Statistical Mechanics and its Applications, 2006. **362**(1): p. 139-145.

61. Guo, Z., C. Zheng, and B. Shi, *Discrete lattice effects on the forcing term in the lattice Boltzmann method.* Physical review E, 2002. **65**(4): p. 046308.

62. Buxton, G.A., R. Verberg, D. Jasnow, and A.C. Balazs, *Newtonian fluid meets an elastic solid: coupling lattice Boltzmann and lattice-spring models.* Physical Review E, 2005. **71**(5): p. 056707.

63. Ostoja-Starzewski, M., *Lattice models in micromechanics.* Appl. Mech. Rev., 2002. **55**(1): p. 35-60.

64. Buxton, G.A., C.M. Care, and D.J. Cleaver, *A lattice spring model of heterogeneous materials with plasticity.* Modelling and simulation in materials science and engineering, 2001. **9**(6): p. 485.

65. Monette, L. and M. Anderson, *Elastic and fracture properties of the two-dimensional triangular and square lattices.* Modelling and Simulation in Materials Science and Engineering, 1994. **2**(1): p. 53.

66. Mao, W., *Modeling particle suspensions using lattice Boltzmann method*. 2013, Georgia Institute of Technology.

67. Jagla, E., *Modeling the buckling and delamination of thin films.* Physical Review B, 2007. **75**(8): p. 085405.

68. Kim, H., J. Lu, M.S. Sacks, and K.B. Chandran, *Dynamic simulation pericardial bioprosthetic heart valve function.* Journal of biomechanical engineering, 2006. **128**(5): p. 717-724.

69. Sacks, M.S., Z. He, L. Baijens, S. Wanant, P. Shah, H. Sugimoto, and A. Yoganathan, *Surface strains in the anterior leaflet of the functioning mitral valve.* Annals of biomedical engineering, 2002. **30**(10): p. 1281-1290.

70. Sacks, M.S. and A.P. Yoganathan, *Heart valve function: a biomechanical perspective.* Philosophical Transactions of the Royal Society B: Biological Sciences, 2007. **362**(1484): p. 1369-1391.

71. Tuckerman, M., B.J. Berne, and G.J. Martyna, *Reversible multiple time scale molecular dynamics.* The Journal of chemical physics, 1992. **97**(3): p. 1990-2001.

72. Yeh, P.D. and A. Alexeev, *Effect of aspect ratio in free-swimming plunging flexible plates.* Computers & Fluids, 2016. **124**: p. 220-225.

73. Alexeev, A. and A.C. Balazs, *Designing smart systems to selectively entrap and burst microcapsules.* Soft Matter, 2007. **3**(12): p. 1500-1505.

74. Yeh, P.D. and A. Alexeev, *Biomimetic flexible plate actuators are faster and more efficient with a passive attachment.* Acta Mechanica Sinica, 2016. **32**(6): p. 1001-1011.

75. Masoud, H., B.I. Bingham, and A. Alexeev, *Designing maneuverable micro-swimmers actuated by responsive gel.* Soft Matter, 2012. **8**(34): p. 8944-8951.

76. Mao, W.B. and A. Alexeev, *Motion of spheriod particles in shear flow with inertia.* Journal of Fluid Mechanics, 2014. **749**: p. 145-166.

77. Hanasoge, S., M. Ballard, P.J. Hesketh, and A. Alexeev, *Asymmetric motion of magnetically actuated artificial cilia.* Lab on a Chip, 2017. **17**(18): p. 3138-3145.

78. Buxton, G.A. and N. Clarke, *Computational phlebology: The simulation of a vein valve.* Journal of Biological Physics, 2006. **32**(6): p. 507-521.

79. Einstein, D.R., F. Del Pin, X. Jiao, A.P. Kuprat, J.P. Carson, K.S. Kunzelman, R.P. Cochran, J.M. Guccione, and M.B. Ratcliffe, *Fluid–structure interactions of the mitral valve and left heart: comprehensive strategies, past, present and future.* International Journal for Numerical Methods in Biomedical Engineering, 2010. **26**(3-4): p. 348-380.

80. Le, T.B. and F. Sotiropoulos, *Fluid–structure interaction of an aortic heart valve prosthesis driven by an animated anatomic left ventricle.* Journal of computational physics, 2013. **244**: p. 41-62.

81. Caulk, A.W., Z.V. Nepiyushchikh, R. Shaw, J.B. Dixon, and R.L. Gleason, *Quantification of the passive and active biaxial mechanical behaviour and microstructural organization of rat thoracic ducts.* Journal of The Royal Society Interface, 2015. **12**(108): p. 20150280.

82. Gashev, A.A., R.-Z. Zhang, M. Muthuchamy, D.C. Zawieja, and M.J. Davis, *Regional heterogeneity of length–tension relationships in rat lymph vessels.* Lymphatic research and biology, 2012. **10**(1): p. 14-19.

83. Rahbar, E., J. Weimer, H. Gibbs, A.T. Yeh, C.D. Bertram, M.J. Davis, M.A. Hill, D.C. Zawieja, and J.E. Moore Jr, *Passive pressure–diameter relationship and structural composition of rat mesenteric lymphangions.* Lymphatic research and biology, 2012. **10**(4): p. 152-163.

84. Gosselin, F., E. De Langre, and B.A. Machado-Almeida, *Drag reduction of flexible plates by reconfiguration.* Journal of Fluid Mechanics, 2010. **650**: p. 319.

85. Alben, S., M. Shelley, and J. Zhang, *Drag reduction through self-similar bending of a flexible body.* Nature, 2002. **420**(6915): p. 479-481.

86. Cermak, J.E. *Wind tunnel studies of buildings and structures*. 1999. American Society of civil engineers.

87. De Langre, E., *Effects of wind on plants.* Annu. Rev. Fluid Mech., 2008. **40**: p. 141-168.

88. Schouveiler, L. and A. Boudaoud, *The rolling up of sheets in a steady flow.* Journal of Fluid Mechanics, 2006. **563**: p. 71.

89. Lauweryns, J.M. and L. Boussauw, *The ultrastructure of lymphatic valves in the adult rabbit lung.* Zeitschrift für Zellforschung und Mikroskopische Anatomie, 1973. **143**(2): p. 149-168.

90. Caulk, A.W., J.B. Dixon, and R.L. Gleason, *A lumped parameter model of mechanically mediated acute and long-term adaptations of contractility and geometry in lymphatics for characterization of lymphedema.* Biomechanics and modeling in mechanobiology, 2016. **15**(6): p. 1601-1618.

91. Gashev, A.A., M.J. Davis, M.D. Delp, and D.C. Zawieja, *Regional variations of contractile activity in isolated rat lymphatics.* Microcirculation, 2004. **11**(6): p. 477-492.

92. Sacks, M.S. and A.P. Yoganathan, *Heart valve function: a biomechanical perspective.* Philosophical Transactions of the Royal Society of London B: Biological Sciences, 2007. **362**(1484): p. 1369-1391.

93. Ohhashi, T., T. Azuma, and M. Sakaguchi, *Active and passive mechanical characteristics of bovine mesenteric lymphatics.* American Journal of Physiology-Heart and Circulatory Physiology, 1980. **239**(1): p. H88-H95.

94. Zawieja, D.C., K.L. Davis, R. Schuster, W.M. Hinds, and H.J. Granger, *Distribution, propagation, and coordination of contractile activity in lymphatics.* American Journal of Physiology-Heart and Circulatory Physiology, 1993. **264**(4): p. H1283-H1291.

95. Akl, T.J., G.L. Coté, Z.V. Nepiyushchikh, A.A. Gashev, and D.C. Zawieja, *Measuring contraction propagation and localizing pacemaker cells using high speed video microscopy.* Journal of biomedical optics, 2011. **16**(2): p. 026016.

96. Gashev, A.A., M.J. Davis, and D.C. Zawieja, *Inhibition of the active lymph pump by flow in rat mesenteric lymphatics and thoracic duct.* The Journal of physiology, 2002. **540**(3): p. 1023-1037.

97. Kornuta, J.A., Z. Nepiyushchikh, O.Y. Gasheva, A. Mukherjee, D.C. Zawieja, and J.B. Dixon, *Effects of dynamic shear and transmural pressure on wall shear stress sensitivity in collecting lymphatic vessels.* American Journal of Physiology-Regulatory, Integrative and Comparative Physiology, 2015. **309**(9): p. R1122-R1134.

98. Watson, D.J., I. Sazonov, D.C. Zawieja, J.E. Moore, and R. van Loon, *Integrated geometric and mechanical analysis of an image-based lymphatic valve.* Journal of biomechanics, 2017. **64**: p. 172-179.

99. Margaris, K. and R.A. Black, *Modelling the lymphatic system: challenges and opportunities.* Journal of the Royal Society Interface, 2012. **9**(69): p. 601-612.

100. Pan, W.R., C.M. Le Roux, S.M. Levy, and C.A. Briggs, *The morphology of the human lymphatic vessels in the head and neck.* Clinical Anatomy, 2010. **23**(6): p. 654-661.

101. Scallan, J.P., J.H. Wolpers, M. Muthuchamy, D.C. Zawieja, A.A. Gashev, and M.J. Davis, *Independent and interactive effects of preload and afterload on the pump function of the isolated lymphangion.* American Journal of Physiology-Heart and Circulatory Physiology, 2012. **303**(7): p. H809-H824.

102. Kassis, T., S.C. Yarlagadda, A.B. Kohan, P. Tso, V. Breedveld, and J.B. Dixon, *Postprandial lymphatic pump function after a high-fat meal: a characterization of contractility, flow, and viscosity.* American Journal of Physiology-Gastrointestinal and Liver Physiology, 2016. **310**(10): p. G776-G789.

103. Burton-Opitz, R. and R. Nemser, *The viscosity of lymph.* American Journal of Physiology-Legacy Content, 1917. **45**(1): p. 25-29.

104. Böhme, G. and A. Müller, *Analysis of non-Newtonian effects in peristaltic pumping.* Journal of Non-Newtonian Fluid Mechanics, 2013. **201**: p. 107-119.

105. Hariharan, P., V. Seshadri, and R.K. Banerjee, *Peristaltic transport of non-Newtonian fluid in a diverging tube with different wave forms.* Mathematical and Computer Modelling, 2008. **48**(7-8): p. 998-1017.

106. Rachid, H. and M. Ouazzani, *Mechanical efficiency of peristaltic pumping of a Newtonian fluid between two deformable coaxial tubes with different phases and amplitudes.* The European Physical Journal Plus, 2015. **130**(6): p. 122.

107. Rao, A.R. and S. Usha, *Peristaltic transport of two immiscible viscous fluids in a circular tube.* Journal of Fluid Mechanics, 1995. **298**: p. 271-285.

108. Tripathi, D., *Study of transient peristaltic heat flow through a finite porous channel.* Mathematical and Computer Modelling, 2013. **57**(5-6): p. 1270-1283.

109. Connington, K., Q. Kang, H. Viswanathan, A. Abdel-Fattah, and S. Chen, *Peristaltic particle transport using the lattice Boltzmann method.* Physics of Fluids, 2009. **21**(5): p. 053301.

110. Pozrikidis, C., *A study of peristaltic flow.* Journal of Fluid Mechanics, 1987. **180**: p. 515-527.

111. Zien, T.-F. and S. Ostrach, *A long wave approximation to peristaltic motion.* Journal of Biomechanics, 1970. **3**(1): p. 63-75.

112. Sutera, S.P. and R. Skalak, *The history of Poiseuille's law.* Annual review of fluid mechanics, 1993. **25**(1): p. 1-20.

113. Mao, W. and A. Alexeev, *Motion of spheroid particles in shear flow with inertia.* Journal of Fluid Mechanics, 2014. **749**: p. 145-166.

114. Uchida, S. and H. Aoki, *Unsteady flows in a semi-infinite contracting or expanding pipe.* Journal of Fluid Mechanics, 1977. **82**(2): p. 371-387.

115. Wolf, K.T., J.B. Dixon, and A. Alexeev, *Fluid pumping of peristaltic vessel fitted with elastic valves.* Journal of Fluid Mechanics, (In press).